

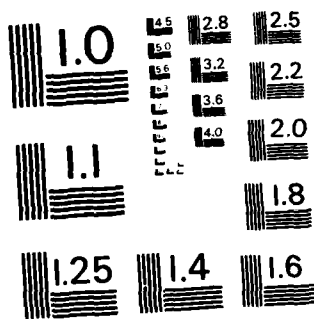
1/2

UNCLASSIFIED

FTD-10(RS)T-1010-82

F/G 20/4

NL



MICROCOPY RESOLUTION TEST CHART
NATIONAL BUREAU OF STANDARDS-1963-A

AD A131031

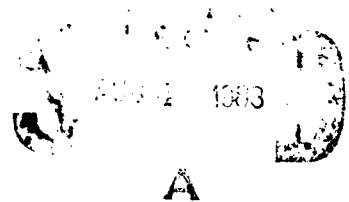
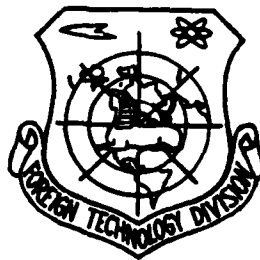
FOREIGN TECHNOLOGY DIVISION



FLOW-FIELD MATRIX SOLUTION FOR DIRECT PROBLEM OF FLOW
ALONG S_1 RELATIVE STREAM SURFACE EMPLOYING
NON-ORTHOGONAL CURVILINEAR COORDINATES
AND CORRESPONDING NON-ORTHOGONAL
VELOCITY COMPONENTS

by

Wu Wenquau and Liu Cuie



Approved for public release;
distribution unlimited.

DTIC FILE COPY

83 08 3 . 215

EDITED TRANSLATION

FTD-ID(RS)T-1010-82

18 July 1983

MICROFICHE NR: FTD-83-C-000860

FLOW-FIELD MATRIX SOLUTION FOR DIRECT PROBLEM OF
FLOW ALONG S_1 RELATIVE STREAM SURFACE EMPLOYING
NON-ORTHOGONAL CURVILINEAR COORDINATES AND
CORRESPONDING NON-ORTHOGONAL VELOCITY COMPONENTS

By: Wu Wenquau and Liu Cuie

English pages: 127

Source: Gongcheng Rewuli Xuebao, Vol. 1, Nr. 1,
February 1980, pp. 17-79; 95-102

Country of origin: China

Translated by: SCITRAN

F33657-81-D-0263

Requester: FTD/TQTA

Approved for public release; distribution unlimited.



THIS TRANSLATION IS A RENDITION OF THE ORIGINAL FOREIGN TEXT WITHOUT ANY ANALYTICAL OR EDITORIAL COMMENT. STATEMENTS OR THEORIES ADVOCATED OR IMPLIED ARE THOSE OF THE SOURCE AND DO NOT NECESSARILY REFLECT THE POSITION OR OPINION OF THE FOREIGN TECHNOLOGY DIVISION.

PREPARED BY:

TRANSLATION DIVISION
FOREIGN TECHNOLOGY DIVISION
WP-AFB, OHIO.

FTD -ID(RS)T-1010-82

Date 18 Jul 19 83

TABLE OF CONTENTS

	<u>PAGE NO.</u>
ABSTRACT	1
TABLE OF SYMBOLS	2
INTRODUCTION	3
I. The Basic Set of Equations	4
II. The Coordinate System and the Velocity Component Equation	5
III. Stream Function and Stream Function Equation	8
IV. The Computational Mesh and Boundary Conditions . . .	10
V. The Storage of the Coefficient Matrix and the Decomposition of [L] [u]	13
VI. The Computation of the Density ρ and the Selection of the Relaxation Factor	15
VII. Computational Examples	17
CONCLUSIONS	19
* * *	
ABSTRACT	22
I. Introduction	23
II. The line Relaxation Solution Computer Program for S ₂ Stream Surface Stream Function by Using Non-orthogonal curvilinear Coordinates and Non-orthogonal Velocity Components	26
III. The Comparison of Several Numerical Computational Methods and Discussion	35
* * *	
ABSTRACT	40
I. Introduction.	41
II. Basic Equations	42
III. The Super Relaxation Solution Method and Convergence Algorithm and Results	45
IV. Discussion of the Principal Equation.	49

TABLE OF CONTENTS (CONTINUED):	<u>PAGE</u>
ABSTRACT	53
I. Introduction	54
II. Computation of the Center S_2 Stream Surface and the Design of the Flow Passage	55
III. Computation of Subsonic Surfaces of Revolution.	62
IV. Computation of Supersonic Surfaces of Revolution	66
V. The Final Results of Stream Surface Iteration and Cumulative Iteration	70
VI. Conclusions	71
* * *	
ABSTRACT	73
I. Introduction	74

GRAPHICS DISCLAIMER

All figures, graphics, tables, equations, etc. merged into this translation were extracted from the best quality copy available.

FLOW FIELD MATRIX SOLUTION FOR DIRECT PROBLEM OF FLOW
ALONG S_1 RELATIVE STREAM SURFACE EMPLOYING NON-ORTHOGONAL
CURVILINEAR COORDINATES AND CORRESPONDING NON-ORTHOGONAL
VELOCITY COMPONENTS*

Wu Wenquau and Liu Cuie
(Academia Sinica)

ABSTRACT

Based on the basic three-dimensional flow thermo aerodynamic equations of turbine machinery proposed by Wu Chung-Hua employing non-orthogonal curvilinear coordinates and their corresponding non-orthogonal velocity components, the main function to be solved i.e., the second order quasilinear partial differentiation equation of the stream function, was obtained in this paper by introducing a stream function. With the exception of density related terms, the various order of derivatives of the stream function were placed on the left side of the equation. By doing so, the convergence rate was accelerated. After discretization of the differential equation by using a center nine-point difference format, the linear algebraic equations obtained were solved directly by the decomposition of the matrices $[L]$ and $[u]$. The convergence rate of this method is comparatively faster than other methods. The coefficient matrix is a diagonal band shaped scattered matrix. We adopted the two measures that: 1) non-zero elements were numbered according to the diagonal line, and 2) fictitious points were added, to greatly reduce the internal storage of the computer. When calculating the density from the stream function, an internally-stored density function table interpolation method was adopted. The selection of relaxation factor was briefly discussed. This program was used in the calculation of the blade patterns of

/17**

* This paper was presented in the 1976 National Turbine Machinery Aerodynamic Conference.

** Numbers in the margin indicate pagination of foreign text.

some compressors and turbines. In comparison of the experimental results and the theoretical analytical solutions, they were in mutual agreement.

TABLE OF SYMBOLS

e_i	base vector of a coordinate in the x^i coordinate system
e^i	reciprocal vector of e_i
a_{ij}	forward transformation tensor element of the x^i coordinate system
a	the Jacobrau determinant composed of a_{ij}
I	the enthalpy of stagnant gas rotor
x^i	an arbitrary non-orthogonal curvilinear coordinate system
w^i	the reverse transformation component of the relative velocity vector of the gas
w_i	the forward transformation component of the relative velocity vector of the gas
W^i	the physical component on the x^i coordinate of the relative velocity vector of the gas
u_i	unit vector of the x^i coordinate system
θ_1	the angle between the x^1 coordinate line and the revolving parent line
θ_2	the angle between the x^2 coordinate line and the revolving line
Σ	the density function
ϕ	a function of the partial derivatives of the stream function
Ψ	the relative motion stream function

Superscript:

/18

- o stagnant parameter
- ^ relative stagnant parameter
- * dimensionless parameter

Subscript:

- i inlet station parameter
- j calculation station along the x^1 direction
- k calculation station along the x^2 direction

INTRODUCTION

The analysis and calculation of the cascade deflected flow, i.e., the computation of the S_1 relative stream surface, is an important aspect in the three-dimensional flow computation of turbine machinery. It not only is a direct solution to the blade pattern problem, but also is an indispensable part in the alternating iteration of the S_1 and S_2 types of relative stream surface in a three-dimensional flow computation. By doing so, not only the flow conditions upstream and downstream from the blade are satisfied, but also the flow conditions of the gas flow in the blade channel are ensured.

In References[3-5], the basic equations of three-dimensional flow in turbine machinery were presented by employing arbitrary non-orthogonal curvilinear coordinates and their corresponding non-orthogonal velocity components. Its characteristics are that it can adapt to any complex shape and type of turbine machinery, and it is capable of rigorously satisfying the tangential condition between the flow and the boundary along the boundary of the object. Based on this set of basic equations, this paper presented the actual computation method. Because of the non-orthogonal curvilinear

coordinates, it also involved the computation of the geometric characteristics of the coordinates. These computation methods belonged to the original type.

We compiled the computer program on the 6912 machine at Beijing University. Its internal storage is 64K. The allowable computational nodal points reached 900 points (approximately 15 points between cascades), which is sufficient for the usual engineering requirements. If the capacity of the computer is less, it is possible to reduce it further. Finally, some typical computational results are given. A comparison of the experimental results and the theoretical analytical solutions was carried out; they were in mutual agreement.

I. The Basic Set of Equations

Assuming the motion relative the blade is stable and adiabatic, then the basic equations are^[1,2]:

Continuity equation

$$\nabla \cdot (\rho \mathbf{W}) = 0 \quad (1)$$

Equation of motion

$$\mathbf{W} \times (\nabla \times \mathbf{V}) \approx g_c J (\nabla I - T \nabla s) \quad (2)$$

First Law of Thermodynamics — energy equation

$$dI/dt = \mathbf{W} \cdot \nabla I \approx 0 \quad (3)$$

Where

$$I \equiv h + |\mathbf{W}|^2/2 + |\mathbf{U}|^2/2 \quad (4)$$

Second law of thermodynamics

$$T ds/dt \geq 0 \quad (5)$$

Ideal gas state equation

$$p = \rho RT \quad (6)$$

In the derivative of the original equations, the equation of motion took the viscoisty of the gas into account and it contained a viscosity term. Due to the viscosity effect and the shock wave loss, an enthalpy increase was produced. Therefore, the equation set is consistent. However, in the actual computation, the viscosity term was neglected in the equation of motion. It is due not only to the complexity of its computation, but also to the fact that it is a small term comparatively speaking. Thus, the approximate relations in equations (2) and (3) were obtained. The gradient of enthalpy in the equation was calculated through the selection of empirical data such as the efficiency or presume loss coefficient, and the loss during passing through shock waves, etc. The above equations were expressed in an invariant form with respect to the coordinates. They are applicable to all coordinate systems. Furthermore, they are simple and easy to understand. /19

II. The Coordinate System and the Velocity Component Equation

By choosing an arbitrary non-orthogonal curvilinear coordinate system (x^1, x^2, x^3) and substituting the correlations of the degree of revolution into the basic equations in the previous section, it is possible to obtain the expression for each component. Specially with regard to the direct problem of the S_1 relative stream surface calculation, because the shape of the stream surface is known, then it is possible to choose this known stream surface

as a coordinate plane $x^3 = \text{constant}$. Furthermore, the x^3 coordinate was made perpendicular to this plane as shown in Figure 1. The coordinate lines (x^1, x^2) are shown in Figure 2. Because the iso- x^3 planes are the stream surfaces, the velocity vector must be tangent to this stream surface. This

$$w^3 \equiv 0 \quad (7)$$

For the usual engineering requirement, it is possible to assume that this S_1 stream surface is an arbitrary revolving surface. From equations (2) and (7), we can obtain the component along the e_2 direction to be

$$-w^1 \left[\left(\frac{\partial w_2}{\partial x^1} - \frac{\partial w_1}{\partial x^2} \right) + 2\omega^1 \sqrt{a} \right] = \frac{\partial l}{\partial x^2} - r \frac{\partial s}{\partial x^2} \quad (8)$$

In order to more precisely show the physical significance and to facilitate the consistent computation, the w^1 and w_1 in equation (8) were further expressed by the physical component $W^{\bar{1}}$:

$$w_i = a_{i1} w^1 = \sqrt{a_{i1}} W^{\bar{1}} \quad (9)$$

The distance between two neighboring iso- x^3 planes (i.e., two neighboring S_1 stream surfaces) is τ . In addition, let $dx^3 = 1$ then

$$\sqrt{a_{33}} = \tau \quad (10)$$

Due to the x^3 coordinate line being chosen to be perpendicular to this stream surface, then

$$a_{13} = a_{31} = a_{23} = a_{32} = 0 \quad (11) \quad /20$$

From the definitions

$$a_{12} = \frac{\partial l}{\partial x^1} \frac{\partial l}{\partial x^2} + \frac{\partial(r\varphi)}{\partial x^1} \frac{\partial(r\varphi)}{\partial x^2} = \sqrt{a_{11}} \sqrt{a_{22}} \cos \theta_{12} \quad (12)$$

$$a = a_{11}a_{22}a_{33}, \sin^2 \theta_{12} = r^2 a_{11}a_{22} \sin^2 \theta_{12} \quad (13)$$

From equation (9)

$$w_1 = a_{11}w^1 + a_{12}w^2 = \sqrt{a_{11}}(W^1 + W^2 \cos \theta_{12}) \quad (14)$$

$$w_2 = a_{21}w^1 + a_{22}w^2 = \sqrt{a_{22}}(W^2 + W^1 \cos \theta_{12}) \quad (15)$$

Substituting equations (14) and (15) into (8) we get

$$\begin{aligned} \frac{\partial}{\partial x^2} [(W^1 + W^2 \cos \theta_{12}) \sqrt{a_{11}}] - \frac{\partial}{\partial x^1} [(W^2 + W^1 \cos \theta_{12}) \sqrt{a_{22}}] \\ = 2\sqrt{a_{11}}\sqrt{a_{22}}\omega^3 \sin \theta_{12} + \frac{\sqrt{a_{11}}}{W^1} \left(\frac{\partial I}{\partial x^2} - T \frac{\partial s}{\partial x^2} \right) \end{aligned} \quad (16)$$

If we choose

$$x^1 = l, \quad x^2 = \varphi,$$

then

$$\sqrt{a_{11}} = 1, \quad \sqrt{a_{22}} = r, \quad \theta_{12} = \frac{\pi}{2}, \quad W^1 = W_l, \quad W^2 = W_\varphi$$

Equation (16) can be simplified as

$$\frac{\partial W_l}{r \partial \varphi} - \frac{\partial W_\varphi}{\partial l} - \frac{W_\varphi \sin \sigma}{r} - 2\omega \sin \sigma = \frac{1}{W_l} \left(\frac{\partial I}{r \partial \varphi} - T \frac{\partial s}{r \partial \varphi} \right) \quad (17)$$

This is the form of equation which is familiar to us.^[2] Equation (16) contained two relative velocity physical components W^1 and W^2 which were to be determined. These could be solved by using the so-called streamline extension method. However, the more suitable method was to introduce a stream function ψ to further transform the equation.

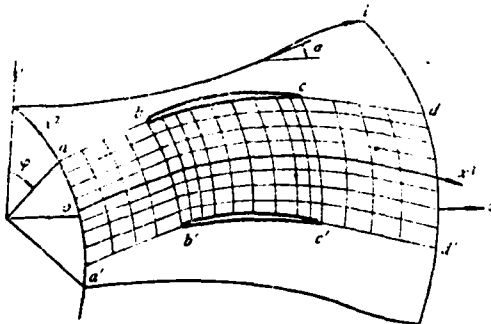


Figure 1. The arbitrary revolving plane of the S_1 relative stream surface.

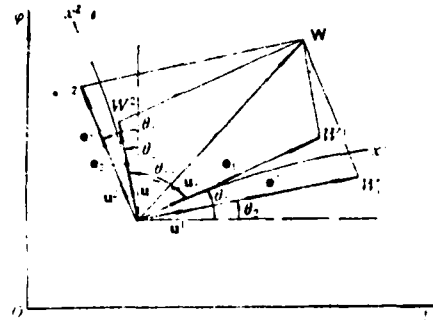


Figure 2. The arbitrary non-orthogonal curvilinear coordinate system (x^1, x^2) .

III. Stream Function and Stream Function Equation

From the continuity equation (1) and $W^3=0$, we get

$$\frac{\partial}{\partial x^1} (\rho r \sqrt{a_{22}} \sin \theta_{12} W^1) + \frac{\partial}{\partial x^2} (\rho r \sqrt{a_{11}} \sin \theta_{12} W^2) = 0 \quad (18)$$

Define the stream function Ψ which satisfied the following relation

$$\tau \rho \sqrt{a_{11}} \sin \theta_{12} W^2 = - \frac{\partial \Psi}{\partial x^1}; \quad \tau \rho \sqrt{a_{22}} \sin \theta_{12} W^1 = \frac{\partial \Psi}{\partial x^2} \quad (19)$$

By substituting equation (19) into (16), we can obtain the stream function equation. In order to calculate conveniently, the equation was further rendered dimensionless. The dimensionless reference quantities are: $\Psi^* = \Psi / G \cdot 100$; $\rho^* = \rho / \rho_i$; $T^* = T / T_i$; $\rho^* = \rho / \rho_i$;

$$\begin{aligned} \tau^* &= \tau / \tau_i; \quad r^* = r / r_i; \quad \omega^* = \omega r_i / U_i = 1; \quad \sqrt{a_{11}}^* = \sqrt{a_{11}} / r_i; \\ \sqrt{a_{22}}^* &= \sqrt{a_{22}} / r_i; \quad (W^1)^* = W^1 / U_i; \quad (W^2)^* = W^2 / U_i; \quad (20) \\ l^* &= l \cdot g_i J / U_i^2; \quad H^* = H \cdot g_i J / U_i^2; \end{aligned}$$

where G is the rate of flow through a blade duct, and U_i is the revolving speed at the inlet. We get^[6]

$$\frac{1}{a_{11}^*} \frac{\partial^2 \Psi^*}{(\partial x^1)^2} - \frac{2 \cos \theta_{12}}{\sqrt{a_{11}^*} \sqrt{a_{22}^*}} \frac{\partial^2 \Psi^*}{\partial x^1 \partial x^2} + \frac{1}{a_{22}^*} \frac{\partial^2 \Psi^*}{(\partial x^2)^2} + \frac{J}{\sqrt{a_{11}^*}} \frac{\partial \Psi^*}{\partial x^1} + \frac{K}{\sqrt{a_{22}^*}} \frac{\partial \Psi^*}{\partial x^2} = M \quad (21)$$

where

$$\begin{aligned} J &= - \frac{\partial \ln (\sqrt{a_{11}^*} \sqrt{a_{22}^*} \tau^* \sin \theta_{12})}{\sqrt{a_{11}^*} \partial x^1} + \frac{\cos \theta_{12} \partial \ln \tau^*}{\sqrt{a_{22}^*} \partial x^2} + \frac{1}{\sin \theta_{12} \sqrt{a_{22}^*}} \frac{\partial \theta_{12}}{\partial x^2} \\ K &= - \frac{\partial \ln (\sqrt{a_{22}^*} / a_{11}^* \tau^* \sin \theta_{12})}{\sqrt{a_{22}^*} \partial x^2} + \frac{\cos \theta_{12} \partial \ln \tau^*}{\sqrt{a_{11}^*} \partial x^1} + \frac{1}{\sin \theta_{12} \sqrt{a_{11}^*}} \frac{\partial \theta_{12}}{\partial x^1} \\ M &= \left(\frac{1}{\sqrt{a_{11}^*}} \frac{\partial \ln \rho^*}{\partial x^1} - \frac{\cos \theta_{12}}{\sqrt{a_{22}^*}} \frac{\partial \ln \rho^*}{\partial x^2} \right) \frac{\partial \Psi^*}{\sqrt{a_{11}^*} \partial x^1} \\ &\quad + \left(\frac{1}{\sqrt{a_{22}^*}} \frac{\partial \ln \rho^*}{\partial x^2} - \frac{\cos \theta_{12}}{\sqrt{a_{11}^*}} \frac{\partial \ln \rho^*}{\partial x^1} \right) \frac{\partial \Psi^*}{\sqrt{a_{22}^*} \partial x^2} \\ &\quad - 2 \tau^* \rho^* \Gamma \sin \sigma \sin^2 \theta_{12} + (\tau^* \rho^* \sin \theta_{12})^2 \left(\frac{\partial \Psi^*}{\partial x^2} \right)^{-1} \left(\frac{\partial l^*}{\partial x^2} - \tau^* \frac{\partial r^*}{\partial x^2} \right) \end{aligned}$$

where

$$r^* = \frac{100}{M_{w_i}} \frac{a_i}{U_i} \Delta \rho_i \cos \beta_i \left(1 + \frac{k-1}{2} M_{w_i}^2 \right)^{-\frac{1}{k-1}}$$

is a dimensionless constant which represented the various incoming gas states, i.e., corresponding to various cascade density $\Delta \phi_t$, gas entering angle β_i , the relative M number of the entering gas M_{w_i} , and the revolving speed U_i , etc. The coefficients in equation (21) were the only geometrical parameters of the coordinate system. After the mesh was determined, these coefficients only needed to be calculated once. The major terms are already included on the left side of the equation. On the right hand side, there are non-linear terms due to variation of density. These require to be calculated through "iteration". Usually, the value obtained from the previous iteration process is chosen. In reality, the original second order quasilinear partial differential equation is transformed into a second order linear partial differential equation and the solution is sought through iteration.

The qualitative determining formula of equation (21) is

$$\Delta = 1/a_{11}^* a_{22}^* - \cos^2 \theta_{12} / a_{11}^* a_{22}^* > 0 \quad (22)$$

We can see that it is an elliptical equation which is suitable for subsonic flow. The original basic equation was not limited by this condition. The problem is located in the treatment of the density terms. As a matter of fact, density is related to velocity which includes the first order derivative of Ψ . Therefore, the right hand terms actually contain a second order partial derivative term of Ψ , which affects the equation qualitatively. If the right hand terms of equation (21) are all moved to the left hand side, then the equation changes from an elliptical type to a hyperbolic type as the flow velocity changes from subsonic to supersonic. However, our present treatment is only suitable for subsonic flows. If we entered the supersonic region

in the computation, the program has an automatic alarming measure arranged in it.

In order to solve equation (21), it is also possible to keep the partial derivatives with respect to x^2 on the left hand side and the remaining terms are moved to the right hand side. Thus, the equation is transformed into a normal differential equation of x^2 in looking for the solution. This method is the so-called stream line extension method. The actual computation showed that when the computation mesh is densified (mainly in the streamline direction) then the convergence rate of the flow field matrix method is much faster than that of the streamline extension method. The reason is that a large number of undetermined terms are moved to the right hand side in the streamline extension method to be substituted by the values obtained in the previous iteration process. Thus, this large lagging quantity is affecting the convergence rate. Therefore, the flow field matrix method is used to solve the equation in the following.

IV. The Computational Mesh and Boundary Conditions

/22

For the usual S_1 flow surface calculation it is possible to choose the (x^1, x^2) coordinate lines as shown in Figure 1, in which the x^2 line is a circular arc and the x^1 line is the line connecting all the points dividing the width of the blade duct according to the same proportion in the blade duct. In the upstream and downstream regions of the blade, it can be simply chosen as a straight line on the $\phi - l$ plane. The angles of inclination with respect to line l are β_1 and β_2 , respectively. The computational mesh formed this way only will require the input of a few data: the parent line $r(z)$ of the revolving surface, the blade surface coordinates $\phi_p(z)$ and $\phi_s(z)$ the gas entrance and exit angles β_1, β_2 . It is very convenient. If the computational mesh is plotted on the $x^1 - x^2$ plane, it is as shown in Figure 3. Thus, it means

that the computational mesh is standardized.

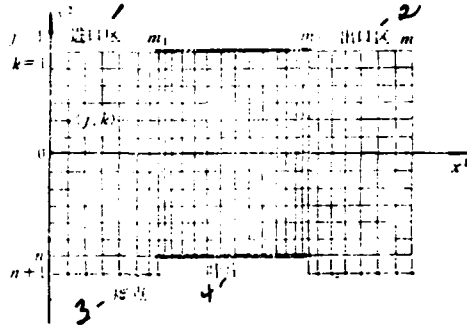


Figure 3. The standardized computational mesh.

Key: 1) inlet zone; 2) outlet zone; 3) fictitious point;
4) blade.

In the computation, it is also required to obtain some geometric parameters such as $\sqrt{a_{11}}$, $\sqrt{a_{22}}$, O_{12} , etc. Numerical differentiation was also used here. To obtain $\sqrt{a_{11}}$, there are two types of correlations:

$$\sqrt{a_{11}} = dS_{(1)}/dx^1 \quad (23)$$

or

$$\sqrt{a_{11}} = \sqrt{\frac{\partial l}{\partial x^1} \frac{\partial l}{\partial x^1} + \frac{\partial(r\varphi)}{\partial x^1} \frac{\partial(r\varphi)}{\partial x^1}} \quad (24)$$

Our experience is that it is more difficult based on equation (24). Theoretically speaking, the values of $\sqrt{a_{11}}$ and so on can vary with the arbitrary selection of x^1 . However, when considering

the error of numerical differentiation, it is better off to have the values of $\sqrt{a_{11}}$, $\sqrt{a_{22}}$, etc. be close to 1. Therefore, we selected the x^1 line with $x^2=0$ on the center line of the blade duct. Furthermore, we chose $\sqrt{a_{11}}=1$ on this line.

Because of the use of a curvilinear coordinate and also because of the introduction of the stream function, the boundary conditions are very simple and easy to understand:

(1) along the surface of the blade

$$m_1 \leq k \leq m_2$$

The surface of the blade is a stream line, and ψ is a constant.

$$\psi_{1,k}^* = 0; \quad \psi_{n,k}^* = 100$$

(2) the inlet and outlet regions

$$1 \leq k \leq m_1; \quad m_2 \leq k \leq m$$

A periodical condition exists, i.e.

For any aerodynamic parameter

$$F_{j,k} = F_{j+n,k}$$

123

The stream function ϕ^*

$$\phi_{j,k}^* = \phi_{j+n,k}^* - 100 = \phi_{j-n,k}^* + 100$$

(3) The Entrance and Exit Gas Boundaries, aa', dd'.

Assuming that the entering and exiting gas boundaries are located at an infinite distance away from the blade, then the two boundary flows are homogeneous. Actual calculations showed that

it is sufficient if they are in front of and behind the blade by a cascade distance. The boundary conditions here are:

$$(c) = \text{constant} \quad \frac{\partial \phi^*}{\partial x^2} = \text{const} = \frac{100}{x_2^2 - x_1^2}; \quad \frac{\partial \phi^*}{\partial x^1} = 0$$

V. The Storage of the Coefficient Matrix and the Decomposition of [L] [u]

The various partial derivatives in the above equation (21) all adopted a three-point center difference formula to form a center nine-point difference format to discretize the equation. The linear algebraic equations can be written as

$$[M]\{\psi^*\} = \{p\} \quad (25)$$

[M] is a matrix formed by the coefficients, $\{\psi^*\}$, $\{p\}$ are the column vectors. It is possible to use various methods to solve this equation set (25) such as point iteration, improved point iteration, and linear relaxation. This paper adopted the direct decomposition of [L] [u] method. The purpose is to accelerate the convergence rate. From (25)

$$[L][u]\{\psi^*\} = \{p\} \quad (26)$$

$$[u]\{\psi^*\} = \{Q\} \quad (27)$$

to solve and obtain ϕ^* . The reality showed that this method is comparatively faster.

The difficulty of this method is that it is necessary to store the large capacity coefficient matrix [M]. Fortunately, this [M] is a diagonally band shaped scattered matrix. In order to reduce the internal storage, two measures were taken.

(1) Renumbering the coefficient $M_{j,k}$ according to the diagonal line.

If $[M]$ is stored as a two-dimensional number group $M[1:mn, 1:mn]$, then it is difficult to eliminate the large amount of non-zero elements.

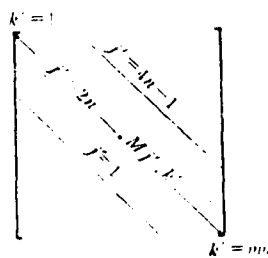


Figure 4a. The original matrix.

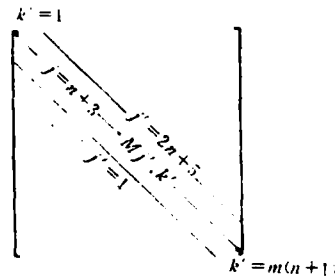


Figure 4b. The matrix after adding fictitious points.

We renumbered the elements along the diagonal line. As shown in Figure (4a): j' represents the diagonal line number from 1 to $4n-1$ and k' represents the element sequence along the diagonal line direction from 1 to mn . At this time, the internally stored numbers are

$$N = (4n - 1) mn$$

(2) Adding fictitious points.

A periodical condition exists in the inlet and outlet regions of the blade which caused the doubling of the non-zero elements. For this purpose, a row of nodal points were added in the inlet region and outlet region, respectively, as shown in Figure 3. These nodal points are not the ones we wanted to calculate. However, they are still included in the numbers. Therefore, they

/24

are called fictitious points. Thus, the band width is changed to $2n+5$. Now, the required internal storage is

$$N = 2n^2m + (7n + 5)m$$

The internally stored quantity is reduced by

$$2n^2m - (8n + 5)m$$

This N increases with n according to a square relation. Thus, the internal storage is saved by approximately a half. Along with increasing n value, the effect is especially obvious. If we choose $m=50$, $n=15$, then $N=28,000$. Similarly, when $m, n=10$, then $N=13,750$. Therefore, this program can be used on a 32K-64K internal storage computer.

/24

VI. The Computation of the Density ρ and the Selection of the Relaxation Factor

In the density calculation, the variation of enthalpy can be taken into account. However, in the S_1 stream surface calculation, due to lack of experimental data, usually it is an iso-enthalpic flow. Therefore, we also treated it using the iso-enthalpic correlation to obtain^[1]

$$\begin{aligned} \rho^* &= \left(\frac{h}{H_i^*} \right)^{\frac{1}{k-1}} = \left(\frac{I^* + \frac{1}{2} (r^*)^2}{H_i^*} - \frac{|W^*|^2}{2H_i^*} \right)^{\frac{1}{k-1}} \\ \rho^{*2} \left(\frac{I^* + \frac{1}{2} r^{*2}}{H_i^*} \right)^{-\frac{1}{k-1}} &= \left\{ 1 - \frac{1}{2H_i^* (\tau^* \rho^* \sin \theta_{12} \Gamma)^2} \left(\frac{I^* + \frac{1}{2} r^{*2}}{H_i^*} \right)^{-\frac{k+1}{k-1}} \right. \\ &\quad \cdot \left(\frac{I^* + \frac{1}{2} r^{*2}}{H_i^*} \right)^{\frac{2}{k-1}} \left[\left(\frac{\partial \phi^*}{\sqrt{a_{11}^*} \partial x^1} \right)^2 + \left(\frac{\partial \phi^*}{\sqrt{a_{22}^*} \partial x^2} \right)^2 \right. \\ &\quad \left. \left. + 2 \frac{\partial \phi^*}{\sqrt{a_{11}^*} \partial x^1} \frac{\partial \phi^*}{\sqrt{a_{22}^*} \partial x^2} \cos \theta_{12} \right] \right\}^{\frac{1}{k-1}} \end{aligned} \quad (28)$$

Let

$$\Sigma = \rho^{*2} \left(\frac{I^* + \frac{1}{2} r^{*2}}{H_i^*} \right)^{-\frac{2}{k-1}}$$

$$\Phi = \frac{1}{2H_i^* (r^* \sin \theta_{12} \Gamma)^2} \left(\frac{I^* + \frac{1}{2} r^{*2}}{H_i^*} \right)^{-\frac{k+1}{k-1}} \left[\left(\frac{\partial \phi^*}{\sqrt{a_{11}^*} \partial x^1} \right)^2 + \left(\frac{\partial \phi^*}{\sqrt{a_{22}^*} \partial x^2} \right)^2 + 2 \frac{\partial \phi^*}{\sqrt{a_{11}^*} \partial x^1} \frac{\partial \phi^*}{\sqrt{a_{22}^*} \partial x^2} \cos \theta_{12} \right]$$

then

$$\Sigma^2 = (1 - \Phi/\Sigma^2)^{\frac{2}{k-1}} \quad (29)$$

When ϕ^* is solved, Φ can be obtained. From (32) we can find Σ , and ρ^* can be further obtained. Equation (29) is not explicit. In order to avoid the trouble of calculation each time, it is possible to prefabricate a Σ - Φ table to be stored in the internal storage of the computer in preparation for interpolation computation. Φ has a maximum $\Phi_{max} \approx 0.066$. This corresponds to $M=1$ and the dense flow maximum $\Sigma \approx 0.68$. It should also be noted that there are two Σ values (ρ values) corresponding to the same Φ value. One corresponds to $M < 1$ and the other corresponds to $M > 1$.

/25

When solving equation (21), the right hand terms of the equation contain ψ^* and ρ^* . This requires us to carry out iterations. Various relaxation factors α_ψ and α_ρ must be selected, respectively. According to our computational experience, the convergence of density ρ is better and usually it is chosen that $\alpha_\rho = 1$. However, α_ψ is chosen to be various values under different conditions. When the flow M number is comparatively low, α_ψ can be chosen to be a larger value. For example, in the approximate incompressible situation, then $\alpha_\psi = 1$. When the M number increases, then α_ψ should be relatively lower, usually around 0.5. When M approaches 1, then α_ψ should be even lower. This is consistent with the physical concept, i.e., when the flow is close to the speed of sound, the density flow value

does not converge easily. For the usual engineering requirements

$$\begin{aligned} |\rho^{*(v+1)} - \rho^{*(v)}| &< 10^{-5} \\ |\psi^{*(v+1)} - \psi^{*(v)}| &< 10^{-4} \end{aligned}$$

then 10-15 iterations will be sufficient. The number of iterations required is even less when the M number is low.

VII. Computational Examples

Trial computations were made for the blade shapes of compressors and turbines. In order to compare to the experimental results or theoretical analytical solutions, these are all plane cascades. A number of cascade computations were carried out and the results were all satisfactory. The following gives two typical results:

1) Reference [7] provided a compressor cascade with an incompressible analytical solution. The relative thickness is 10% and the density is relatively small. The comparison to the calculated results is as shown in Figure 5.

2) The maximum thickness of the blade of the T_1 compressor was shifted backward to 60% of the chord length to thus reduce the maximum velocity peak of the gas entrance boundary. Furthermore, a second velocity peak was at 60% of the blade chord. Thus, the allowable inlet M number can be improved. The comparison of the calculated results to the experimental ones showed that they are consistent as shown in Figure 6.^[8]

Figure 7 shows the distributions of the density flow on the center stream line and the inlet density flow ratio. It showed that the effect of blade thickness is not only limited to the blade duct, but also in the blade inlet and outlet regions. It is worthwhile noting that these compressor blade results are consistent with the turbine blade results obtained many years ago.

These must be taken into account in the design of compressors. Furthermore, these data are indispensable in the iterative calculation of the S_1 and S_2 stream surfaces.

Figure 5. Comparison between the computed results and the theoretical analytical solution.

Key: 1) numerical computed value; 2) analytical solution.

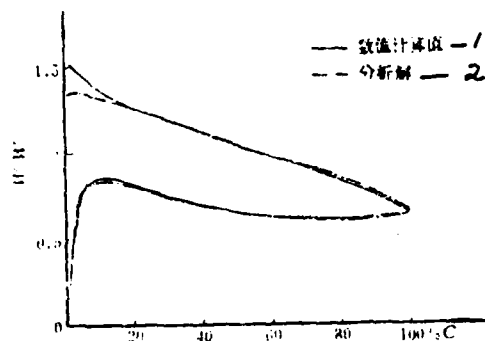


Figure 6. Comparison of computed results to the experimental results.

Key: 1) blade model; 2) calculated value; 3) experimental value.

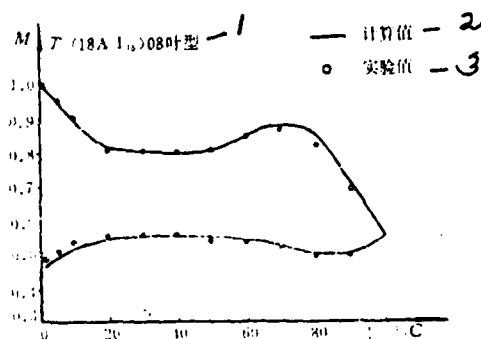
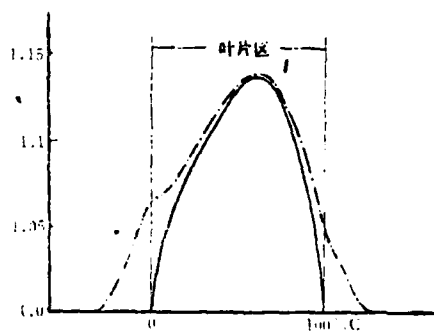


Figure 7. The effect of blade thickness.

Key: 1) blade region; 2) p is cascade distance, t is the blade thickness.

$$\frac{(\rho W \tau)_m}{(\rho W \tau)_i} \quad \frac{P}{P - t}$$



Summarizing the above, we believed that: 1) the three-dimensional flow basic equation set for turbine machinery which was rigorously derived in Reference [3] by employing arbitrary non-orthogonal curvilinear coordinates and their corresponding non-orthogonal velocity components can be applicable to any complicated boundary conditions. Actual computation showed that it is a feasible and effective method. The use of this coordinate system and its computational method are original. Furthermore, it can be extended to other engineering computations.

2) By introducing the stream function, a second order quasi-linear partial differential equation of the stream function Ψ was established as the major equation in searching for the solution. This not only makes the boundary conditions more rigorous and precise, but also brings about improvements in the numerical solution method.

3) In this paper, with the exception of the density terms in the stream function equation to be solved, the various orders of partial derivative terms of Ψ are placed on the left hand side of the equation. This would reduce, to the extent possible, the lagging quantities in the iteration computational process. This is very favorable to the acceleration of the convergence rate.

4) The direct decomposition of matrices $[L]$ $[u]$ was used to solve the Ψ equation. Due to the fact that the density terms are shifted to the right hand side of the equation, the coefficient matrix is composed of geometric parameters of the mesh which are invariant in the iteration process. Therefore, the matrix decomposition will only have to be carried out once. Furthermore, the density terms are converging more easily. Actual experience showed that this method converges comparatively faster.

5) In the direct matrix solution method, the storage of the coefficient matrix is an important problem. Because the diagonal line numbering and the additional fictitious points methods were used, the internal storage was greatly decreased.

6) When finding density ρ from the stream function Ψ , an internally stored density function table interpolation computation was used. This is favorable to accelerating the computing speed.

7) From the comparison of the calculated results to the analytical solutions and the experimental results, we can see that they are in mutual agreement. There is some difference in the gas entering boundary. This is mainly due to the complicated variation of the blade curve at the gas entering boundary, and the simulated matching of the curve is relatively more difficult. This will require special treatment which will be described in another paper. In addition, for the difference in comparison to the experimental results, the local flow separation is also another reason.

This paper was carried out under the direct guidance of Professor Wu Chung-Hua. We wish to express our deepest gratitude.

REFERENCES

- 1) Wu Chung-Hua: A General Theory of Three-Dimensional Flow in Subsonic or Supersonic Turbomachines of Axial Radial and Mixed Flow Types, ASME Paper No. 50-A-79, Trans ASME Nov. 1952, or NACA TN 2604, 1952.
- 2) Wu Chung-Hua: The Thermoaerodynamic Basic Equations under Static and Moving Coordinates — the action of the viscous force and the physical meaning of the viscosity term, Journal of Mechanical Engineering, Vol. 13, No. 4, December, 1965.

127

- 3) Wu Chung-Hua: The Thermoaerodynamic Basic Equations of Turbine Machinery Employing Non-orthogonal Curvilinear Coordinates and Non-orthogonal Velocity Components, research notebook, 1963.
- 4) Wu Chung-Hua: Lecture note on the three-dimensional flow of turbine machinery, Chinese Technical University, 1975.
- 5) Wu Chung-Hua: The three-dimensional flow basic equations and the solution method of turbine machinery by employing non-orthogonal curvilinear coordinates and non-orthogonal velocity components, a paper presented at the Third International Air Jet Engine Conference. Munich, West Germany, 1976. Journal of Mechanical Engineering, Vol. 15, No. 1, June, 1979.
- 6) Wu Wen-quan: The Major Equations of the S_1 Stream Function Solution by employing non-orthogonal curvilinear coordinates. Research Notebooks, 1970.
- 7) Gostelow, J.P., Potential Flow Through Cascade Extension to an Exact Theory, ARC, CP No. 808, 1964.
- 8) Savage, M., Felix, R., and Emery, J.: High Speed Cascade Tests of a Blade Section Designed for Typical Hub Conditions of High-Flow Transonic Rotors, NACA RM L55F07, 1955.

FLOW FIELD LINE RELAXATION SOLUTION FOR INVERSE PROBLEM OF
FLOW ALONG S_2 RELATIVE STREAM SURFACE EMPLOYING
NON-ORTHOGONAL CURVILINEAR COORDINATES AND CORRESPONDING
NON-ORTHOGONAL VELOCITY COMPONENTS*

Zhurong-guo
(Academia Sinica)

ABSTRACT

Specifically with regard to the calculation of the inverse problem of the S_2 stream surface of a turbomachine, the computer program of the flow field line relaxation solution for the inverse problem of flow along the S_2 stream surface employing arbitrary non-orthogonal curvilinear coordinates and non-orthogonal velocity components was introduced. Furthermore, the differences between this program and the presently commonly used velocity extension method (streamline curvature method) program and the direct matrix solution method program were briefly compared and commented on. The advantages of the flow field line relaxation method are pointed out. Especially when the three-dimensional blade design computation is used, when it is necessary to establish more computational stations along the streamline direction of the blade region, the flow field line relaxation method is worth recommending.

I. Introduction

Since Wu Chung-Hua^[1, 2] established the three-dimensional flow basic equation of the turbomachine and the stream surface theory for the solution of three-dimensional flow in the early

* This paper has been presented in the Second National Engineering Thermal Physics Conference in Haugchow in November 1978.

fifties, great advances have been made in the aerodynamic numerical computations of turbomachines. At the present moment, it has already combined with experiments to become an indispensable powerful tool in the design and development of turbomachines. In the aerodynamic design of turbomachines, the computation of the S_2 stream surface occupies an extremely important position. It determines the flow distribution along the blade height. For the calculation of the S_2 stream surface, much attention was paid to it. Many different numerical methods were developed.

In the selection of the coordinate system, initially the orthogonal cylindrical coordinate system and the corresponding orthogonal velocity components were adopted^[2]. In order to adapt to the various boundary shapes, the three-dimensional flow basic equation set^[4-6] of turbomachines employing non-orthogonal curvilinear coordinate systems and non-orthogonal velocity components was used. By introducing a non-orthogonal curvilinear coordinate system, it can very conveniently transform a physical surface with complicated boundary shape into a rectangular mesh computational plane. In the meantime, it can naturally satisfy the physical condition that the boundary flow direction is tangential to the surface.

In the computation of the S_2 stream surface, from the viewpoint of the equation form and the computation method, there are primarily two types of methods widely used.

The first type is the velocity extension method (streamline curvature method). It is based on the radial component equation of the equation of motion to write the partial differential equation of the velocity along the blade height. For example, it is written in the following form^[1]:

$$\frac{\partial V_s}{\partial r} = \frac{1}{V_s} \left[-\frac{V_\theta}{r} \frac{\partial(V_{\theta r})}{\partial r} + gJ \left(\frac{\partial H}{\partial r} - T \frac{\partial s}{\partial r} \right) - F_r \right] + \frac{\partial V_r}{\partial z} \quad (1)$$

The left hand side of equation (1) is written in the velocity partial derivatives form which is characteristic of this type of solution method. When looking for the solution, first a velocity value $V_{z,h}$ is assumed at a certain radius (such as the inner radius) and then the velocity value along the blade height according to the equation. The flow rate is used to check whether the selected initial velocity is proper. If it is not proper, then another initial value is chosen until the flow rate condition is satisfied. Because the right hand of the equation contains many unknown parameters related to the streamline shape, they can only be replaced by the approximate values. Thus, it requires repeated iteration. /29

For the quantities dependent on the streamline position on the right hand side of the equation, they can be expressed in various forms. Earlier, such as in Reference [1], assuming that the projection of the streamline on the meridian plane is a sinusoidal curve, then the relevant term on the right hand side to the streamline wave was

$$V_z \frac{\partial V_z}{\partial (z/\Delta)} \approx \frac{\pi^2 r_2 - (r_1 + r_2)/2}{2 \Delta} \left(\frac{\Delta}{L}\right)^2 V_z^2 \cos \frac{\pi z}{L}, \quad (2)$$

After that, many authors more directly wrote the $\partial V_z / \partial z$ on the right hand term into a form related to the radius of curvature of the streamline. Therefore, this type of method is also commonly called the streamline curvature method, or it is called the velocity extension method.

The second type is the flow field matrix method or the so-called stream function matrix method. It involves the introduction of the stream function into the continuity equation and the stream function equation is substituted into the equation of motion. Finally, the radial equilibrium equation of motion expressed in the stream function form is obtained. Then, the numerical differential formula is used to write the stream function

differential equation into a difference equation form with respect to each nodal points to obtain the linear algebraic equation set related to the stream function of the nodal points of the entire field. Use the numerical computation methods of the linear algebraic equation set such as the direct matrix decomposition method or the iteration method to solve the stream function values of the nodal points of the entire flow field. Subsequently, other physical quantities such as density, velocity, etc. are determined.

II. The Line Relaxation Solution Computer Program for S_2 Stream Surface Stream Function by Using Non-orthogonal Curvilinear Coordinates and Non-orthogonal Velocity Components

In the past, we have compiled two S_2 computation programs based on the velocity extension method^[7,8]. Due to the slow convergence inside the duct during computation, this more satisfactory computing program was subsequently compiled. With regard to the details and explanation, References [7,8] can be referred to.

1. The Stream Function Equation to be Solved.

The dimensionless form of the S_2 stream surface radial equilibrium equation under arbitrary curvilinear coordinates is ^[4-8]

$$\begin{aligned} & \frac{\sqrt{a_{11}}}{\rho f \sqrt{a_{22}}} \frac{\partial^2 \psi}{\partial (x^2)^2} - 2 \frac{\sin(\theta_1 - \theta_2)}{\rho f} \frac{\partial^2 \psi}{\partial x^1 \partial x^2} + \frac{\sqrt{a_{22}}}{\rho f \sqrt{a_{11}}} \frac{\partial^2 \psi}{\partial (x^1)^2} \\ & + \left[\partial \left(\frac{\sqrt{a_{11}}}{\rho f \sqrt{a_{22}}} \right) / \partial x^1 - \partial \left(\frac{\sin(\theta_1 - \theta_2)}{\rho f} \right) / \partial x^1 \right] \frac{\partial \psi}{\partial x^2} \\ & + \left[\partial \left(\frac{\sqrt{a_{22}}}{\rho f \sqrt{a_{11}}} \right) / \partial x^1 - \partial \left(\frac{\sin(\theta_1 - \theta_2)}{\rho f} \right) / \partial x^2 \right] \frac{\partial \psi}{\partial x^1} = A + F \end{aligned} \quad (3)$$

where

$$A = \frac{\sqrt{a_{11}}}{V_1} \left(-\frac{W_r}{r} \frac{\partial(V_{\theta r})}{\partial x^2} + \frac{\partial I}{\partial x^1} - \frac{RT_1 g_c}{U_A^2} T \frac{\partial s}{\partial x^2} \right) \quad (4)$$

$$F = \left[\frac{\partial(V_{\theta r})}{\partial x^1} + \frac{\sqrt{a_{11}} I_2}{\sqrt{a_{22}} V_1} \frac{\partial(I_{\theta r})}{\partial x^2} \right] \frac{\partial \rho}{\partial x^1} \quad (5)$$

It is briefly noted as

$$A_1 \partial^2 \Psi / \partial (x^2)^2 + A_2 \partial^2 \Psi / \partial x^2 \partial x^1 + A_3 \partial^2 \Psi / \partial (x^1)^2 + A_4 \partial \Psi / \partial x^2 + A_5 \partial \Psi / \partial x^1 = A_6 + F \quad (6)$$

This is the S_2 stream surface radial equilibrium stream function equation to be used in seeking the solution.

2. The Difference Equation and the Iteration Format.

The numerical differentiation is expressed using the three point differential formula [9] as

/30

$$(\partial \Psi / \partial x^2)_{j,k} = C11_k \Psi_{j,k-1} + C12_k \Psi_{j,k} + C13_k \Psi_{j,k+1} \quad (7)$$

$$(\partial \Psi / \partial x^1)_{j,k} = C21_k \Psi_{j-1,k} + C22_k \Psi_{j,k} + C23_k \Psi_{j+1,k} \quad (8)$$

$$(\partial^2 \Psi / \partial (x^2)^2)_{j,k} = D11_k \Psi_{j,k-1} + D12_k \Psi_{j,k} + D13_k \Psi_{j,k+1} \quad (9)$$

$$(\partial^2 \Psi / \partial (x^1)^2)_{j,k} = D21_k \Psi_{j-1,k} + D22_k \Psi_{j,k} + D23_k \Psi_{j+1,k} \quad (10)$$

$$\begin{aligned} (\partial^2 \Psi / \partial x^1 \partial x^2)_{j,k} = & C21_k C11_k \Psi_{j-1,k-1} + C21_k C12_k \Psi_{j-1,k} \\ & + C21_k C13_k \Psi_{j-1,k+1} + C22_k C11_k \Psi_{j,k-1} + C22_k C12_k \Psi_{j,k} \\ & + C22_k C13_k \Psi_{j,k+1} + C23_k C11_k \Psi_{j+1,k-1} + C23_k C12_k \Psi_{j+1,k} \\ & + C23_k C13_k \Psi_{j+1,k+1} \end{aligned} \quad (11)$$

By substituting equations (7)-(11) into equation (6), the difference equation related to the j,k point is obtained. After simplification, it is noted as

$$\begin{aligned} E11 \Psi_{j-1,k-1} + E12 \Psi_{j-1,k} + E13 \Psi_{j-1,k+1} + E21 \Psi_{j,k-1} + E22 \Psi_{j,k} + E23 \Psi_{j,k+1} \\ + E31 \Psi_{j+1,k-1} + E32 \Psi_{j+1,k} + E33 \Psi_{j+1,k+1} = A6_{j,k} + F_{j,k} \end{aligned} \quad (12)$$

With regard to equation (12), it is possible to use various methods to seek the solution. One is the point by point iteration format

$$\begin{aligned} \Psi_{j,k}^{(n)} = & (A6_{j,k}^{(n-1)} + F_{j,k}^{(n-1)} - E11 \Psi_{j-1,k-1}^{(n-1)} - E12 \Psi_{j-1,k}^{(n-1)} - E13 \Psi_{j-1,k+1}^{(n-1)} \\ & - E21 \Psi_{j,k-1}^{(n-1)} - E23 \Psi_{j,k+1}^{(n-1)} - E31 \Psi_{j+1,k-1}^{(n-1)} - E32 \Psi_{j+1,k}^{(n-1)} \\ & - E33 \Psi_{j+1,k+1}^{(n-1)}) / E22, \end{aligned} \quad (13)$$

Using matrices and vectors, it can be expressed as

$$[\Psi]^{(v)} = [B]^{(v-1)} - [M - E][\Psi]^{(v-1)} \quad (14)$$

where [M] is the coefficient matrix, [B] is the vector formed by the right hand terms, and [Ψ] is the stream function vector to be solved.

The second method is to list all the difference equations with respect to all the j,k points in equation (12). Then, an element elimination method is used to solve the linear algebraic equation set related to ψ . The iteration format is

$$\begin{aligned} &E11\Psi_{j-1,k-1}^{(v)} + E12\Psi_{j-1,k}^{(v)} + E13\Psi_{j-1,k+1}^{(v)} + E21\Psi_{j,k-1}^{(v)} + E22\Psi_{j,k}^{(v)} \\ &+ E23\Psi_{j,k+1}^{(v)} + E31\Psi_{j+1,k-1}^{(v)} + E32\Psi_{j+1,k}^{(v)} + E33\Psi_{j+1,k+1}^{(v)} \\ &= A6_{j,k}^{(v-1)} + F_{j,k}^{(v-1)}. \end{aligned} \quad (15)$$

By using matrices and vectors, it can be expressed as

$$[M][\Psi]^{(v)} = [B]^{(v-1)} \quad (16)$$

With regard to the solution of equation (16), it frequently uses the decomposition of the coefficient matrix [M] into the lower triangular matrix [L] and the upper triangular matrix [u], i.e., the so-called large matrix direct decomposition method is used to find the solution.

This program used a piece by piece iteration format, and equation (12) is briefly noted as

$$E1_{i,k}\Psi_{i,k-1}^{(v)} + E2_{i,k}\Psi_{i,k}^{(v)} + E3_{i,k}\Psi_{i,k+1}^{(v)} = B_{i,k}^{(v+1)} \quad (17)$$

For each station j, the column functions form k=2 to k=n-1 in equation (17) together with the two functions $\Psi_{j,1}=0$ and $\Psi_{j,n}=0$ are used to obtain $\Psi_{j,k}^{(v)}$ using the chasing method. This iteration format can be expressed in the following form by using the matrix

and vector form, i.e., $[M]$, $[\phi]$, and $[B]$ in equation (16) are considered to be composed of some submatrices and component vectors. It is written as

$$\begin{bmatrix} [m_{11}] & & & \\ [m_{21}] & [m_{22}] & [m_{23}] & \\ & \ddots & & \\ & & [m_{j,1}] & [m_{j,2}] & [m_{j,3}] \\ & & & \ddots & \end{bmatrix} \begin{bmatrix} [\phi_1] \\ [\phi_2] \\ \vdots \\ [\phi_j] \\ \vdots \end{bmatrix} = \begin{bmatrix} [B_1] \\ [B_2] \\ \vdots \\ [B_j] \\ \vdots \end{bmatrix} \quad (18)$$

Then, each submatrix block and component vector is used as a unit to carry out the iteration computation. After the Ψ component vectors are obtained, it is relaxed one by one, i.e., by the line relaxation or the block iteration method.

It is actually written as

$$[m_{j,1}][\Psi_{j-1}] + [m_{j,2}][\Psi_j] + [m_{j,3}][\Psi_{j+1}] = [B_j]^{(s-1)} \quad (19)$$

The iteration format used is

$$[m_{j,2}][\Psi_j]^{(s)} = [B_j]^{(s-1)} - [m_{j,1}][\Psi_{j-1}]^{(s)} - [m_{j,3}][\Psi_{j+1}]^{(s-1)}. \quad (20)$$

With regard to solving equation (20), the similar large matrix direct decomposition method is used to find the solution. Because the matrix $[m_{j,2}]$ is a diagonal band matrix with a width of three, the computation at this time is much simpler. Its matrix decomposition and the Ψ solution processes can be written into an iterative deduction formula. This is also the so-called chasing solution method. This is a computation method located between large matrix direct decomposition and point by point iteration, which accelerates the convergence rate and does not occupy a lot of internal storage.

3. Finding the Solution for the Main Equation, Using the Chasing Method to Solve the Linear Algebraic Equation Set. /31

With regard to equation (17), by listing all the equations of the station j , the following equation set is obtained:

$$\left. \begin{aligned} \Psi_1 &= 0 & (21-1) \\ E1_1\Psi_1 + E2_1\Psi_2 + E3_1\Psi_3 &= B_1 & (21-2) \\ &\vdots \\ E1_k\Psi_{k-1} + E2_k\Psi_k + E3_k\Psi_{k+1} &= B_k & (21-k) \\ &\vdots \\ \Psi_n &= G & (21-n) \end{aligned} \right\} \quad (21)$$

Write the equations (21-2) to (21-(n-2)) in equation (21) one by one in the following standardized form

$$\Psi_k + b_k\Psi_{k+1} = g_k \quad (22)$$

With respect to (21-2), we have

$$\Psi_2 + (E3_1/E2_1)\Psi_3 = B2/E2_1 - (E1_1 \cdot \Psi_1)/E2_1 \quad (23)$$

i.e.

$$b_2 = E3_1/E2_1 \quad (24)$$

$$g_2 = B2/E2_1 - (E1_1 \cdot \Psi_1)/E2_1 \quad (25)$$

Substituting the standardized form $\Psi_{k-1} + b_{k-1}\Psi_k = g_{k-1}$ into equation (21-k), we get

$$\Psi_k + [E3_k/(E2_k - E1_k b_{k-1})]\Psi_{k+1} = (B_k - E1_k g_{k-1})/(E2_k - E1_k b_{k-1})$$

Comparing to the standardized form (22), we have

$$b_k = E3_k/\omega_k \quad (26)$$

$$g_k = (B_k - E1_k g_{k-1})/\omega_k \quad (27)$$

$$\omega_k = E2_k - E1_k b_{k-1} \quad (28)$$

According to equations (24)-(28), all the w_k , b_k , and g_k are obtained first. They can be substituted into equation (22) to obtain the entire ψ_k values.

4. The Computation of Other Parameters.

The automatic formation of the mesh nodal points and the computation of the geometric parameters:

In order to reduce the input of original data, the curvilinear mesh was formed automatically by the machine. It was regulated that the x^2 coordinate lines from the root to the top of the blade are second order curves. However, the coordinates of the root and the top in the x^1 direction were completely given in order to adapt to the arbitrary shape of the meridian duct. The computation of the mesh was given in terms of the maximum arch degree DZ and the distribution coefficient x of the nodal point along the blade height:

/32

$$R_k = R_1 + x_k(R_n - R_1) \quad (29)$$

$$Z_k = Z_1 + x_k(Z_n - Z_1) + DZ[1 - 4(x_k - 0.5)^2] \quad (30)$$

The maximum arch degree DZ was given at the front and rear fringes of the blade. As for the other stations, it was calculated automatically according to a linear distribution.

After the nodal coordinates had been computed, then the following geometric parameters were calculated:

$$\theta_1 = -\arctg(dz/dr)_{x^1=const} \quad (31)$$

$$\theta_1 = \arctg(dr/dz)_{x^1=const} \quad (32)$$

$$\sqrt{a_{22}} = \sqrt{(\partial z/\partial x^1)^2 + (\partial r/\partial x^1)^2} \quad (33)$$

$$\sqrt{a_{11}} = \sqrt{(\partial z/\partial x^1)^2 + (\partial r/\partial x^1)^2} \quad (34)$$

The dimensionless computational equations for the physical quantities are given in the following:

The $V_{\theta r}$ of the blade spacing stations along the blade height were given and the $V_{\theta r}$ values in the blade duct were determined using the coefficient:

$$V_{\theta r} = V_{\theta r, in} + \xi_{1, \theta r} [(V_{\theta r})_{out} - (V_{\theta r})_{in}] \quad (35)$$

The coefficient $\xi_{v\theta r}$ is usually given based on S_1 stream surface computation

$$W_{\theta} = V_{\theta r} / r - \Lambda r \quad (36)$$

$$H_{i+1} = H_i + \Lambda [(V_{\theta r})_{i+1} - (V_{\theta r})_i] \quad (37)$$

$$l = H - \Lambda V_{\theta r} \quad (38)$$

for a moving blade $\Lambda=1$, for a static blade $\Lambda=0$.

$$V_1 = -(\partial \Psi / \partial x^1) / (\rho f \sqrt{a_{11}}) \quad (39)$$

$$V_2 = (\partial \Psi / \partial x^2) / (\rho f \sqrt{a_{22}}) \quad (40)$$

$$T_{i+1} = T_i + U_{\theta}^2 (\kappa - 1) [(H - V^2/2)_{i+1} - (H - V^2/2)_i] / (\kappa R T_i g_c) \quad (41)$$

$$V^2 = V_1^2 + V_2^2 + 2V_1 V_2 \sin(\theta_1 - \theta_2) + V_0^2 \quad (42)$$

$$\rho_{i+1} = \rho_i (T_{i+1}/T_i)^{1/(\kappa-1)} \cdot e^{-(\epsilon_{i+1}-\epsilon_i)} \quad (43)$$

$$p = T \rho \quad (44)$$

$$\Delta s = \ln(P_0/P'_0) \text{ (static blade)} \quad (45)$$

$$\Delta s = \kappa / (\kappa - 1) \cdot \ln \{ (H_i/H'_i) / [\eta (H_i/H'_i - 1) + 1] \} \quad (46)$$

for a moving blade during compression process.

$$\Delta s = \kappa / (\kappa - 1) \cdot \ln \{ (H_i/H'_i) / [\eta (H_i/H'_i - 1) + 1] \} \quad (47)$$

for a moving blade during expansion process.

The computational formulas related to the output printing are as follows:

total temperature

$$T_0 = H \cdot U_A^2 (\kappa - 1) / \kappa \cdot R \cdot T_0^0 \cdot g_c \quad (48)$$

total pressure

$$p_0 = (T/T_0)^{\kappa/(\kappa-1)} \cdot p \quad (49)$$

Mach number

$$M = V / \sqrt{\kappa T R T_0^0 g_c U_A^2} \quad (50)$$

diffusion factor

$$D = 1 - (W_{in}/W_{out}) + [(W_{\varphi r})_{out} - (W_{\varphi r})_{in}] / [\lambda \cdot W_{in} \cdot (r_{in} + r_{out})] \quad (51)$$

/33

efficiency

$$\eta = [(p_{0out}/p_{0in})^{(\kappa-1)/\kappa} - 1] / (T_{0out}/T_{0in} - 1) \quad (52)$$

pressure coefficient

$$C_p = (p_{0out} - p_{in}) / (p_{0in} - p_{in}) \quad (53)$$

Meridian inclination angle of the streamline

$$\sigma \approx \text{arctg}(R'_1) \cdot (180/\pi) \quad (54)$$

ϕ coordinate of the stream surface

$$\varphi_i = \varphi_{i-1} + \Delta l [(W_{\varphi}/W_m)_{i-1} + (W_{\varphi}/W_m)_i] / (2R_i)$$

where

$$\Delta l = \sqrt{\Delta r^2 + \Delta z^2} \quad (55)$$

thickness of the stream slice of the S_1 stream surface

$$r_1 = \xi_0 \cdot G \cdot \xi P / [200(P - t)\pi\gamma\rho W_m] \quad (56)$$

the flow angle

$$\beta_m = \arctg(W_m/W_q) \quad (57a)$$

$$\beta_z = \arctg(W_z/W_\phi) \quad (57b)$$

5. Brief Description of the Program.

The computation program was compiled using the ALGOL language on a TQ-16 machine. The computation procedures of the program are as follows:

1) Input the original data, including incoming flow conditions, the geometric parameters of each blade section, loss coefficients, $V_{\theta r}$ the variational coefficients of $V_{\theta r}$ in the duct, the blade thickness distribution and the effect coefficient, the flow rate coefficient, densities, and other parameters.

2) Calculate the geometric parameters for the mesh nodal points according to equations (29)-(34).

3) Make them dimensionless.

4) Form the initial value fields of Ψ and ρ in preparation for iterative computation.

5) Calculate parameters such as $V_{\theta r}$, W_ϕ , H , l , s , T , and ρ .

6) Find the value of Ψ using the chase method one after the other along the j stations. After line relaxation, the new Ψ distribution of the entire field is obtained.

7) Calculate V_1 and V_2 .

8) Check the errors of ψ and ρ . If the accuracies are not enough, then go back to step 5) to repeat the next iterative computation.

9) If the computational accuracy is sufficient, then print out the computed results. The output of results can be in the dimensional or dimensionless form according to the need. It is also possible to have the output according to the nodal point position or the streamline position. The computational accuracy can be given according to the need.

III. The Comparison of Several Numerical Computational Methods and Discussion

Although, whether a design is successful or not is not completely determined by the computational method adopted and, to a great extent, is decided by the design parameters and experimental data chosen such as whether the selected losses, attack angle of the blade, and lagging angle are rational. However, different computational methods, due to the different internal storage capacity requirements and the iterative convergence rates, have different computational costs for numerical computations. Sometimes, the difference can be even very large.

1. The Velocity Extension Method.

Its major characteristic is to alternatively use the equation of motion and the continuity equation to carry out the iteration. Therefore, the efficiency of computation is, to a great extent, determined by whether this mutual iterative correction process can converge rapidly or not. However, this type of mutual iteration does not converge rapidly under all conditions. Especially when

/34

many stations are established in the blade duct, the computation diverges easily. In order to prevent the computational process from diverging, therefore, it is necessary to use a low relaxation factor α , which is less than 1 when calibrating the position of the streamline. According to our trial computation practice and related analysis on the convergence of iteration^[10], under the condition that other parameters are unchanged, the magnitude of the mesh Δm in the streamline direction is a major factor affecting the convergence. Furthermore, there is a quantitative relationship that the relaxation factor α is proportional to Δm^2 . With respect to the computation of a two level fan, when the aerodynamic parameters are identical and only the mesh densities in the streamline direction are different, there are the following effects: a) when the computational stations are only taken in between the blade gaps, the relaxation factor can be chosen as 0.3. After 12 iterations, the accuracy of the streamline position can reach 0.98×10^{-3} ; b) when the mesh in the streamline direction becomes denser, each blade zone has three computational stations added to it. That is, when one computational station is added at the front and rear fringes as well as in the middle of the blade, then the convergence becomes apparently poorer. The relaxation factor can only be chosen as 0.04. In order to reach the same accuracy of 0.99×10^{-3} , the number of iterations is increased to 80; c) if we further densify the mesh in the streamline direction, when the computational stations in the blade region are increased to 6 stations, it becomes divergent easily when the relaxation factor exceeds 0.01. After 273 iterations using a 0.01 relaxation factor, the accuracy of the streamline position is merely 0.58×10^{-2} . Therefore, we can see that the velocity extension method (streamline curvature method) is more suited for the aerodynamic computation in the situation of blade gap station of a large mesh spacing in the streamline direction. When the computation enters the blade region and it is required to set up more computational stations, its convergence becomes very poor.

2. Direct Flow Field Matrix Decomposition Method.

Its greatest special feature is that once the coefficient matrix $[M]$ is decomposed, when the B value of the right hand term is determined, the precise solution of Ψ on all the nodal points can be directly calculated without the need of any iterative process. Therefore, for the calculation of incompressible fluids and iso-energetic iso-enthalpic axial symmetric flows along the blade height, it is possible to obtain the Ψ value of the entire field by one computation. The computation is more fast and accurate. However, there is a very large coefficient matrix $[M]$ in the direct matrix decomposition method. The storage capacity occupied by the coefficient matrix and the $[L]$ and $[u]$ after decomposition is considerable. It is proportional to the number of stations along the streamline direction and it is proportional to the square of the number of stations n along the blade height direction, i.e., $\propto mn^2$. In addition, with regard to the usual S_2 stream surface aerodynamic calculation, the right hand term B of equation (16) must still be iterated. However, at this time we can use a very large relaxation factor. It is possible to obtain a solution with satisfactory accuracy after a few iterations.

3. The Line Relaxation Iteration Solution of the Flow Field Matrix.

This program is well suited for the three-dimensional flow design blades when it is necessary to set up more computational stations in the computation of the S_2 stream surface for the mutual iteration with the S_1 stream surface^[11]. Under this condition, the convergence rate of the velocity extension method is too slow. The typical relaxation factor is about 0.01. In order to satisfy the 0.1% accuracy, it requires about 200 iterations. The typical relaxation factor of the flow field matrix line relaxation program is 1-1.65. To satisfy the 0.1% accuracy, 15-20 iterations will do. It is 10 times faster than the velocity extension method.

The flow field matrix direct decomposition method, because of the high internal storage requirement, such as when $m=47$, $n=11$, the nodal point number is 517 and the internal storage capacity required by the coefficient matrix is about 28000 units, is more difficult to compute on a 32K internal storage computer. However, the line relaxation method can allow about 1200 nodal points on a 32K internal storage computer without using external storage.

Therefore, in this situation the line relaxation computation program avoids the shortcomings of slow convergence and high iteration numbers of the velocity extension method and it also overcomes the difficulty of the high internal storage capacity requirement of the direct matrix decomposition method. It maintains the advantages of the low internal storage capacity requirement of the velocity extension method and the fast convergence rate of the direct matrix decomposition method. It is indeed a good method which is worthwhile recommending.

This work was carried out under the direct guidance of Professor Wu Chung-Hua. We wish to express our deepest gratitude.

REFERENCES

- 1) Wu Chung-Hua and Wolfenstein, L., Application of Radial-Equilibrium Condition to Axial-Flow Compressor and Turbine Design, NACA Rep. 955, 1950.
- 2) Wu Chung-Hua, A General Theory of Three-Dimensional Flow in Subsonic and Supersonic Turbomachines of Axial, Radial, and Mixed-Flow Types. ASME Paper No. 50-A-79, Trans., Nov. 1952, or NACA TN 2604, 1952.
- 3) Wu Chung-Hua: Thermoaerodynamic Basic Equations under the Static and Moving coordinates — the action of the viscous force and the physical meaning of the viscosity term, Journal of Mechanical Engineering Vol. 13, No. 4, December 1965. /35
- 4) Wu Chung-Hua: The Thermoaerodynamic basic equations of a turbomachine using non-orthogonal curvilinear coordinates and non-orthogonal velocity components, Research Notebook, 1963.

- 5) Wu Chung-Hua: Lecture Notes on Three-dimensional flow of Turbomachines, Chinese Technical University, 1975.
- 6) Wu Chung-Hua, Three-Dimensional Turbomachine Flow Equations Expressed with respect to Non-Orthogonal Curvilinear Coordinates and Methods of Solution, Proceedings of 3rd ISABE 1976, pp. 233-252, or Journal of Mechanical Engineering, No. 15, Vol. 1, June 1979.
- 7) Group No. 4, Room No. 5, Institute of Mechanics: S_2 Stream Surface Equation of Turbomachines under arbitrary curvilinear coordinates and the computer program. Work Report of the Institute of Mechanics, 1975.
- 8) Group No. 4, Room No. 5, Institute of Mechanics: The Computer Program of the S_2 Stream Surface of Turbomachines under arbitrary curvilinear coordinates using the stream function line relaxation solution method, Work Report, March, 1977.
- 9) Wu Chung-Hua: Non-equal-distance Numerical Differential Equation and Coefficient table and their applications to the numerical solution of partial differential equations, Science Publications 1959.
- 10) Room No. 3 of the Computer Center of Academia Sinica: Solving the Aerodynamic Problems of Turbomachinery Using the Streamline Iteration Method, Work Report, 1975.
- 11) Wu Wen-quan, Shu Rong-guo, Liu Cui-e, Computer Programs of Flow Calculation on Relative Stream Surfaces S_1 and S_2 . Employing Non-Orthogonal Curvilinear Coordinates and Non-Orthogonal Velocity Components and Their Application to the Design of Turbomachine Blades Based on Three-Dimensional Flow, Proceedings of 4th ISABE, 1979, pp. 277-287.

COMPUTER PROGRAM FOR DIRECT PROBLEM OF FLOW ALONG S_2
RELATIVE STREAM SURFACE EMPLOYING NON-ORTHOGONAL
CURVILINEAR COORDINATES FOR TURBOMACHINE*

Ding Yun-Feng and Deng Zi-Tong
(Computer Center, Academia Sinica)

ABSTRACT

With regard to the direct problem of S_2 stream surface of a turbomachine with non-orthogonal curvilinear coordinates (subsonic conditions), a convergence algorithm was realized on the computer. The verifying computation of a highly loaded axial-flow two stage fan showed that the computed results and experimental results are in agreement.

/36

The principal deviation equation used was the newly obtained non-linear form--equation (8). In comparison to the conventionally used linear form--equation (13), when the high subsonic velocity region was comparatively large, the new algorithm improved the convergence of the numerical solution process.

I. INTRODUCTION

The flow inside a turbomachine is very complicated. The three-dimensional flow theory presented by Professor Wu Chung-Hua in the early 50's is still used as the basis for the computation of internal flow motion of turbomachines.

In [1], the principal equations of flow along the S_1 stream surface and S_2 stream surface under orthogonal coordinates were derived in linear and non-linear forms. In the early 60's, the principal equations of the motion along the S_1 stream surface and S_2 stream surface using non-orthogonal curvilinear coordinates were derived in [2-4] in a linear form. [1] believed that it is more convenient to use the

linear form of the principal equation for numerical solution for subsonic conditions.

Along with the development of electronic computers, in the mid-60's the three-dimensional flow theory began its computer programming realization stage. For over a decade up to the present, the principal derivation equation has been the linear form by tradition.

This paper derived the non-linear form principal equation of the direct problem for S_2 stream surface using non-orthogonal curvilinear coordinates. It is used as the starting equation in the numerical solution. The difference equation of the stream function ψ is solved by using the super relaxation iteration method. Computations were also made with the principal equations in a linear form. A comparison of the two methods showed that the new method improved the convergence better in the high subsonic velocity region. In the meantime, with regard to high parameter conditions, measures were taken to gradually increase the parameters and to correct the gas entrance angle.

The program was compiled on a TQ-16 computer using ALGOL-60 language. It is capable of analyzing the aerodynamic properties of turbomachines (under subsonic conditions). It is able to calculate the entire flow field of a two-stage blade at once. The computed results agree well with the experimental results.

II. BASIC EQUATIONS

Non-orthogonal curvilinear coordinates (x^1, x^2) were used on the meridian plane. For these coordinates, the wheel shell line, the wheel boss line and the projections of the front and rear fringes of the blade on the meridian plane can all be selected as the x^1 line or the x^2 line. Therefore, it is not only general but is also convenient to treat the boundary conditions.

* This paper has been presented at the 2nd National Engineering Thermal Physics Conference in Hangchow in November 1978.

For a moving blade, let us choose a moving coordinate system (x^1, x^2, ϕ) which rotates at an angular speed ω with the moving blade. The remaining are static coordinates (x^1, x^2, θ) . Under the assumptions that it is stable and adiabatic, the flow on the S_2 stream surface satisfies the equations [2-5].

Continuity equation

37

Equation of motion

$$\frac{\partial}{\partial x^1} (f \rho W^1 \sqrt{a_{11}}) + \frac{\partial}{\partial x^2} (f \rho W^2 \sqrt{a_{11}}) = 0 \quad (1)$$

x^1 direction:

$$\begin{aligned} \frac{W^2}{\sqrt{a_{11}}} \left\{ \frac{\partial}{\partial x^1} [(W^1 \sin(\theta_1 - \theta_2) + W^2) \sqrt{a_{11}}] - \frac{\partial}{\partial x^2} [\sqrt{a_{11}} (W^1 \right. \\ \left. + W^2 \sin(\theta_1 - \theta_2))] \right\} + \frac{W_\phi}{r} \frac{\partial (V_{\theta r})}{\partial x^1} - \frac{\partial l}{\partial x^1} \end{aligned} \quad (2)$$

x^2 direction:

$$+ T \frac{\partial s}{\partial x^1} = -f_1 = \frac{\partial \varphi}{\partial x^1} \frac{d(V_{\theta r})}{dt}$$

$$\frac{\partial}{\partial x^2} [(W^1 + W^2 \sin(\theta_1 - \theta_2)) \sqrt{a_{11}}] - \frac{\partial}{\partial x^1} [(W^1 \sin(\theta_1 - \theta_2) \quad (3)$$

Energy equation:

$$+ W^2) \sqrt{a_{11}}] = \frac{\sqrt{a_{11}}}{W^1} \left[-\frac{W_\phi}{r} \frac{\partial}{\partial x^2} (V_{\theta r}) + \frac{\partial l}{\partial x^2} - T \frac{\partial s}{\partial x^2} - f_2 \right]$$

$$\frac{dl}{dt} = 0 \quad (4)$$

i.e., l is a constant along the streamline (relative streamline in the dynamic blade region). We must notice that l is not continuous on the boundary of the dynamic and static regions. The gap value is $\omega r V_\theta / g_c J$, i.e., the constant has a different value in each region (because $l = H - Q r V_\theta / g_c J$).

Thermodynamic relations:

$$l = c_p T + [(W)^2 - Q^2 r^2] / 2 g_c J \quad (5)$$

$$ds = (d \ln T - (\kappa - 1) d \ln \rho) R / J(\kappa - 1) \quad (6)$$

where: f is the blade thickness effect coefficient, the specific heat ratio $k = k(T)$, the isobaric specific heat

$$\begin{aligned} c_p &= R \kappa / (\kappa - 1) J, \quad V_\theta = W_\phi + Q r, \\ (W)^2 &= (W^1)^2 + (W^2)^2 + 2 W^1 W^2 \sin(\theta_1 - \theta_2) + W_\phi^2, \\ W_\phi &\approx W^1 d_1, \quad d_1 = \cos \theta_1 \cdot \lg \gamma, \end{aligned}$$

$$\Omega = \begin{cases} \omega & \text{(dynamic coordinate system)} \\ 0 & \text{(static coordinate system)} \end{cases}$$

$$f_1 = \frac{\partial \psi}{\partial x^1} \frac{d(V_{or})}{dt},$$

$$a_{ii} = \left(\frac{\partial z}{\partial x^i} \right)^2 + \left(\frac{\partial r}{\partial x^i} \right)^2, \quad a_i = \sqrt{a_{ii}} \quad (i = 1, 2),$$

$$\theta_1 = \arctg \left(\frac{\partial r}{\partial x^1} / \frac{\partial z}{\partial x^1} \right), \quad \theta_2 = \arctg \left(- \frac{\partial z}{\partial x^2} / \frac{\partial r}{\partial x^2} \right).$$

38

The geometric parameters γ and ϕ of S_2 stream surface are not continuous at the boundary between the static and dynamic regions.

The principal derivation equations: From equation (1), let us define the stream function Ψ :

$$\frac{\partial \Psi}{\partial x^2} = f \rho W^1 \sqrt{a_{22}} / K \quad (7.1)$$

$$\frac{\partial \Psi}{\partial x^1} = - f \rho W^2 \sqrt{a_{11}} / K \quad (7.2)$$

K is the flow rate coefficient. Using equations (5), (6) and (7), it is possible to transform equation (3) into

$$\begin{aligned} & \frac{a_2}{a_1} (A^2 + a^2 - (W)^2) \frac{\partial^2 \Psi}{(\partial x^1)^2} - 2[(a^2 - (W)^2) \sin(\theta_1 - \theta_2) \\ & + A \cdot B] \frac{\partial^2 \Psi}{\partial x^1 \partial x^2} + \frac{a_1}{a_2} [(1 + d_1^2)(a^2 - (W)^2) + B^2] \frac{\partial^2 \Psi}{(\partial x^2)^2} \\ & = f \rho (a^2 - (W)^2) \left\{ \frac{a_1}{W^1} J g_c \left(\frac{\partial I}{\partial x^1} - \frac{RT}{J} \frac{\partial s^*}{\partial x^2} - f_2 \right) - W^1 \frac{\partial a_1}{\partial x^2} \right. \\ & - W^2 a_1 \frac{\partial \sin(\theta_1 - \theta_2)}{\partial x^2} + W^2 \frac{\partial a_2}{\partial x^1} + W^1 a_2 \frac{\partial \sin(\theta_1 - \theta_2)}{\partial x^1} \\ & + \frac{a_1}{a_2} (1 + d_1^2) W^1 \frac{\partial a_2}{\partial x^2} - \frac{W^2 a_2}{a_1} \frac{\partial a_1}{\partial x^1} - a_1 d_1 \left(2\Omega + \frac{W^1 d_1}{r} \right) \frac{\partial r}{\partial x^2} \\ & - W^1 d_1 a_1 \frac{\partial d_1}{\partial x^2} \left. \right\} - a^2 f \rho \left(a_1 B \frac{\partial s^*}{\partial x^2} - a_2 A \frac{\partial s^*}{\partial x^1} \right) \\ & + f \rho B a_1 \left\{ \frac{\partial}{\partial x^2} \left(g_c J I + \frac{\Omega^2 r^2}{2} \right) + \frac{a^2}{f} \frac{\partial f}{\partial x^2} - (W^1)^2 d_1 \frac{\partial d_1}{\partial x^2} \right. \\ & - W^1 W^2 \frac{\partial \sin(\theta_1 - \theta_2)}{\partial x^2} + \frac{W^1 B}{a_2} \frac{\partial a_2}{\partial x^2} + \frac{W^2 A}{a_1} \frac{\partial a_1}{\partial x^2} \left. \right\} \\ & - f \rho A a_2 \left\{ \frac{\partial}{\partial x^1} \left(g_c J I + \frac{\Omega^2 r^2}{2} \right) + \frac{a^2}{f} \frac{\partial f}{\partial x^1} - (W^2)^2 d_2 \frac{\partial d_2}{\partial x^1} \right. \\ & - W^1 W^2 \frac{\partial \sin(\theta_1 - \theta_2)}{\partial x^1} + \frac{W^1 B}{a_2} \frac{\partial a_2}{\partial x^2} + \frac{W^2 A}{a_1} \frac{\partial a_1}{\partial x^1} \left. \right\} \end{aligned} \quad (8)$$

where

$$A = W^2 + W^1 \sin(\theta_1 - \theta_2), \quad B = W^2 \sin(\theta_1 - \theta_2) + W^1(1 + d_1^2).$$

Equation (8) is hyperbolic form when $W > a$, elliptical when $W < a$.

Equations to calculate enthalpy s and density ρ : The viscous force was neglected in the equation of motion. However, it is possible to realize part of the viscosity effect through the calculation of enthalpy with the given static blade total pressure loss coefficient σ and the dynamic blade efficiency η . When passing through the static blade and dynamic blade (compressor), the enthalpy increments along the streamline are

$$\Delta s^* = -\ln \sigma \quad \text{static blade} \quad (9.1)$$

$$\Delta s^* = \frac{\kappa}{\kappa - 1} \ln \frac{H_t/H_l}{1 + \eta(H_t/H_l - 1)} \quad \text{dynamic blade} \quad (9.2)$$

The subscripts, l , t , represent the front and rear fringes, respectively. $S^* = s \cdot J/R$. The enthalpy is calculated according to the predetermined distribution in the blade array.

The computation of ρ was obtained by integrating equation (6) along the streamline. We obtained

$$\rho = \rho_a (T/T_a)^{\frac{1}{\kappa-1}} e^{-\Delta s^*} \quad (10)$$

Boundary conditions: The inlet gas flow parameters are given. The wheel shell line and wheel boss line are streamlines. The outlet conduit is properly extended when necessary to have axial gas exit to make $W^2 = 0$. Thus, the boundary conditions are: inlet $\Psi = \Psi_a$, wheel boss $\Psi = 0$, wheel shell $\Psi = G$, outlet

39

$$\frac{\partial \Psi}{\partial x^1} = 0.$$

III. THE SUPER RELAXATION SOLUTION METHOD AND CONVERGENCE ALGORITHM AND RESULTS

If we assume that the flow in the gap is an axial symmetric flow, a unified solution can be sought for the dynamic blade region and the

static blade region simultaneously. This program is capable of calculating seven blade sections, including the upstream region, the guiding blade, the two-stage blade and the downstream region. In the x^1 direction, a three-point unequal distance numerical differential equation was used. In the x^2 direction, it was equally divided according to the duct height of the loop using the center difference equation. By using a nine-point difference form, the difference equation (8) is transformed into a difference equation.

$$\begin{aligned} Q_{1,i,k}\Psi_{i-1,k-1} + Q_{2,i,k}\Psi_{i,k-1} + Q_{3,i,k}\Psi_{i+1,k-1} + Q_{4,i,k}\Psi_{i-1,k} + Q_{5,i,k}\Psi_{i,k} \\ + Q_{6,i,k}\Psi_{i+1,k} + Q_{7,i,k}\Psi_{i-1,k+1} + Q_{8,i,k}\Psi_{i,k+1} + Q_{9,i,k}\Psi_{i+1,k+1} \\ + Q_{10,i,k} = 0 \end{aligned} \quad (11)$$

Using the super relaxation method to solve the difference equation (11), the $\Psi_{i,k}$ solved from equation (11), is recorded as $\tilde{\Psi}_{i,k}^{(v_n+1)}$. Then

$$\Psi_{i,k}^{(v_n+1)} = \Psi_{i,k}^{(v_n)} - \alpha(\Psi_{i,k}^{(v_n)} - \tilde{\Psi}_{i,k}^{(v_n+1)}) \quad (12)$$

where α is the super relaxation factor, n is the number of times to find coefficients Q_1 - Q_{10} and p_n is the iteration number of Ψ under the coefficients which are found in the n th time. Iterations are carried out until

$$d^{(v_n+1)} = \max_i |(\Psi^{(v_n+1)} - \Psi^{(v_n)}) / \Psi^{(v_n)}|_{i,k} < \varepsilon_p$$

The solution at this time is noted as $^{(n+1)}\Psi_{i,k}$, which represents the solution of Ψ with the coefficients $Q_1^{(n)} - Q_{10}^{(n)}$ of the n th time. This is the iteration of Ψ which is called the outer loop.

Then, the $^{(n+1)}\Psi_{i,k}$ and $^{(n)}\rho_{i,k}$ obtained are used to calculate $W^1, W^2, W, V_\theta, T, I, s^*$, etc. Equation (10) is used to calculate $\rho^{(v_n+1)}$, and iterated until $|(\rho^{(v_n+1)} - \rho^{(v_n)}) / \rho^{(v_n)}| < \varepsilon_p$. The ρ obtained at this time is called $^{(n+1)}\rho_{i,k}$. Therefore, new coefficients $Q_1^{(n+1)} - Q_{10}^{(n+1)}$ are obtained. This is the iteration of ρ which is called the inner loop.

Repeat the inner and outer loop until $|(^{(n+1)}\Psi - ^{(n)}\Psi) / ^{(n)}\Psi| < \varepsilon_\Psi$

There is no general proof on the convergence of the aforementioned Ψ - ρ iteration process. With regard to the S_2 stream surface direct flow problem, the convergent algorithm under high parameters condition is an important problem because:

(1) the equation is non-linear, as the M number approaches 1, the degree of non-linearity becomes larger.

(2) the $\text{tg}\gamma$ term in the coefficient of the equation has a discontinuity. Furthermore, it is not easy to provide an accurate value. This may cause the V_θ obtained to be discontinuous. Very frequently in the inner loop to find ρ the value of ρ is too small to be rational and T appears to be a negative value. These would cause the iterations to fail.

Specifically with respect to these two parts, this paper adopted the following methods:

1) the gradual raising of the computational parameters. That is to gradually raise the inlet velocity or gradually increase the S_2 stream surface parameter d_1 .

2) the correction of the S_2 stream surface geometric parameters. This is to consider that the gas exit angle β_2 of each blade array is given and unchanged and the gas entrance angle β_1 is determined by the gas exit condition of the preceding blade (here it is assumed that $\gamma \simeq \beta$. When the model is built on a cylindrical surface, β is identical to γ). The condition used is that in the bladeless regions. $V_\theta r$ remains a constant along the streamline. The $\text{tg}\gamma$ in the blade array varies according to the defined regularity. This newly defined $\text{tg}\gamma$ is used to recalculate the flow on the corrected S_2 stream surface until the difference in gas entrance angles before and after the correction is within the error range required.

40

These measures are taken according to the need. Usually, they are used only in high parameter conditions.

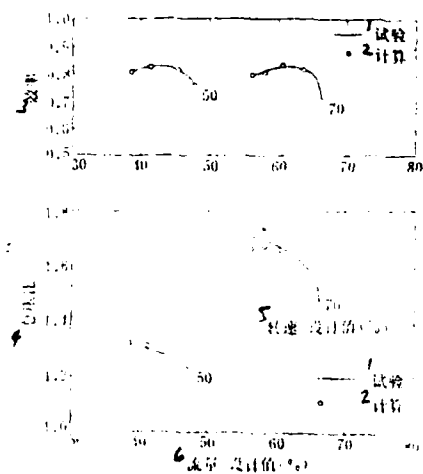


Figure 1. The total characteristics of a two-stage fan
1--efficiency; 2--total compression ratio; 3--experimental; 4--calculated; 5--revolving speed, designed value (%); 6--experimental; 7--calculated

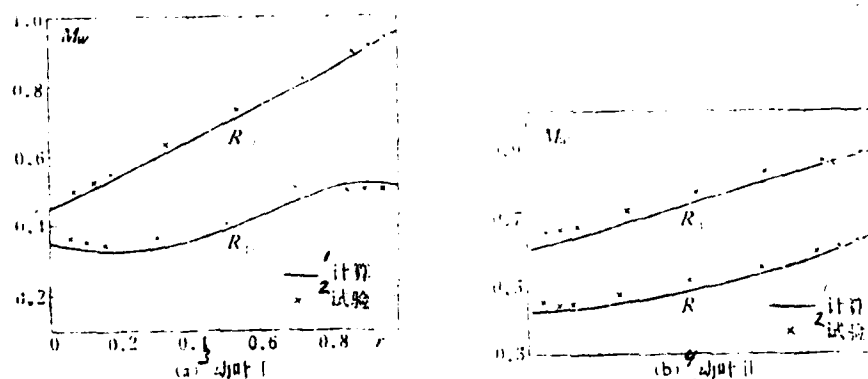


Figure 2. The radial distribution of M_w at the front and rear fringes of a dynamic blade
1--calculated; 2--experimental; 3-- (a)dynamic blade I; 4--calculated; 5--experimental; 6-- (b)dynamic blade II

For a highly loaded two-stage axial flow fan [6], the working conditions corresponding to velocity $c_{0.5}^{-1} 50$ and 70 were computed*. There are four points for the 50% working condition and five points for the 70% working condition. They were marked as 50-1, -2, -3, -4, and 70-1, -2, -3, -4, -5, respectively. In the computation, 48 stations were setup in the x^1 direction. Seven stations were set up in one blade section in which four stations were in the blade, one station each at the front and rear fringes and one station in the gap. 11 stations were set up in the x^2 direction. There were a total of 528 nodal points. The maximum corresponding M number for the 70 working conditions was always above 0.95. The maximum relative M number of 70-1 was 0.9852. When β_1 was not corrected, the numbers of inner and outer loop iterations for the 50 and 70 working conditions were 7 and 25, respectively. The iterations of Ψ were about 100 and 200 times, respectively. The computer time was four minutes and nine minutes, respectively. The correction of β_1 required approximately 10 minutes of computer time.

The calculated results and the experimental results are very consistent. Figure 1 is the total characteristics of a two-stage fan. Figure 2 is the radial distribution of the relative number M at the front and rear fringes of the dynamic blade for the 7-4 working condition. Figure 3 is the streamline pattern.

IV. DISCUSSION OF THE PRINCIPAL EQUATION

Substituting equations (7.1), (7.2) into equation (3), we can get

$$\begin{aligned} & \frac{1}{a_1^2} \frac{\partial^2 \Psi}{(\partial x^1)^2} + \frac{1 + d_1^2}{a_1^2} \frac{\partial^2 \Psi}{(\partial x^2)^2} - \frac{2 \sin(\theta_1 - \theta_2)}{a_1 a_2} \frac{\partial^2 \Psi}{\partial x^1 \partial x^2} - \frac{f \rho}{a_1 a_2} \left\{ \frac{\partial}{\partial x^2} \left(\frac{\sin(\theta_1 - \theta_2)}{f \rho} \right) \right. \\ & - \frac{\partial}{\partial x^1} \left(\frac{a_2}{a_1 f \rho} \right) \left. \right\} \frac{\partial \Psi}{\partial x^1} + \frac{f \rho}{a_1 a_2} \left\{ \frac{\partial}{\partial x^2} \left(\frac{a_1}{a_2 f \rho} \right) + \frac{d_1 a_1}{r} \frac{\partial}{\partial x^2} \left(\frac{d_1 r}{f \rho a_2} \right) \right. \\ & - \frac{\partial}{\partial x^1} \left(\frac{\sin(\theta_1 - \theta_2)}{f \rho} \right) \left. \right\} \frac{\partial \Psi}{\partial x^2} - \frac{f \rho}{K a_1} \left\{ \frac{g_c}{W^1} \left[J \left(\frac{\partial l}{\partial x^2} - \frac{RT}{J} \frac{\partial s^*}{\partial x^2} \right) \right. \right. \\ & \left. \left. - \frac{\partial \varphi}{\partial x^2} \frac{d(V_{\theta r})}{ds} - 2 Q d_1 \frac{\partial r}{\partial x^2} \right] \right\} = 0 \end{aligned} \quad (13)$$

* i.e., the conditions when the rotating speeds are 50% and 70% of the designed revolving speed.

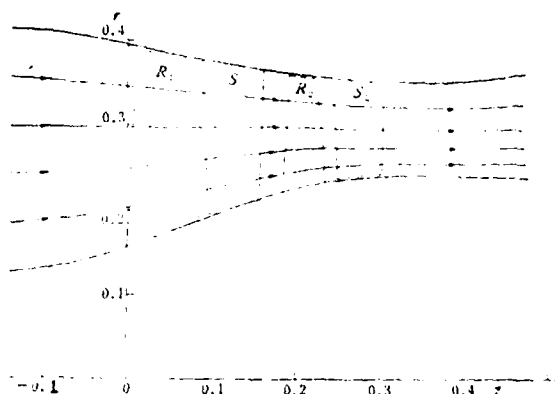


Figure 3. The projections of the streamline on the meridional plane

This is the linear form principal equation. The term $\partial \rho / \partial x^i (i = 1, 2)$ is included which inexplicitly contains second order derivative terms of Ψ . Therefore, equation (13) is linear only by form. In the low subsonic condition, the density variation is not too large. It is actually also close to linearity. The linear form recommended by [1] is indeed convenient. However, in high subsonic situations, the density variation is very large. When using equation (13) to perform iterations for Ψ , $\partial \rho / \partial x^i (i = 1, 2)$ remains unchanged. However, when $M \approx 1$, the variation of ρ with respect to Ψ is especially sensitive. Therefore, it is not favorable for the convergence of iterations between $\Psi - \rho$. If equation (8) is used, then the variation of $\partial \rho / \partial x^i (i = 1, 2)$ with Ψ is taken into account which is helpful for the convergence of ρ . The number of iterations n between $\Psi - \rho$ is reduced. The number of iterations v_n of the Ψ field itself could also be decreased.

In a loop duct example, $M_{\max} \approx 0.96$, the ratio of the time required for computation by using equations (8) and (13) $t_8/t_{13} \approx 0.4$. At this time, the $M > 0.7$ region occupies approximately 20%. The improvement in the 70-2 working condition was not obvious because most of the region in the flow field had very low M number. The $M > 0.7$ region merely occupied 5% although M_{\max} had already reached 0.96.

The new solution method using the non-linearization as the principal equation is similarly applicable to the inverse problem of S_1 stream surface and S_2 stream surface. Especially, the high subsonic region at that time would be larger. For the transsonic conditions, this new method should have special meaning.

The authors are very grateful for the guidance provided by Prof. Wu Chung-Hua.

APPENDIX DERIVATION OF EQUATION (8)

From equation (6) we can get

$$\frac{\partial \ln \rho}{\partial x^i} = \frac{J g_i}{a^2} \frac{\partial h}{\partial x^i} - \frac{\partial_i^*}{\partial x^i} \quad (i = 1, 2) \quad (\text{A.1}) \quad 42$$

where

$$h = c_p T = RT\kappa/(\kappa - 1)J, \quad a = \sqrt{\kappa g_c RT},$$

From equation (5), we get

$$\begin{aligned} g_c J h = g_c J I + \frac{\Omega^2 r^2}{2} - \frac{1}{2(f\rho)^2} \left\{ \frac{1 + d_1^2}{a_1^2} \left(\frac{\partial \psi}{\partial x^2} \right)^2 + \left(\frac{1}{a_1} \frac{\partial \psi}{\partial x^1} \right)^2 \right. \\ \left. - \frac{2}{a_1 a_2} \frac{\partial \psi}{\partial x^1} \frac{\partial \psi}{\partial x^2} \sin(\theta_1 - \theta_2) \right\} \end{aligned} \quad (\text{A.2})$$

From equation (A.2) and using (A.1), we can find

$$\begin{aligned} g_c J \frac{\partial h}{\partial x^i} = \frac{a^2}{f\rho(a^2 - (W)^2)} \left\{ \frac{W^2 + W^1 \sin(\theta_1 - \theta_2)}{a_1} \frac{\partial^2 \psi}{\partial x^1 \partial x^i} \right. \\ \left. - \frac{(1 + d_1^2)W^1 + W^2 \sin(\theta_1 - \theta_2)}{a_1} \frac{\partial^2 \psi}{\partial x^1 \partial x^2} \right\} + h_i \end{aligned} \quad (\text{A.3})$$

From (7.1), we get

$$\frac{\partial W^1}{\partial x^i} = \frac{1}{f\rho a_1} \frac{\partial^2 \psi}{\partial x^1 \partial x^i} - W^1 \left\{ \frac{\partial \ln(fa_2)}{\partial x^i} + \frac{g_c J}{a^2} \frac{\partial h}{\partial x^i} - \frac{\partial_i^*}{\partial x^i} \right\} \quad (\text{A.4})$$

Substituting equation (A.3) into (A.4), we get

$$\begin{aligned} \frac{\partial W^1}{\partial x^i} = \frac{\partial^2 \psi}{\partial x^1 \partial x^i} \left\{ 1 + \frac{W^1}{a^2 - (W)^2} [(1 + d_1^2)W^1 + W^2 \sin(\theta_1 - \theta_2)] \right\} \frac{1}{f\rho a_1} \\ + \frac{W^2 + W^1 \sin(\theta_1 - \theta_2)}{f\rho a_1} \frac{\partial^2 \psi}{(\partial x^1)^2} - W^1 \left\{ \frac{\partial \ln(fa_2)}{\partial x^i} + \frac{h_i}{a^2} - \frac{\partial_i}{\partial x^i} \right\} \end{aligned} \quad (\text{A.5})$$

Similarly, we can get the same kind of expressions for $\frac{\partial W^2}{\partial x^i}, \frac{\partial W^2}{\partial x^1}$. In which the expression of h_1 is

$$\begin{aligned} h_1 = \frac{a^2}{a^2 - (W)^2} \left\{ \frac{\partial}{\partial x^1} \left(g_c J I + \frac{\Omega^2 r^2}{2} \right) + (W)^2 \left(\frac{\partial \ln f}{\partial x^1} - \frac{\partial_1^*}{\partial x^1} \right) \right. \\ \left. - (W^1)^2 \frac{\partial a_1}{\partial x^1} - W^1 W^2 \frac{\partial \sin(\theta_1 - \theta_2)}{\partial x^1} + [(1 + d_1^2)(W^1)^2 \right. \\ \left. + W^1 W^2 \sin(\theta_1 - \theta_2)] \frac{\partial \ln a_2}{\partial x^1} + [(W^2)^2 + W^1 W^2 \sin(\theta_1 - \theta_2)] \frac{\partial \ln a_1}{\partial x^1} \right\} \end{aligned}$$

By substituting the expressions of $\delta w'/\delta x'$, $\delta w'/\delta x'$ into equation (3), we get the principal equation (8).

REFERENCES

- [1] Wu Chung-Hua: A General Theory of 3-Dimensional Flow in sub- and Supersonic Turbomachines of Axial, Radial and Mixed Flow Types, ASME paper no. 50-A-79, Trans. ASME Nov. 1952, NACATN 2604, 1952.
- [2] Wu Chung-Hua: The Thermoaerodynamic Basic Equations using Arbitrary non-Orthogonal Curvilinear Coordinates, 1963.
- [3] Wu Chung-Hua: Lecture notes on turbomachine 3-dimensional flow. 1975.
- [4] Wu Chung-Hua: 3-Dimensional Turbomachine Flow Equations Expressed with Respect to Non-Orthogonal Curvilinear Coordinates and Methods of Solution. 3rd International Symposium on Air Breathing Engines held in March 1976 at Munich.
- [5] Wu Chung-Hua: With regard to Simplified "Radial Equilibrium", "Axial Symmetric" flow motion, through flow computation, 3-dimensional theory of S_1 and S_2 relative stream surfaces and computer program. Technical Information Institute, Academia Sinica, 1974.
- [6] Robert S. Ruggeri and William A. Bensen. Performance of a Highly Loaded 2-stage Axial Flow Fan. NASA TMX-3076, 1974.

THEORY, METHOD AND APPLICATION OF THREE DIMENSIONAL FLOW DESIGN OF TRANSSONIC AXIAL FLOW COMPRESSOR*

Academia Sinica and Shenyang Aeroengine Company

ABSTRACT

On the basis of the 3-dimensional flow motion theory of Wu Chung-Hua, the thermoaerodynamic design of a single stage transsonic axial flow research purpose compressor has been accomplished. Through five cycles of iteration of the two stream surfaces, the center streamline on the S_1 surface of revolution basically coincided in shape with that of the corresponding streamline on the S_2 stream surface. The parameters on it such as V_{0r} , $\Delta s/R$ and stream surface thickness are approximately the same. A solution convergent to the three-dimensional flow field is obtained. In the meantime, the guidelines to judge that the design requirements are satisfied, the required flow passage needed for the flow rate and the blade airfoil are determined. The flow field analysis with respect to the supersonic gas inlet cross-section shows that due to the stagnation effect of the duct shockwave, quantities such as V_{0r} , $\Delta s/R$ all undergo sudden jumps.

I. INTRODUCTION

In the early 50's, reference [1] established the theory for the solution of subsonic and supersonic 3-dimensional flow motion of turbomachines using two types of relative stream surfaces. Now, it has become the theoretical basis for the turbomachine 3-dimensional flow design and the solution of the 3-dimensional flow field.

For an axial flow compressor, it is possible to neglect the rising curvature of the S_1 stream surface and to approximately assume it is a surface of revolution. The design problem can begin with the calculation of the inverse problem of the center S_2 stream surface (S_{2m}). After going through shape building and the direct problem calculation

of a family of S_1 surfaces of revolution procedures, a new cycle of S_{2m} computation is just beginning. In this process, based on certain judgment criteria determined by experiments or experience, corrections are made for parameters to make the aerodynamic plane more rational. Therefore, the entire iteration process is not only the solution process of the 3-dimensional flow but also the design process of the 3-dimensional flow.

In a transonic compressor, the airfoil of the supersonic gas entering cross-section and the calculation of the revolving surface flow field are closely connected.

This paper introduces the 3-dimensional flow design of a single stage transonic axial flow research compressor. The major design parameters are: flow rate 61 kg/sec, tangential velocity of the blade tip of the rotor 400 m/sec, wheel boss ratio 0.4, stage pressure ratio 1.5 and adiabatic efficiency 85%. Furthermore, it is required to have sufficient flutter margin and distortion-resistant capability. In order to improve the varying working condition characteristics, a varying curvature inlet guide blade is used.

II. COMPUTATION OF THE CENTER S_2 STREAM SURFACE AND THE DESIGN OF THE FLOW PASSAGE

1. Simplification of radial direction computation

Before computing S_{2m} , because the radial distributions of the flow passage and the work done are not determined, for simplification, the radial direction computation is carried out first. Seven factors such as the stage pressure ratio, the law of work performed, the inner and outer diameters of the rotor and the stator are selected. Three levels are chosen for each factor and an orthogonal design of flexible level is used according to the table heading $L_{27}(3^{13})$ to carry out 27 computations. The results are as follows:

* This paper has been presented in the 2nd National Engineering Thermal Physics Conference in Hangchow in November 1978.

(i) Under the condition of $U_t = 400$ m/sec, 1.5 pressure ratio and 85% efficiency can be reached. Therefore, they are chosen as the design parameters.

(ii) In the C type, equal work and S type work performing laws, the S type not only adds more work on the top to sufficiently utilize the work performing capability of the supersonic flow, but also greatly reduces the stress at the root which is advantageous to the deflection, diffusion factor and M number of the flow at that place. Consequently, it is favorable to the assurance of the efficiency of the root and the flutter margin and distortion-resistance of the stage. Therefore, we decided to adopt the S type work law (Figure 1).

(iii) The optimum value ranges of the inner and outer diameters of the flow passage are obtained to enable the computation of S_{2m} to be carried out in a more concentrated manner.

2. Characteristics of center S_2 stream surface computation

It completely abandons the axial symmetry assumption and it is also different from the principle of the average S_2 stream surface.

(1) Consideration of the effect of blade thickness. On the surface of revolution with P as the cascade distance, the flow rate can be expressed as

$$\begin{aligned} G &= \rho_0 W_{10} \tau_0^{(1)} P_0 \equiv \int_0^{(P-t)_k} \rho_k W_{1k} \tau_k^{(1)} dP_k \\ &\equiv \overline{\rho_k W_{1k} \tau_k^{(1)}} (P - t)_k \\ &\equiv (\rho_k W_{1k} \tau_k^{(1)})_m (P - t)_k / \zeta \end{aligned}$$

45

From this, the stream surface thickness used as the input of the S_{2m} computation is

$$\begin{aligned} \tau_{km}^{(2)} &\sim (2\pi r_0 \tau_0^{(1)} \rho_0 W_{10}) / (\tau_k^{(1)} \rho_k W_{1k})_m \\ &= (2\pi r_k / \zeta) / (P - t/P)_k \end{aligned}$$

where $\tau^{(1)}$ and $\tau^{(2)}$ are the stream surface thicknesses of the S_1 and S_2 stream surfaces, respectively. The subscripts 0, k and m are the

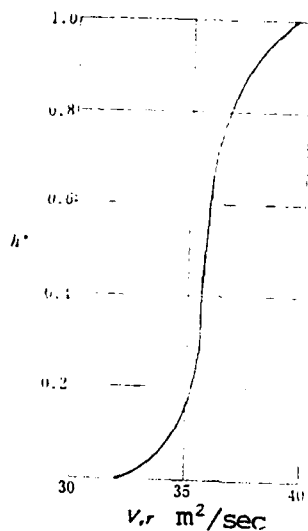


Figure 1. Distribution of $V_{\theta}r$ along the blade height

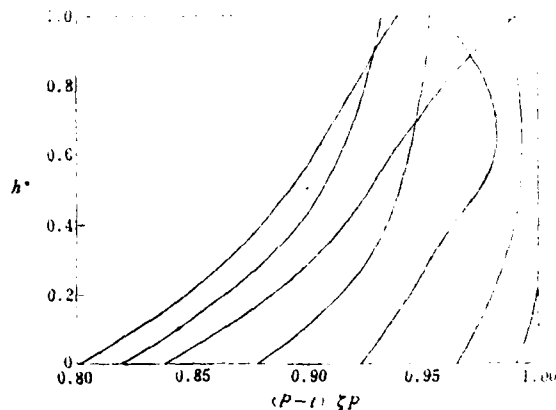


Figure 2. Distribution of $(P-t)/\zeta P$ along the radial direction

parameters in the gap, in the passage and on the center streamline, respectively. From the above equation, we can see that the physical meaning of ζ is the ratio of the density flow on the center streamline $(\rho W_1)_m$ and the average density flow on the surface of revolution $\overline{\rho W_1}$. It represents the effect of the tangential thickness of the blade on the center S_2 stream surface flow parameters (in the mean S_2 stream surface computation, $\zeta \equiv 1.0$).

In the S_{2m} computation, ζ directly takes the computational results from the S_1 surface of revolution. Finally, the radial distribution of $(P-t)/\zeta P$ is as shown in Figure 2. Figure 3 is the distribution regularity of the M number computed with various ζ values with respect to S_{2m} and the flow angle β . We can see the magnitude of the effect of ζ (in the figure the large ζ is the aforementioned calculated value, the small ζ is value obtained by using the blade front fringe radius as the tangential thickness at the front fringe).

(ii) The work law in the passage along the streamline

$$\xi_{V_{\theta}r} = [(V_{\theta}r)_k - (V_{\theta}r)_0] / [(V_{\theta}r)_7 - (V_{\theta}r)_0]$$

46

is based on the results on the center streamline obtained in the

(iii) The enthalpy increase law in the blade passage along the streamline is

$$\xi_k = (s_k - s_0)/(s_7 - s_0)$$

Because the projections of the blade gas entrance and exit boundaries on the meridian plane are curves, we adopted the computer program [6] compiled according to [3,4,5].

55

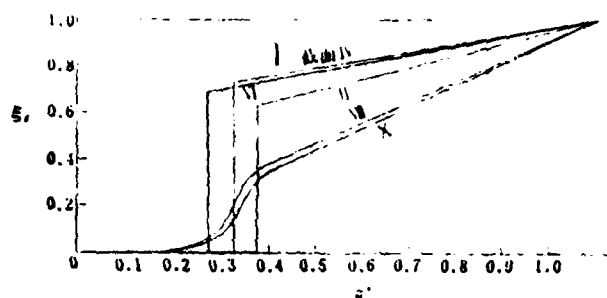


Figure 5. Variation of enthalpy along the flow passage
I--cross-section IV

The finally determined flow passage is as shown in Figure 6 (part of the streamlines and the computation stations are also plotted on it). It is obtained in the S_{2m} computation by adjusting the curvature of the flow passage. The purpose of the adjustment is to change the velocity distribution of the local regions in the root and at the top to improve the elemental characteristics of the heavily loaded rotor top and roots of the rotor and stator. 47

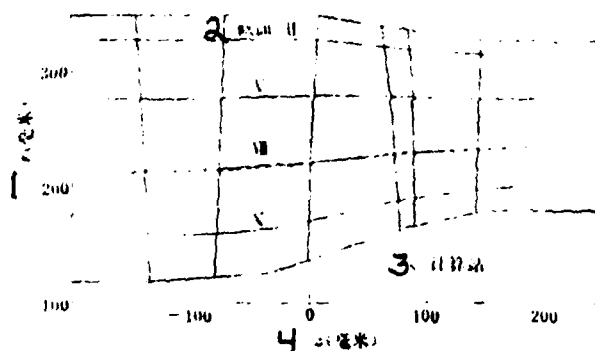


Figure 6. Flow passage pattern
1--(mm); 2--cross-section II; 3--computation station; 4--z(mm)

In the S_{2m} computation, we combined a series of experimental data and directly established the $\omega \cos \beta / 2\sigma - D$ curve based on various blade airfoils, cross-sectional positions and M numbers to select the absolute loss value for various positions. Because the numerical value of the D factor is not known beforehand, therefore, it requires iteration in the computation of the loss value. However, when the gas exciting angle turns beyond the axial direction, the value of the D factor can no longer reflect the load condition. This should be noticed in using the loss curve. The finally selected rotor efficiency

and stator total pressure restoration coefficient are given in Figure 7.

With regard to the flow rate coefficient, on the basis of analyzing large amounts of experimental data according to the condition of this research compressor, corresponding numerical values are chosen for the gap stations. In the blade array, linear interpolation is used. The flow rate coefficient values of the gap stations are shown in Table 1.

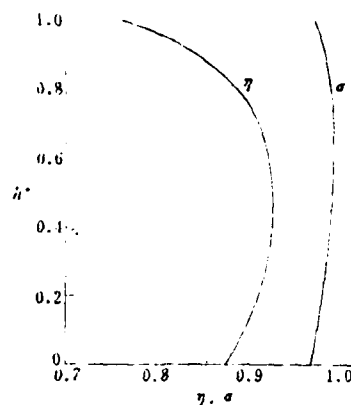


Figure 7. Radial distributions of rotor efficiency and stator total pressure restoration coefficient

4. Judgment guideline

In this design, the ranges of the following parameters are controlled:

rotor

$$D_r < 0.4 \quad \Delta\beta_h < 45^\circ$$

stator

$$M_{hi} < 0.75 \quad (V_{z1}/V_{s1}) \geq 0.85$$

$$D_h < 0.5 \quad \Delta\alpha_h \lesssim 45^\circ$$

$$(V_{s1}/V_{s1}) \geq 1.00 \quad (P_1/P_1) \geq 1.03$$

5. Calculated results

The convergent results of S_{2m} computation after five cycles of iteration are shown in Figures 8-11 and Table 2.

In order to facilitate the comparison to experiments, we also carried out S_{2m} computations of a single stage and single rotor with larger gaps. The calculated results indicate that the gas entrance and exit angles, the inlet M numbers and the diffusion factors of the three are comparatively close. Thus, as long as we carry out a design for a single stage without enlarging the gap, we should be able to obtain the blade and wheel which satisfy the three requirements of the experimental piece.

TABLE 1

far upstream	guiding vane inlet	rotor blade inlet	stator blade inlet	stator blade exit
1.000	1.010	1.015	1.025	1.028

47

1--far forward position; 2--inlet of the guide blade; 3--inlet of the dynamic blade; 4--outlet of the static blade;

TABLE 2

48

		inlet M	inlet angle	exit angle	axial speed ratio	static press. ratio	total press. ratio	total temp. ratio	diffusion factor
rotor	tip	1.340	-64.85	-58.22	0.8905	1.480	1.492	1.159	0.396
	mid-span	1.115	-56.49	-42.97	0.9060	1.498	1.545	1.144	0.432
	root	0.6826	-43.67	0.40	1.186	1.126	1.454	1.129	0.290
stator	tip	0.5798	35.13	0	1.043	1.034	0.9700	1.000	0.403
	mid-span	0.6529	36.75	0	1.067	1.071	0.9902	1.000	0.368
	root	0.8010	45.35	0	1.011	1.214	0.9670	1.000	0.485

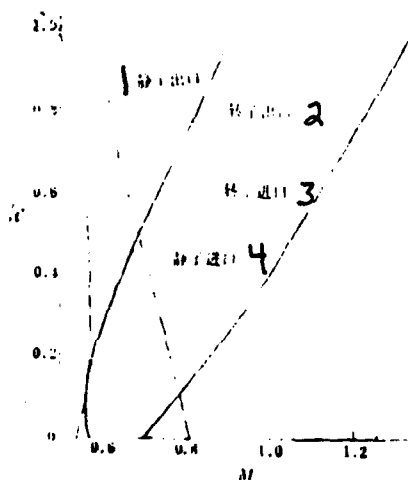


Figure 8. Radial distributions of the inlet and outlet M nos. 1--stator outlet; 2--rotor outlet; 3--rotor inlet; 4--stator inlet

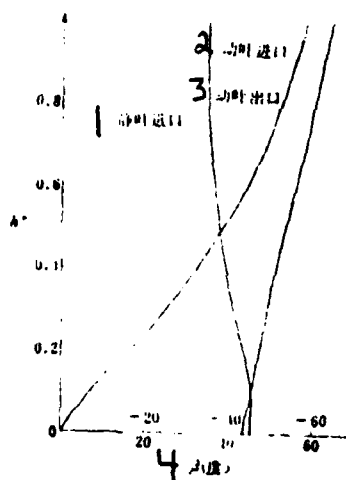


Figure 9. Radial distributions of the inlet/outlet β angle 1--static blade inlet; 2--dynamic blade inlet; 3--dynamic blade outlet; 4-- β (degree)

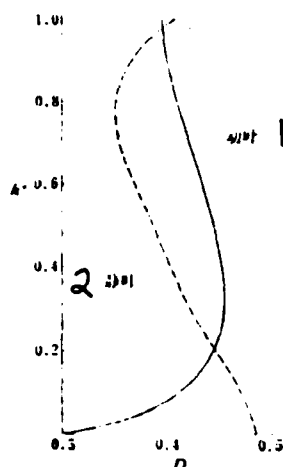


Figure 10. Radial distribution of diffusion factor
1--dynamic blade;
2--static blade

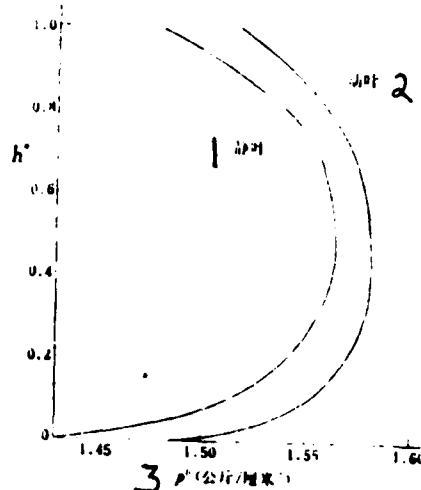


Figure 11. Total pressure distribution of dynamic blade outlet
1--static blade; 2--dynamic blade; 3-- p^0 (kg/cm^2)

III. COMPUTATION OF SUBSONIC SURFACES OF REVOLUTION

49

1. The computation of direct surface of revolution problem.

Different from S_{2m} , the computation of surface of resolution is carried out on a curved surface with pre-determined shape. Its main contents are:

(1) to calculate to obtain the $V_{\theta r}$, $\Delta S/R$ and $\tau^{(2)}$ on the middle streamline as the input data of S_{2m} computation to form the next cycle of computation.

(11) to compare the results of different airfoils and different attack angle shapes, to choose, adjust and correct the airfoil to minimize flow loss to the extent possible.

The selection and comparison of the airfoil are based on: the small pressure gradient of the rear part of the blade, the uniform velocity reduction of the flow passage and the low peak value of the

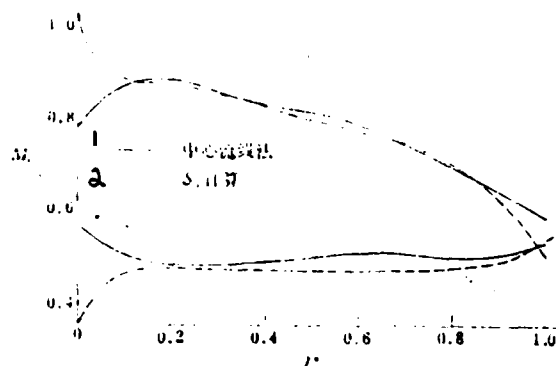


Figure 12. Results of surfaces of revolution computation
1--center streamline method; 2-- S_1 computation

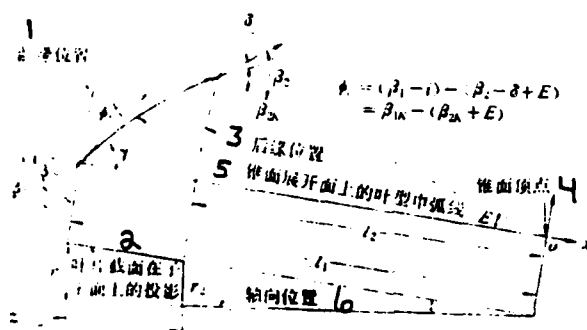


Figure 13. Diagrammatic example of the blade model parameters
1--position of the front fringe; 2--projection of the blade section on the meridian plane; 3--position of the rear fringe; 4--vertex of the conical surface; 5--middle arc line of the airfoil on the expansion surface of the conical surface; 6--axial direction position

M number in front of the suction surface. Thus, it is possible to reduce the blade surface boundary separation loss or to cause the cascade to deviate from critical over flow during the over rotating work condition without the occurrence of plugging. The computation of the surfaces of revolution adopts the computer program [7] compiled based on [3,4,5]. The typical calculated results are shown in Figure 12.

Through the computation of the surfaces of revolution, based on the parametric range in this design, with the exception that the top of the dynamic blade is a multi-arc model, the other sections are the double circular arc blade airfoil. The attack angle at the root of the dynamic blade is chosen to be 5° .

Because it is difficult to model on the surface of revolution, the geometric modeling is carried out on the expansion surface of the conical surface (Figure 13). On the expansion surface of the conical surface, the bending angle of the airfoil is

$$\varphi_E = \Delta\beta + \delta - i - E$$

where E is the angle between the two parent lines passing through the front and rear fringes on the expansion surface. The E angle of the positive cone is positive.

In order to be consistent with the S_{2m} computation, in this design the projection length of the airfoil on the meridian plane is fixed to be $b_l = L_2 - L_1$. For a certain attack angle and lag angle, the chord length b is determined by iteration. In the meantime, considering the methods to obtain the experimental cascade data, we use the M number and β angle of the gap station in the S_{2m} calculation as the basis for the model on the conical surface formed by the front and rear fringes. The lag angle computation formula used is:

$$\delta = \left(\frac{\Delta\beta - i}{\sqrt{\sigma/m_c}} + \Delta\delta \right) / \left(\frac{1 - m_c}{\sqrt{\sigma}} \right)$$

where

$$m_c = 0.92(u/c)^2 + 0.0002\beta_1, \quad \sigma = bN/\pi(R_1 + R_2)$$

(N is the number of blades), $\Delta\delta$ is the correction value of the lag angle which is chosen by experience (Figure 14).

The throat choking margin is an important judgment guideline of geometric modeling. If the throat flow has reached the critical stage, then it is possible to list the continuity equation from the inlet to the throat:

$$P_{01} q(\lambda_1) A_1 / \sqrt{T_{01}} = P_{0t}^* A_t^* / \sqrt{T_{0t}^*}$$

Because of the boundary layer and three-dimensional effects, the actual throat area A_t should be greater than A_t^* . In this design, the throat aerodynamic margin of the various sections of the rotor is

$$A_t / A_t^* \geq 1.03.$$

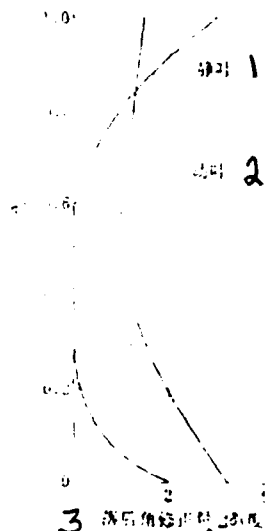


Figure 14. Variation of the correction amount of the lag angles $\Delta\delta$
 1--static blade; 2--dynamic blade; 3--correction of the lag angle (degree)

For stators, according to the results of cascade experiments, in order to obtain the minimum flow loss, the throat area margin A_1/A_t is about 1.03 within the M number range (0.6-0.8) in this design. The entire model design has been compiled into a computer program. The details are shown in [8].

3. The center streamline method aerodynamic model

For the subsonic flow on the surface of revolution, the various physical quantities $q(l, \varphi)$ of the flow field can be obtained from the value $q_0(l, \varphi_0)$ obtained from S_{2m} computation on the center streamline through a Taylor series expansion along the tangential direction. For a higher density airfoil, usually sufficient accuracy is reached by taking three terms:

$$q(l, \varphi) \approx q_0 + (\varphi - \varphi_0) \left(\frac{\partial q}{\partial \varphi} \right)_0 + \frac{(\varphi - \varphi_0)^2}{2!} \left(\frac{\partial^2 q}{\partial \varphi^2} \right)_0,$$

in which the first and second order derivatives are obtained from the continuity equation and the momentum equation. Then, from the flow rate relation, by taking the $\pm 50\%$ streamlines of the cascade flow rate, it is possible to obtain the upper and lower airfoil coordinates of the flow passage $l = l_{\pm}(r^*, \varphi^*)$. Simultaneously, it is possible to obtain the pressure distribution of the surface of the airfoil and the distribution of the number M.

The sectional airfoil of the rotor root obtained from computation using the computer program [9] compiled by this method is shown in Figure 15. In the figure, the surface of the geometric model is also plotted. The two are comparatively close. The distribution of the M number of the surface obtained using the center streamline method model is shown in Figure 12.

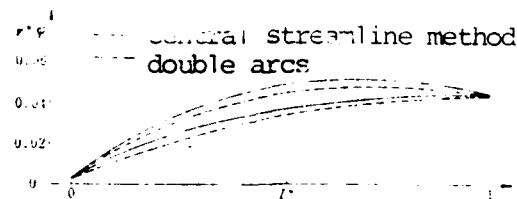


Figure 15. Comparison of center streamline method model to geometric model, the solid line is the center streamline method model, the dotted line is the double circular arc
1--center streamline method model; 2--double circular arc

It must be pointed out that whether the model surface obtained by the center streamline method model is rational or not depends on the given center streamline shape and the parameter distribution on it; the latter is obtained from S_{2m} computation. Therefore, although the center streamline method model does not explicitly include the attack angle and the lag angle, yet, because of its relation with S_{2m} computation, it must be correlated with certain characteristics such as the attack angle and lag angle. As a matter of fact, only after the convergence of stream surface iteration, can it then be compared to the corresponding geometrical model. Owing to this fact, the key to this method is S_{2m} computation. Once the two stream surfaces iteration computation converges to obtain the accurate S_{2m} data, it will be possible to get a smoothly surfaced, reasonably thick airfoil without any difficulty. This method can also be used to modify the airfoil.

IV. COMPUTATION OF SUPERSONIC SURFACES OF REVOLUTION

1. Multi-arc profile of sections at rotor tip

The inlet M number of the rotor from the root to the top varies from 0.68 to 1.34. Therefore, different airfoils are adopted. The sections with $M > 1.15$ use the multiple circular arc and the remaining sections use the double circular arc.

The multiple circular arc airfoil is plotted on the conical surface expansion surface. Because it is possible to adjust the bending

ratio of the front and rear segments, the position of the connecting point of the two circular arc segments and the maximum thickness position, it is possible to control the wave series in the flow passage to a certain extent to reduce shock wave losses.

In order to smoothly connect the multiple circular arc airfoil to the double circular arc airfoil, it is possible to properly choose the forward segment bending ratio and the forward segment chord length of the multiple circular arc airfoil near the connecting point of the two airfoils to make the two circular arc segments approach one circular arc.

For a cascade airfoil with supersonic gas inlet, it is necessary to satisfy the only gas entrance angle relation. Therefore, it is necessary to carry out iteration in the modeling process.

2. Computation at the inlet region

Both experimental results and theoretical analysis proved that there exists a stable periodic shock wave and expansion wave series in the head regions of a two-dimensional supersonic gas intake cascade. They have the function of adjusting the gas intake condition. Thus, corresponding to a certain gas intake M_0 , there exists the only gas intake angle β_0 . The correlation can be obtained through the solution of the basic equation established by the inlet flow field between the upstream and inlet regions.

The actual method is: to use the detached shock wave model [10] of a two-dimensional isolated wing. It is placed on the conical surface expansion surface as the shock wave ahead of the cascade. With regard to the supersonic flow field, the characteristic line equation in [11] and the correlation are used to find the solution. The computer program is shown in [12]. The computer program starts from the semi-infinite cascade of a blade with head and then propagates from upstream to downstream. After passing through 3-4 cascade distances, the M number of the corresponding position in the flow field is equal

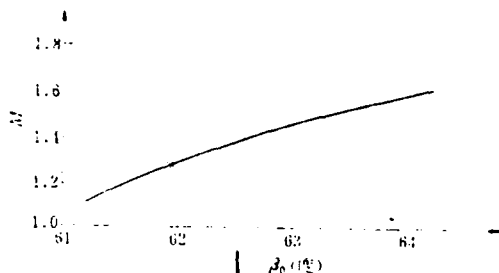


Figure 16. The only gas intake angle relation of supersonic gas intake cascade
1-- β_0 (degree)

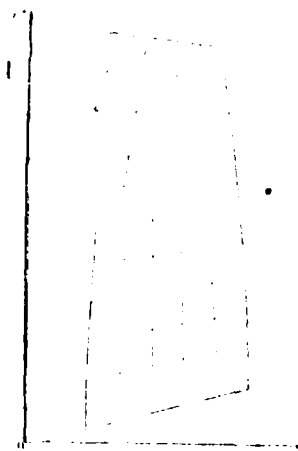


Figure 17. Shock wave track of the dynamic blade
1--shock wave track

to the value of β ; the periodic condition of the cascade is satisfied. Then, the invariance relation between the incoming flow and the inlet parameters is established for a control system whose tangential direction is one cascade distance in order to obtain the M_0 - β_0 relation of a uniform incoming flow. The typical result is shown in Figure 16.

When the M_0 number of the incoming flow is not too large and the taper of the outer wall of the machine box is not too high, and consequently, the variations of stream surface thickness and radius are not large, the supersonic inlet region can be approximately considered as single wave flow. Consequently, the Prandtl-Meyer equation is obtained. Its advantage is that the parametric relation between the inlet region and the upstream area can be directly established. It is only necessary to analyze one flow passage of an infinite cascade in order to obtain the upstream condition. Thus, the work load is greatly reduced.

Under these conditions, with the assistance of the neutral point and neutral wave concepts, from the continuity equation

$$\tau_0 \rho_0 W_0 \cos \beta_0 = \tau_e \rho_e W_e b \sin \mu_e$$

(where b is the width of the first passage swallowing a Mach wave in the cascade passage) and the P-M correlation

$$\beta_o = \beta_e + V(M_e) - V(M_o)$$

52

(where

$$V = \sqrt{(k+1)/(k-1)} \operatorname{tg}^{-1} \sqrt{(k-1)/(k+1)(M^2-1)} - \operatorname{tg}^{-1} \sqrt{M^2-1}$$

it is very easy to obtain the two unknowns M_o and β_o .

With regard to the effect of three-dimensional effect on the computation of the inlet region, typical computed data shows that when the stream surface thickness differs by 1%, the calculated attack angle deviates by 1° and the throat choking margin will be off by 1%.

3. Estimation of the $V_{\theta r}$, $\Delta s/R$ and ζ values on the center streamline

Due to the difficulty in accurately determining the position and shape of the shock wave in the passage, a model [13] with a certain accuracy as compared to the actual experimental data is used to estimate shock wave loss. Thus, it is approximately considered that: in front of passage shock wave, it is iso-enthalpic expansion. Through the shock wave enthalpy increment jump, the shock wave rear streamline airfoil loss increases linearly until the outlet (Figure 5). The corresponding meridian plane shock wave track line is shown in Figure 17.

From the calculated results of $V_{\theta r}$, we can see that on the supersonic gas intake cross-section, shock wave work occupies a great proportion. Along with the increases in the gas intake M number, this proportion also increases. Especially for the sections near the top, the work done is almost completely accomplished by shock wave. There is almost no increase in the passage behind the wave. Even acceleration would occur. In view of the important effect of the design of the sections near the top on the entire stage, it is necessary to carefully select the blade number, chord length, flow turning angle and other geometric parameters of the airfoil to ensure the design requirements.

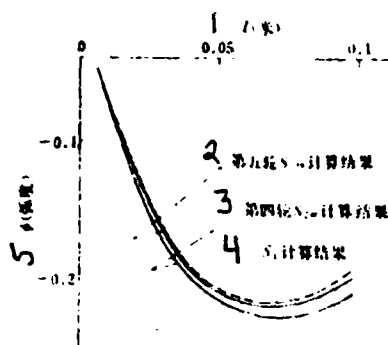


Figure 18. Center streamlines on the surface of revolution during iteration convergence and on S_{2m}

1--1(m); 2--5th cycle calculated result of S_{2m} ; 3--4th cycle calculated result of S_{2m} ; 4-- S_1 calculated result; 5-- ϕ (radian)

V. THE FINAL RESULTS OF STREAM SURFACE ITERATION AND CUMULATIVE ITERATION

After five cycles of iteration, convergent result is obtained. The major signs are that: The center streamline on the surface of revolution basically coincides with the corresponding streamline on S_{2m} in shape (Figure 18). The parameters, such as $V_{\theta}r$, $\Delta S/R$ and thickness distribution are approximately the same on them. At this time, the judgment criteria for each term have been met.

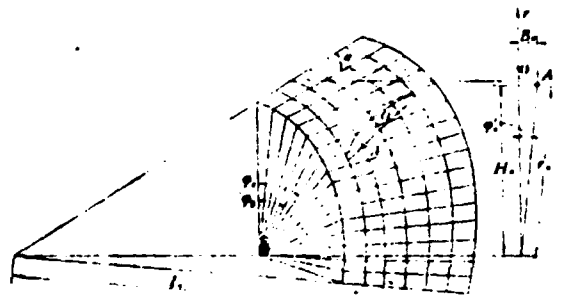


Figure 19. Schematic diagram of airfoil cumulative iteration

The airfoils of all the stream surfaces place their centers of gravity on the same radial line to carry out cumulative iteration [14]. In addition, the meridian projection of the chord length and the density value are adjusted to obtain the entire blade. The special feature of the cumulated iteration in this design is that the weight (represented by the thickness) of each stream surface is considered when the position of center of gravity is calculated. Consequently, the cumulative iteration method is consistent with the stream surface theory (Figure 19).

After airfoil cumulated iteration, we must also calculate elastic distortion of the blade and carry out correction for the blade coordinate.

VI. CONCLUSIONS

The two-stream surfaces theory was originally proposed for entirely subsonic or entirely supersonic flow motion. In recent years, it has been widely applied and verified. Now, we used it to design a transsonic compressor, i.e., through the iterative computation between a center S_2 stream surface and a family of S_1 surfaces of revolution to carry out the thermoaerodynamic computation as well as to select and modify the airfoil. It should be said that this was an attempt. We hope that through the repeated process of experiments and modifications later to continually perfect and develop the three-dimensional flow motion theory to gradually establish a more perfect three-dimensional flow design system of a transsonic turbomachine.

The supersonic inlet section, due to the presence of shock waves, makes the work done and enthalpy increase rapidly. Especially for the sections near the top, acceleration may occur even in the passage behind the shock wave. Therefore, to accurately control the wave series is an important problem in the design of a transsonic compressor.

The entire work was carried out under the guidance and participation of Prof. Wu Chung-Hua. Those who participated at various stages are: Xu Jian-zhong, Lu Wen-qian, Jiang Zuo-ren, Zhao Lian-xing, Wu Pang-xim, Tu Zhuan-She, Yang Jin-sheng, Bai Yin-ming, Zhang Yin and Lu Gen-shou of Academia Sinica; Zhou Wei-guo, Zhang Bao-xiang, Gao Yao-lin, Pau Yun-hu, Xu Bao-ming, He Shi-hui, Wu Ke, Zhang Zhi-fang and Yu Jin-shi of the Third Mechanical Department of Shenyang Aeroengine Company.

REFERENCES

- [1] Wu, Chunghua. A general theory of three-dimensional flow in subsonic and supersonic turbomachines of axial, radial and mixed-flow types, ASME paper no. 50-A-79; Trans. ASME Nov. 1952, or NACA TN 2504, 1952.
- [2] Wu, Chunghua and Wolfenstein, L. Application of radial-equilibrium condition to axial-flow compressor and turbine design, NACA Rep. 955, 1950.
- [3] Wu Chung-Hua: The Thermoaerodynamic Basic Equations of Turbomachines using Non-orthogonal Curvilinear Coordinates and Non-orthogonal Velocity Components, Research Note, 1963.
- [4] Wu Chung-Hua. Lecture note on three-dimensional flow of turbomachines, Chinese Technical University, 1975.
- [5] Wu, Chunghua. Three-dimensional turbomachine flow equations expressed with respect to non-orthogonal curvilinear coordinates and methods of solution, 3rd International Symposium on Air Breathing Engines held in Munich, March 1976,
- [6] Zhu Rong-guo: Computer program for S_2 stream surface line relaxation computation using arbitrary non-orthogonal curvilinear coordinates (manuscript), 1976
- [7] Wu Wen-qian and Liu Cui-e: Computer Program for computation method and matrix solution of S_1 stream surface using arbitrary non-orthogonal curvilinear coordinates (manuscript), 1976
- [8] Zhang Bao-xiang: Computer program for multiple circular arc modeling and double circular arc modeling on conical surface expansion surface (manuscript), 1978.
- [9] Liu Jilin, Lu Wengiang and He Shihuei. Computer program for central streamline on arbitrary surface of revolution, manuscript, 1978.
- [10] Moeckel, W. E. Approximate method for predicting form and location of detached shock waves ahead of plane or axially symmetric bodies, NACA TN 1921, 1949.
- [11] Wu Chunghua and Costdow, E. L. A method of solving the direct and inverse problem of supersonic flow along arbitrary stream filaments of revolution in turbomachines, NACA TN 2492, 1951.
- [12] Liu Cui-e and Wu Wen-qian. Determination of the only gas intake angle and computer program of flow field characteristic line algorithm of supersonic inlet of arbitrary surface of revolution cascades (manuscript), 1978.
- [13] Miller, G. R., et al. Shock losses in transonic compressor blade rows, ASME paper 60-WA-77.

EXPERIMENT OF TWO-DIMENSIONAL TRANSONIC TURBINE CASCADES*

Al Kiao-Yi**

(Beijing Heavy Electric Machinery Plant)

ABSTRACT

Based on the experimental results of three cascades, this paper analyzes the generation and development of the shock flow patterns in the transonic turbine cascade channel and their influence on the cascade aerodynamic performance. The important characteristics of the limiting regime, limiting loading and limiting inlet angle of the cascades are discussed. It is apparent that the transonic turbine cascade has the advantage of high loading capacity and high efficiency.

1. INTRODUCTION

Two-dimensional cascade experiments are an essential means to study the aerodynamic performance of transonic turbines. Wind tunnel tests have been conducted for the 850 mm rotor blades on our 10,000 kilowatt transonic turbine with three different blade profiles at various angles of attack. Figure 1 shows the three airfoil profiles used in the tests.

The experiments are conducted on the transonic cascade wind tunnel at the Ching-he Laboratory of our plant. The cross section of the test section is 400 x 100. The Mach number M_{2t} at the exit of the cascade can reach about 1.7. The duration for steady operation

* This paper was presented at the Second National Convention of Engineering Thermophysics, November 1978.

** Other contributors to this study: Zhang Ru-muo, Min Da-fu, Kong Qing-Xi and Yang De.

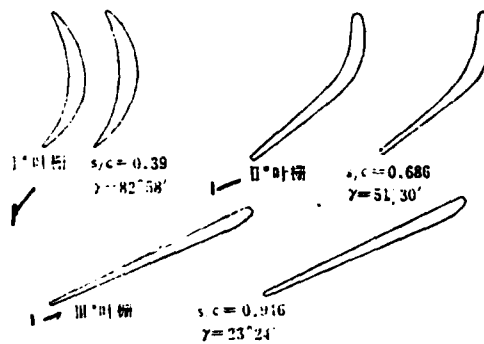


Figure 1. Airfoil profiles of the blades.

1--Cascade

is 50 - 100 seconds. The wind tunnel system satisfies the requirements of cascade testing after examination. The error of pressure measurements is 0.4% and the error in loss coefficient measurements is $\pm 0.3\%$. The exit angle is measured by self-alignment probes. Its error is $\pm 15'$. During the experiment, the total pressure and the static pressure both upstream and downstream of the cascade and the surface pressure along the blades are all recorded electronically. The wave spectrum in the cascade channel is also recorded by means of a 505-I shadowgraph camera with a 200 mm-diameter lens.

The condition of supersonic flow at the exit of the cascade must be considered when taking pressure data. The total pressure P_{03} measured by the probe is actually the total pressure behind the normal shock at the tip of the probe, while the static pressure P_2 on the side wall downstream of the cascade is the static pressure upstream of the shock. Hence, upon introducing the normal shock equations:

$$\frac{P_{03}}{P_2} = \left(\frac{K+1}{2} M_2^2 \right)^{\frac{K}{K-1}} \left(\frac{2K}{K+1} M_2^2 - \frac{K-1}{K+1} \right)^{-\frac{1}{K-1}}$$

and

$$\frac{P_{03}}{P_{02}} = \left(\frac{\frac{K+1}{2} M_2^2}{1 + \frac{K-1}{2} M_2^2} \right)^{\frac{K}{K-1}} \left(\frac{2K}{K+1} M_2^2 - \frac{K-1}{K+1} \right)^{-\frac{1}{K-1}}$$

the total pressure P_{02} downstream of the cascade without probe disturbance can be found readily. The resulting loss coefficient calculated eliminates the disturbance due to the probe.

All the experimental data are arranged in the following parameters:

Isentropic Mach number downstream of the cascade

$$M_{2i} = \sqrt{\frac{2}{K-1} \left[(P_{01}/P_{2CP})^{\frac{K-1}{K}} - 1 \right]}$$

Approaching Mach number upstream of the cascade

$$M_1 = \sqrt{\frac{2}{K-1} \left[(P_{01}/P_{1CP})^{\frac{K-1}{K}} - 1 \right]}$$

Mean loss coefficient

$$\zeta_{CP} = \frac{1}{S} \int_0^S \frac{(P_{01}/P_{02i})^{\frac{K-1}{K}} - 1}{(P_{01}/P_{2i})^{\frac{K-1}{K}} - 1} dS$$

Mean exit angle

$$\beta_{2CP} = \frac{1}{S} \int_0^S \beta_{2i} dS$$

Isentropic Mach number on the blade surface

$$M_{2i} = \sqrt{\frac{2}{K-1} \left[(P_{01}/P_i)^{\frac{K-1}{K}} - 1 \right]}$$

Loading coefficient

$$C_n = M_1^2 \cos \beta_1 + M_2^2 \cos \beta_2$$

Flow rate coefficient

$$\mu = M_1 \sin \beta_1 / \left[\left(\frac{2}{K+1} \right) \left(1 + \frac{K-1}{2} M_1^2 \right) \right]^{\frac{K+1}{K-1}} \sin \beta_{2i}$$

where $\beta_{2t} = \arcsin(t/S)$ is the effective exit angle of the cascade. This paper attempts to perform a preliminary analysis based on the experimental data.

2. GENERATION AND DEVELOPMENT OF SHOCK WAVE PATTERN IN THE CASCADE CHANNEL

Shadowgraphs of the II# cascade channel at the design inlet angle for different regimes are taken and are illustrated on the next page. Figure 2 shows the isentropic Mach number distribution along the blade surface of the cascade. For convenience, the wave system in the channel is reconstructed in Figure 3 according to the shadowgraph. 157

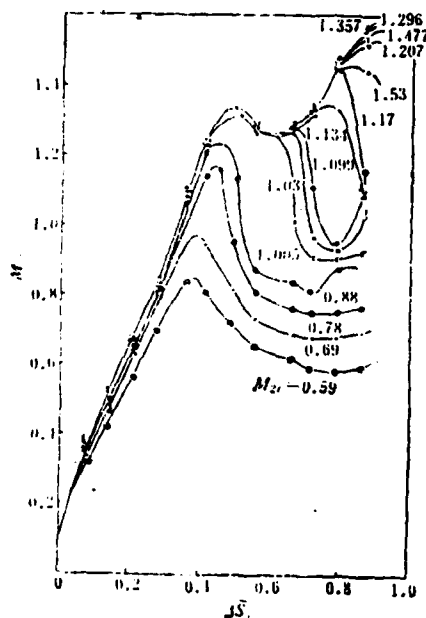


Figure 2. Mach number distribution along blade of II* cascade at design inlet angle.

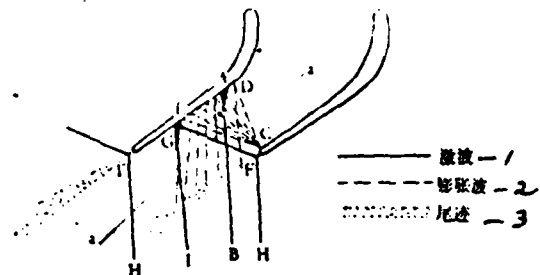


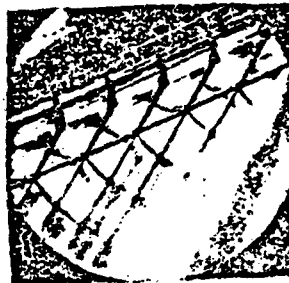
Figure 3. Wave pattern in channel.

1-- Shock wave; 2-- Expansion wave;
3-- Wake

From Figure 2, it can be noticed that, as the regime Mach number $M_{2t} > 0.7$, a local supersonic region appears on the portion of the blade surface where the curvature is the largest. A fan of



(a) $M_{\infty}=0.88$



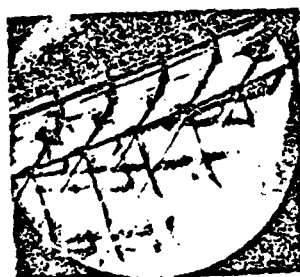
(b) $M_{\infty}=1.0$



(c) $M_{\infty}=1.1$



(d) $M_{\infty}=1.2$



(e) $M_{\infty}=1.35$



(f) $M_{\infty}=1.5$

Shadowgraphs of II[#] cascade channel at design inlet angle and different operating conditions.

relatively weak λ shock waves from the local supersonic region can be seen from shadowgraph a. They are represented by AB in Figure 3. The first peak value of the velocity distribution curve in Figure 2 gives the position of the generation of wave AB. As M_{2t} exceeds a certain value, the pressure at the exit of the cascade drops drastically due to the sudden circulating flow around the trailing edge of the blade. Thus supersonic region may also occur near the trailing edge, especially on the upper surface. The flows along the upper and the lower surfaces of the blade meet at a certain distance away from the trailing edge and the two fans of the compression waves reinforce into a pair of oblique shocks, that is, the left running wave FH and the right running wave FG (Figure 3). Together, they are called the sparrow tail waves of the blade.

As M_{2t} is increased, the local supersonic region enlarges accordingly. When $M_{2t} > 1$, the sonic line spans across the entire cascade channel, causing the flow to be choked. For such a condition, the right-running wave PG will meet wave AB (shadowgraph b). Since the flow behind wave AB is subsonic due to a sudden increase of pressure accompanied by a sudden drop in velocity across the wave (Figure 2), wave FG ceases to propagate after crossing wave AB. On the other hand, as the flow along the lower surface of the blade passes the trailing edge C, it experiences a sudden drop of pressure and accelerates around the edge rapidly. An expansion wave fan CDE centered at C is then generated between the sonic line and the tail wave, and reflected expansion waves are generated from the upper surface of the adjacent blade. A further increase of the flow regime would result in a corresponding increase of the strength and the range of the expansion wave fan. At the same time, the wave AB generated from the upper surface of the adjacent blade passes further downstream, and its strength is reduced under the interference of the expansion wave fan CDE. From shadowgraph c, the disturbed wave AB in the channel is not very clear due to the poor transmissivity of organic glass. But it is

still very sharp in the region downstream of the cascade. The velocity behind wave AB is increased correspondingly, such that the entire rear section of the cascade channel is supersonic (Figure 2). The right-running tail wave FG will now pierce the entire channel span to reach the upper surface of the adjacent blade. Under the influence of the boundary layer, a shock wave GI with complicated structure and large dimensions is reflected. The wake behind the cascade is a parallel flow of varying velocity. Hence when wave AB and the reflected wave GI come across the wave, they are deflected and partially reflected (shadowgraph c).

With the increase of M_{2t} , the intensities of all the wave systems increase and the Mach angles decrease correspondingly, causing the incident point G of the right-running tail wave on the upper blade surface to displace downstream (shadowgraphs c and d). The second peak value of the velocity distribution curve in Figure 2 indicates the location of the incident point G. It is apparent that it displaces downstream gradually as M_{2t} is increased. When $M_{2t} > 1.4$, the incident point reaches the exit trailing edge, and the reflected wave aligns with the left-running tail wave (shadowgraph e). A further increase of M would cause the right-running tail wave PG to depart from the cascade channel. Due to the non-uniform flow behind the cascade, it is deformed into a curve with its wave surface curving downstream (shadowgraph f). The mutual interference of the shock wave and the wake will become the decisive factor of the flow regime.

3. CRITICAL MACH NUMBER, CHOKING MACH NUMBER AND FLOW RATE COEFFICIENT

/ 59

The critical Mach number M_{2tKP} is the operating Mach number at which local supersonic regions appear in the cascade channel. Based on the tested data of the velocity distribution along the blade surface for various operating conditions, the relation between the maximum Mach number on the blade surface and the regime Mach number can be determined (Figure 4). The critical Mach number can then be obtained from such curves. It is found that for I* cascade: $M_{2tKP} = 0.76$, and for II* cascade: $M_{2tKP} = 0.69$.

When the cascade is operating in the transonic range and the sonic line spans across the entire channel, the flow rate will no longer increase with M_{2t} , that is, the channel is choked. The approaching Mach number upstream of the cascade also does not increase and is termed the choking Mach number M_{1max} . It depends on the geometric dimensions of the airfoils and the cascade, the inlet angle, and the viscosity of the working fluid. Figure 5 shows the variation of the approaching Mach number M_1 with the regime Mach number measured for the I* cascade. The choking Mach number can be read off directly. Figure 6 shows the measured variation of the choking Mach number versus different inlet angles for the III cascade. The dotted curve is the calculated curve based on one-dimensional isentropic theory, assuming that the sonic line passes through the geometric throat of the channel. The two curves are close to each other at low inlet angles.

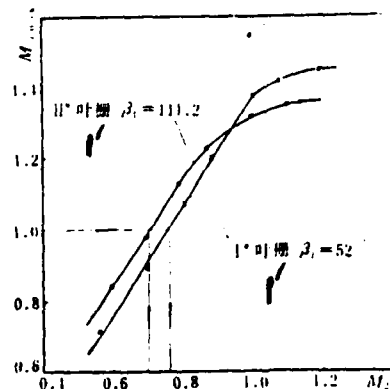


Figure 4. Relation between maximum Mach number M_{itmax} on the blade surface and the regime Mach number M_{2t} .

1-- Cascade

The flow rate coefficient μ is defined as the ratio of the actual choked flow rate to the theoretical design flow rate. In general, the theoretical flow rate is calculated by using the geometric throat area of the channel, while the actual flow rate depends on the aerodynamic throat area. In the experiment, it can be computed according to one-dimensional isentropic theory by employing the measured approaching Mach number and the inlet cross section. Figure 6 also shows the variation of the flow-rate coefficient with the inlet angle for the III* cascade. Although M_{lmax} increases correspondingly as β_1 increases, this does not mean that the throughflow capacity of the cascade would increase. It is because the throughflow capacity of the transonic cascade mainly depends on the actual dimensions of the aerodynamic throat. Either an extremely small or an extremely large inlet angle would make the flow characteristics of the cascade worse, causing the distribution and thickness of the boundary layer along the blade surface to change. Especially when separation of the boundary layer occurs, the size of the actual throat is greatly reduced. Hence for a certain flow rate coefficient μ , there exists an optimum range of inlet angle β_1 . For the III* cascade, μ always exceeds 0.99 for the range $141^\circ \leq \beta_1 \leq 149^\circ$.

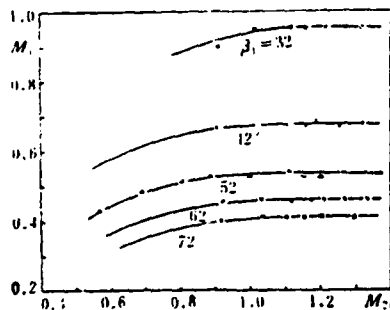


Figure 5. Variation of approaching Mach number versus Regime Mach number for I* Cascade.

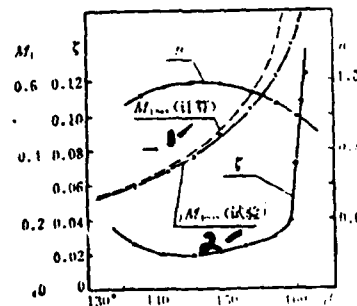


Figure 6. Variation of Loss Coefficient, Choking Mach number and flow rate coefficient versus inlet angle for III* Cascade.

1-- Calculated; 2-- Experiment

Figure 7 shows the experimental variation curve of energy loss coefficient ζ_{cp} versus operating Mach number M_{2t} of the three sets of cascades at the design inlet flow angle. Although the order of magnitude of the loss coefficients of the three different cascades are different from each other, the trends of variation are similar. These are typical loss characteristics of transonic turbine cascades. The following analysis of the relation between the variation of the loss coefficient and the development of wave systems are performed with the II* cascade as an example.

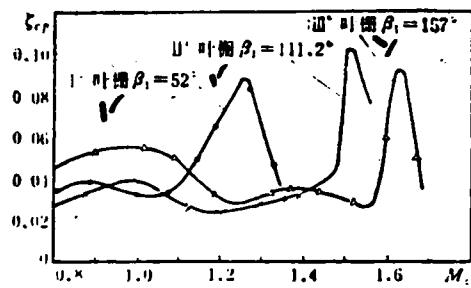


Figure 7. Experimental relation between energy loss coefficient and operating Mach number.

1-- Cascade

In the subcritical region ($M_{2t} < 0.69$), the loss coefficient due to friction and wake mixing is of the order 2%. After reaching the supercritical condition, local supersonic regions appear on the top of the blade, producing λ waves. The addition of shock wave loss gradually increases the total loss. When $M_{2t} = 1$, the choking condition is reached and the tail wave meets the λ waves from the blade top. The increase of shock wave loss causes the early separation of the boundary layer along the blade top, increasing the energy loss. The order of magnitude of the loss coefficient reaches 4%, which is about twice that for the subsonic operating

condition. When M_{2t} is further increased, a system of expansion waves occurs, weakening the waves on the blade top. At the same time, the incident point of the right-running tail wave on the blade top is displaced further downstream, causing the boundary layer separation region to move toward the exit and the energy loss to drop. For the range $M_{2t} = 1.07 - 1.35$, the measured loss coefficient of the cascade is 2.5 - 3%, which is slightly higher than that of the subsonic operation condition. This shows that the efficiency is not low at all. For $M_{2t} > 1.3$ and above, the incident point of the tail wave on the blade top still displaces downstream, but the loss increases slightly due to the increase of the shock strength. At about $M_{2t} = 1.45$, the tail wave propagates beyond the channel and hits the subsonic region of the wake of the adjacent blade. The signal of sudden pressure increase behind the wave would propagate upstream through the subsonic region of the wake, causing a pressure increase along with a velocity drop at the exit of the cascade and a thickness increase and separation of the boundary layer. At the same time, the left-running tail wave occurring there also displaces forward along the separation region of the boundary layer, causing the separation region to enlarge and mix with the wake and hence producing a great loss. From Figure 7, it can be seen that the loss coefficient at such operating conditions can jump to over 8%. As M_{2t} is further increased, the downstream displacement of the tail wave may reach the supersonic region of the wake. The signal of pressure increase behind the wave can no longer be propagated upstream. The degree of separation of the boundary layer near the trailing edge is lowered gradually and the flow condition is improved, causing the loss coefficient to drop gradually. The operating Mach number at which the loss coefficient starts to increase sharply is called the limit operating Mach number M'_{2t} . From experiments: for I* cascade $M'_{2t} = 1.1$, for II* cascade $M'_{2t} = 1.45$, for III* cascade $M'_{2t} = 1.55$. From the above analysis, it can be concluded that, if the operating condition of the cascade is kept under the limit operation Mach number, then the loss coefficient is by no means significantly large and relatively high efficiency is attained.

Factors influencing the loss coefficient of transonic turbine cascades are very complicated. The variation of the strength and the position of the wave systems, their reflections and mutual interferences, especially the interference between the shock wave and the boundary layer along the blade, and the mixing process of the wake behind the cascade, etc., all have a great effect on the characteristics of the energy loss. These factors make the calculation of loss extremely complicated and difficult. Hence nowadays people still rely on experiments to determine the loss coefficient and the limit operating Mach number M'_{2t} of transonic cascades and to define the optimum operating range.

Figure 8 shows the variation of the mean exit flow angle β_{2CP} with the operating Mach number for the three sets of cascades at design inlet flow angle. Their trend of variation is basically the same. In the subsonic range, the exit flow angle is basically constant. In the supercritical range, shock waves are generated in the channel. Refraction of the streamlines occurs when passing through shock waves, producing an obvious change of exit flow angle. Upon taking II* cascade as an example, it can be observed that when $M_{2t} > 1$, the exit flow angle drops slightly due to the effect of the right-running tail wave. But due to the interaction of the shock wave generated from the blade top, the reflected tail wave and the expansion wave fan, the exit flow angle increases with the increase of M_{2t} . At about $M_{2t} = 1.36$, the exit flow angle reaches the first peak value of about 35° . As M_{2t} is further increased, the incident point of the right-running wave on the blade top approaches the trailing edge, causing the boundary layer separation region to displace downstream. Hence, the flow remains closer to the blade once again and the exit flow angle drops slightly. Beyond the limit operating Mach number, the exit flow angle increases sharply due to the large separation region at the trailing edge. When $M_{2t} = 1.53$, the angle β_{2CP} can be as high as 44° , reaching a second peak value.

/61

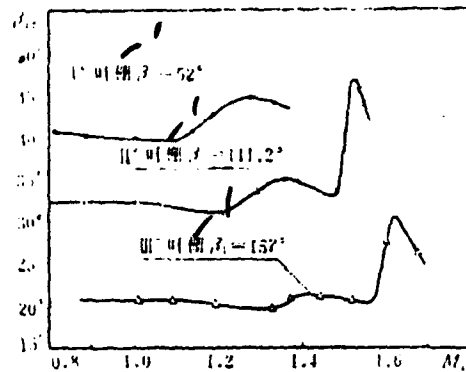


Figure 8. Tested curve of the relation between mean exit flow angle β_{2cp} and operating Mach number M_{2t} .

1-- Cascade

5. OPERATING CAPABILITY AND LIMIT LOAD

Operating capability is an important gasdynamic characteristic of the cascade. It is expressed by the loading coefficient

$$C_n = M_1^* \cos \beta_1 + M_2^* \cos \beta_2$$

For transonic cascades operating at supercritical pressure ratio, the choking condition is reached and the upstream Mach number M_1 is kept constant. Hence when the inlet flow angle β_1 is constant, the operating capability of the cascade can only be expressed by $M_2^* \cos \beta_2$, which is the tangential exit Mach number.

When the cascade is operating in the subsonic range, the expansion process of the flow is completed mainly in the mainstream passage upstream of the throat of the cascade channel. After the flow passes the throat, a portion of the expansion is eliminated due to a pressure increase and velocity decrease along the blade top. With the increase of the operating Mach number and when the supercritical pressure ratio is reached, the cascade is operating at

transonic speed and the flow at the throat is sonic. The supersonic flow in the divergent section continues to accelerate and expand, thus improving the operating capability of the cascade. In Figure 9, the variation curves of C_u with M_{2t} from experiments are shown for the three sets of cascades. It can be observed that, when $M_{2t} > 1$, C_u continues to increase, verifying that transonic cascades have higher operating capability. However, it does not increase indefinitely with M_{2t} . For each set of cascades, there exists a maximum value for C_u , which is termed "the limit load". The operating Mach number corresponding to the limit load is called the limit load Mach number. It is clear from the analysis of the wave systems that the supersonic expansion process in the divergent section relies mainly upon the expansion fan CDE (Figure 3) and their reflected expansion waves. With the increase of Mach number, the strength and the Mach angle of the expansion wave fan also increase. Their incident points on the blade top are thus displaced downstream, enlarging the expansion ratio and hence the operating capability of the cascade. But when the last expansion wave CE hits the trailing edge of the blade, the expansion in the divergent section ends. From Figure 2, it is clear that velocity increases along the blade top until the trailing edge at the exit is reached, making full use of the expansion function of the divergent section. As the operating Mach number is further increased, the flow behind the cascade expands with constant tangential velocity due to the enlarged exit flow angle. At this point, the operating capability not only ceases to increase, it may in fact decrease slightly due to the separation of the boundary layer at the trailing edge. Hence the problem of maximum operating capability of transonic cascade; that is, the limit load problem, does exist.

The analysis and study of the physical process of the formation / 62
of limit loads in transonic cascades and the determination of the
magnitude of the limit load and the corresponding limit load Mach

number is very important. A comparison between Figure 7 and Figure 9 shows that the limit load Mach number of the cascade and the limit operating Mach number at which loss starts to increase sharply are very close to each other. This may be due to the fact that for common cascades, especially those with blades of a very thin exit edge, the last expansion wave is very close to the right-running tail wave, and they hit the trailing edge of the blade at almost the same operating conditions. This result enables us to make good use of the advantages of transonic cascades, namely, large operating capability while performing with acceptable efficiency. Currently approximate methods for the calculation of limit load of cascades already exist. But wind tunnel tests are still very practical in the determination of limit loads of transonic cascades.

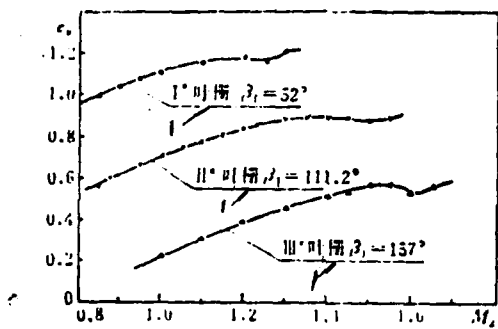


Figure 9. Tested curve of relation between cascade load coefficient C_u and operating Mach number M_{2t} .

1-- Cascade

6. LIMIT INLET FLOW ANGLE

Figure 10 shows the $\zeta_{cp} = f(M_{2t})$ curves of the III* cascade at different inlet flow angles obtained experimentally. It is observed that the effect of the inlet flow angle becomes more explicit only after $M_{2t} > 1.4$. For $\beta_1 > 149^\circ$, the minimum value of loss rises slightly, but the corresponding optimum operating Mach number increases significantly. At the same time, the limit operating Mach number also increases with the inlet flow angle. This implies that the practical operating range of the

cascade is extended. This may be due to the extension of the supersonic expansion region when the sonic line moves upstream from the throat at higher inlet flow angle. But there exists a certain limitation to the inlet flow angle increase of cascades with $\beta_1 > 90^\circ$ and the inlet flow angle decrease of cascades with $\beta_1 < 90^\circ$. Analysis of the III* cascade ($\beta_1 > 90^\circ$) shows that when β_1 increases to a certain value, such that the width of the approaching stream is less than the throat width of the channel, then the sonic line at which subsonic flow transits into supersonic flow would displace forward up to the guiding stream in front of the cascade channel. Thus, the cascade inlet flow is already supersonic. Two oblique shocks are generated from the leading edge of the blade. As illustrated in Figure 11, the right-running shock wave destroys the uniform flow field at the inlet region of the cascade, while the left-running shock wave propagates across the channel and produces a reflection wave after hitting the concave surface of the blade. The cascade channel becomes entirely supersonic and more complicated wave systems appear. Their superposition and their interference with the boundary layer along the blade cause the energy loss of the cascade to increase sharply. Figure 12 shows the variation of M along the cascade pitch of the III* cascade operating at $M_{2t} = 1.5$ and various inlet flow angles. When $\beta_1 = 161^\circ$, the M_1 distribution becomes non-uniform, and when $\beta_1 = 162^\circ$, M_1 exceeds 1 at a certain section of the cascade pitch and supersonic region appears. At $\beta_1 = 162.6^\circ$, a sudden jump of M_1 distribution occurs, under the interference of the leading edge shock wave. It is certain that energy loss is very large at this stage. The experimental curve in Figure 6 verifies this judgment: For $\beta_1 > 159^\circ$, the loss starts to increase sharply, and when $\beta_1 = 161^\circ$ is reached, its value has already exceeded 10%.

To restrict the inlet flow angle, the inlet flow angle at which the sonic line occurs just in front of the channel, such that the approaching flow is supersonic, is defined as the limit inlet flow

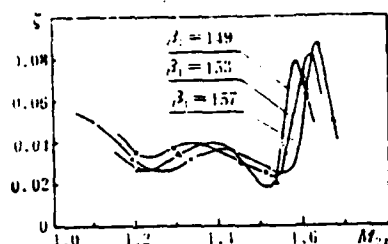


Figure 10. Experimental variation of loss coefficient of III* Cascade at various inlet flow angles.

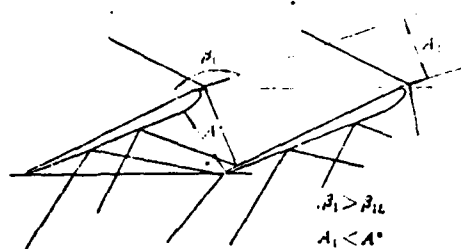


Figure 11. Waves in the Cascade when the inlet flow angle exceeds the limit.

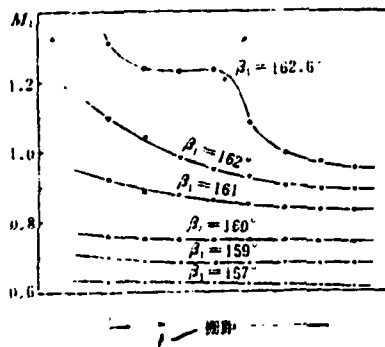


Figure 12. Distribution of approaching Mach number M_1 of III* Cascade.

1-- Cascade pitch

angle. If the width of the guiding stream at such a condition is assumed to be equal to the geometric throat of the channel, then the limit inlet flow angle of the III cascade can be calculated to be $\beta_{1L} = 159^\circ 10'$. Actually, due to the two-dimensional and viscous effects of the flow, β_{1L} is slightly larger than the computed value. Using the same method, the limit inlet flow angle of the I* cascade is also calculated to be $\beta_{1L} = 38^\circ$, which is close to the measured value.

The author would like to express his gratitude to Mr. Zhang Guong-hua, Mr. Ling Zhi-guog, Mr. YehDa-jun and Mr. Quiang Kuo-fang for their valuable advice.

REFERENCES

- [1] M.E. Jie Yi-gi, "Engineering Gasdynamics", Electric Industry Publication, 1956.
- [2] J.B. Meyer, "Theoretical and Experimental Investigations of Flow Downstream of Two-Dimensional Transonic Turbine Cascades", ASME paper 72-GT-43.
- [3] I. Fruchtman, "The Limit Load of Transonic Turbine Blading", ASME paper 74-GT-80.
- [4] Troyanovskiy, B.M., Mayorskiy, Ye.V., Garagulya, B.A., "Supersonic Lattices of the Last Stages of Powerful Steam Turbines," Teploenergetika, 1977, 10.
- [5] Jin Teng-ho, Shuoitien Guong-hong, Shangji Ji-Hong, "Experimental of Two-Dimensional Transonic Turbine Cascades", Report of Japanese Aerospace Technology, TR-84, 1965, 3.

Gao Yao-lin, Cai Yun-jin, Wang Hui-lin and Zhong Yu-ling
(Shenyang Aeroengine Company)

ABSTRACT

This paper is a summary of progress made in experiments on inlet flow distortions of the low pressure compressor of the B₁ engine.

In the experiment, the equal rotational speed characteristic lines and the surge lines of compressors with blades of two different aspect ratios were recorded under different inlet flow distortions. Furthermore, the critical sector angle of distortion resistance and attenuation rate of flow distortion for each case were determined. In the paper, the experimental results were analyzed. The experimental results indicate that the response characteristics of inlet flow distortions for compressors with blades of different aspect ratios were not the same. Compared to a large aspect ratio, compressor blades of smaller aspect ratios have better distortion resistant capability and larger surge margin. This improved the operating characteristics of the engine which was more suitable for flight maneuverability of airplanes.

I. EXPERIMENTAL OBJECT AND DISTORTION APPARATUS

The experiments were carried out with a modified experimental J211-950 unit. The modification consists of removing the fourth stage and to restoring the flow regulating blades in the third stage to the original position. Then, the corresponding measurement section and the disturbance device are installed.

*This paper was read at the Second Engineering Thermal Physics Conference in Hangzhou in November 1978.

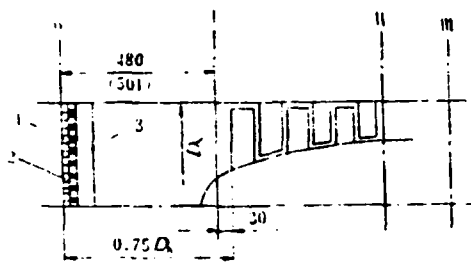


Figure 1
1--disturbance net; 2--
support net; 3--support
frame

The steady state inlet radial pressure flow distortion of the compressors used in this experiment was realized by relying on a disturbance device upstream. The simple structures of this device were most commonly holes in a plate and disturbance net types. In this experiment, the disturbance net structure was adopted. Figure 1 is a schematic diagram of the experimental unit and the disturbance device. The disturbance net was installed at $0.75 D_k$ in the upstream. The support frame was composed of 12 radial bars. A support net woven of 1 mm metal wires with 20x20 eyelets was placed on the support frame. Finally, the required disturbance net was secured at the support net and the frame. Thus, the distortion apparatus of this experiment was created.

The quasi-uniform flow in the paper referred to the flow field of the inlet flow after passing through the support frame and support net. Various flow distortions were accomplished by the sector shaped disturbance net of different blockage ratios. Simultaneously, in order to find the critical disturbance angle (sector angle) of the compressor, various sector shaped disturbance nets were prepared before hand. The passage way blockage ratios (%) for various kinds of sector shaped disturbance nets were 20, 25, 30, 35, 40, 64 and 69.

The B_1 engine low pressure compressor is a three stage transonic axial flow compressor. The only difference in the two experimental compressors mentioned in this paper is that the aspect ratios $\frac{h}{b}$ of the first stage working blades were not the same. One of them has $\frac{h}{b} \approx 2.0$ and the other one has $\frac{h}{b} \approx 2.6$. For convenience, they are called Compressor I and Compressor II for short from here on.

In order to satisfy the required flow distortions, in the experiment we frequently overlapped various sector disturbance nets on the support frame and net. Actual results proved that the effect was good. Using only a few disturbance nets, we could obtain a lot of distortions. In addition, in this experiment, we also used structural measures for adjusting the axial distance from the disturbance net to the compressor inlet in order to obtain more distortions.

II. PARAMETRIC MEASUREMENT AND DATA PROCESSING

The parametric measurement cross-section I-I of the compressor inlet was located 30 mm in front of the front fringe of the root of the first stage blades. The disturbance net was installed at the 0-0 cross-section which was 480 mm from the I-I cross-section (see Figure 1).

The inlet flow distortion experiments had placed greater requirements on the testing methods. Not only the flow parameters must be accurately measured at the measuring point, but also the distributions of the measured flow parameters across the entire measuring cross-section must be determined because they could directly influence the accuracy of the experimental results.

In the experiment, several fixed pressure transducer probes were installed on the I-I cross-section to facilitate the determination of the total pressure distribution of the compressor inlet cross-section. The pressure probes were of two types: one was the ten point synthesized probes which were placed radially along the total static pressure measuring point 18 mm apart; the other was the 6p pressure probes distributed radially along the measuring points 20 mm apart.

From Figure 7, we can see that in order to accurately calculate the average total pressure value p_{1cp}^* at the I-I cross-section of the inlet, it was necessary to go through the lengthy circumferential and radial averaging process. For convenience, we selected the average value of the pressures measured by a synthesized probe and a 6p

probe behind the net as the low pressure value of the inlet cross-section disturbance region and chose the average value of total pressure measured by the synthesized probed inserted in areas not affected by the disturbance as the high pressure value of the inlet I-I cross-section. Then, the average value of the total pressure of the flow at the inlet could be obtained according to the following formula:

$$p_{i,r}^* = \frac{p_{i,min}^* \cdot \theta^\circ + p_{i,max}^* (360^\circ - \theta^\circ)}{360^\circ}$$

where θ° --disturbance sector angle

$p_{i,min}^*$ --inlet flow average total pressure in the disturbance net region

$p_{i,max}^*$ --inlet flow average total pressure in the area without disturbance

In the III-IV cross-section located far away from the outlet of the compressor, a total pressure target with nine measuring points along the blade spacing was installed. It could move along the direction of blade height. The total flow pressure was measured at 5 radial positions and their average value was taken as the total pressure of the compressor outlet. The measuring plane of the compressor outlet flow distortions was II-II which was close to the outlet of the third stage flow regulating blades. Several pressure and temperature probes were installed in that plane.

In order to evaluate the magnitude of the inlet flow distortion, the following two distortion indicators were used

$$DC_\theta = \frac{p_{i,r}^* - p_{i,min}^*}{\frac{1}{2} \rho V^2} \quad (1)$$

$$\bar{D} = \frac{1}{p_{i,r}^*} (p_{i,max}^* - p_{i,min}^*) \quad (2)$$

where $\frac{1}{2} \rho V^2 = (p_i^* - p_i)_{max} - \frac{\theta^\circ}{360^\circ} [(p_i^* - p_i)_{max} - (p_i^* - p_i)_{min}]$; $(p_i^* - p_i)_{max}$

and $(p_i^* - p_i)_{min}$ were related to the flow velocities of the disturbance free flow and disturbance flow, respectively.

AD-A131 031 FLOW-FIELD MATRIX SOLUTION FOR DIRECT PROBLEM OF FLOW
ALONG S1 RELATIVE S..(U) FOREIGN TECHNOLOGY DIV
WRIGHT-PATTERSON AFB OH W WENQUAU ET AL. 18 JUL 83

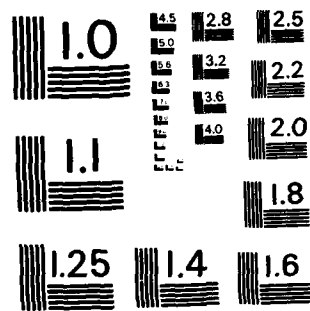
2/2

FTD-ID(RS)T-1010-82

F/G 20/4

NC

END
DATE
FILMED
6 83
DTIC



MICROCOPY RESOLUTION TEST CHART
NATIONAL BUREAU OF STANDARDS-1963-A

The two indicators above are both distortion indicators based on the calculation of the total pressure loss. Their magnitudes demonstrated the degrees of flow distortions. In this experiment, the experimental ranges of DC_0 and \bar{D} were 24-55% and 8-18% respectively.

/66

III. EXPERIMENTAL RESULTS AND DISCUSSION

We recorded the characteristic lines and surge lines of the quasi-uniform flow of Compressor I and Compressor II under rotational speeds at $\bar{n} = 1.0, 0.98, 0.95, 0.90, 0.85$ and 0.80 as the base line in comparison with the performance of the compressor under flow distortion. In addition, in order to evaluate the distortion-resistant capability of Compressor I and Compressor II, we used a fixed working line, obtained by calculation, to estimate the variations of the surge margin of the above two compressors under various inlet flow distortions. It should be pointed out that up until the present moment there has not been a standard for the definition of surge margin. There are various definitions. Some of them used the working point on the equal rotating speed line and the converted flow at the surge point to carry out an overall comparison with the pressure ratio parameter, some only used the pressure ratio parameter for comparison; some used the pressure ratio parameter at the working point under constant flow and at the surge point for comparison, etc. We, based on the actual situation, adopted the following definition of surge margin to calculate the surge margin of the compressor.

$$\text{Surge margin (\%)} = \left[\frac{(G_{\text{surge}}/\pi_k^2)_{\text{exp}}}{(G_{\text{surge}}/\pi_k^2)_{\text{cal}}} - 1 \right] \times 100\%$$

where G_{surge} and π_k^2 were the converted flow and pressure ratio of the compressor, respectively.

(I) Critical sector angle, θ_{critical}

The critical sector angle is one of the indicators of the distortion-resistant capability of the compressor. If θ_{critical} is large, this indicates that the response of the compressor to the inlet

flow distortion is not sensitive. It can stand a larger area of disturbance of the inlet flow. In this experiment, two pieces of sector disturbance nets (overlapping each other) with passage blockage ratios at 25% and 30%, respectively, were used to determine the critical sector angle of the compressor. The sector angles of these nets were 45°, 60°, 75°, 90° and 120°. Figures 2 and 3 are curves obtained experimentally.

From Figure 2 we found that the critical sector angle θ_{critical} of Compressor I was between 75° and 90°. In the region less than θ_{critical} , when θ was increased, the ratio π_k^* distorted,surge / π_k^* quasi,surge of the compressor dropped rapidly almost in a linear fashion. After reaching θ_{critical} , if θ was increased further, that ratio maintained a constant value. Figure 3 is the corresponding experimental curve for Compressor II whose critical sector angle was 60°. It was smaller than the critical sector angle of Compressor I.

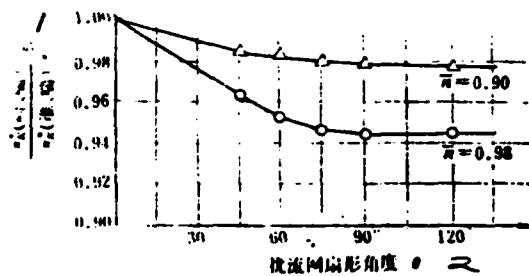


Figure 2. Experimental curve of the critical disturbance angle of Compressor I.
1-- π_k^* (distortion,surge) / π_k^* (quasi,surge)%
2--disturbance sector angle θ

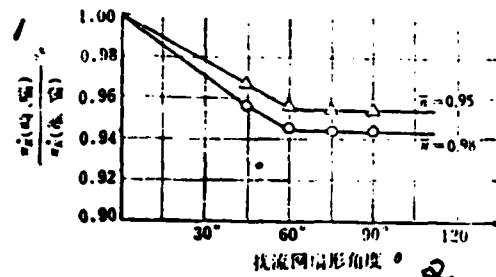


Figure 3. Experimental curve of the critical disturbance angle of Compressor II.
1-- π_k^* (distortion,surge) / π_k^* (quasi,surge)%
2--disturbance sector angle θ

TABLE 1. Critical sector angles of several compressors under distortion

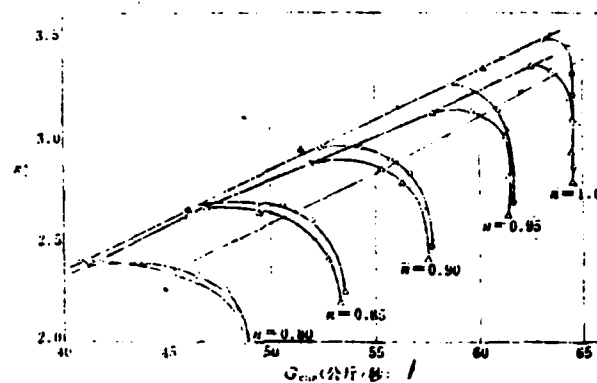
	轴流压气机 1	J85-GH-13	A 机高压 2	压气机 I 3	压气机 II 4
$\theta_{\text{critical}}^5$	60°	60°	40°	75°—90°	60°

1--spade; 2--high pressure A engine; 3--Compressor I; 4--Compressor II;
5-- θ_{critical}

Table 1 presents the distortion critical sector angles of several types of compressors. The first three, due to the difference in experimental conditions, will not be compared. The latter two had exactly the same experimental conditions. The only difference was that the aspect ratios of the first stage rotor blades were not the same. From the comparison of $\theta_{critical}$, it showed that Compressor I was not sensitive to the inlet flow distortion which was in agreement with the conclusion in [4]. This was also consistent with the fact that Compressor I had a larger surge margin under flow distortion which will be discussed later.

(II) The effect of inlet flow distortion on compressor characteristics and surge lines

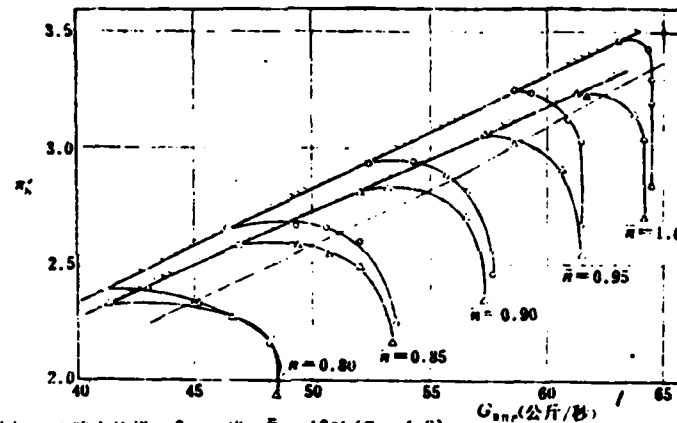
From the experimental results, we found that at higher rotational speeds ($\bar{n} \geq 0.90$) the characteristic lines were most steep while under quasi-homogeneous flow and most flat while under flow distortion. Along with increasing inlet flow distortion \bar{D} , this trend became more obvious (refer to Figures 4-6). Therefore, based on the experimental results, there is such a regularity in existence. This indicated that the distortion of inlet flow would cause the compressor performance to decrease and that the characteristic lines were greatly varied. For rotational speeds $\bar{n} = 1.0$ and 0.98 , the flow region contained was increased. The medium rotational speed lines did not vary significantly in shape, however, their positions were shifting toward the direction of lower performance but it was not as obvious as in the high speed case. This is most probably because the corresponding distortions under these rotational speed lines were small. It should be pointed out that in Figures 4-6 presented in this paper, for the various characteristic lines in the same figure, their corresponding inlet flow distortion values were not identical. With decreasing rotational speed, the corresponding inlet flow distortion was also decreased. Our experimental method could not guarantee to keep the inlet flow distortion under various rotational speeds to be constant. In fact, it was not necessary because that would further deviate away from the actual working conditions.



2 压气机 I ○ 准均匀流场 △ 畸变流场: $\theta = 90^\circ$ $\bar{D} = 8\%$ ($\bar{n} = 1.0$) ▲ 压气机 II 准均匀流场端点

Figure 4

1-- G_{sur} (kg/sec); 2--Compressor I, 0 quasi-homogeneous flow, Δ distorted flow: $\theta = 90^\circ$ $\bar{D} = 8\%$ ($\bar{n} = 1.0$) ▲ surge point of quasi-homogeneous flow of Compressor II.



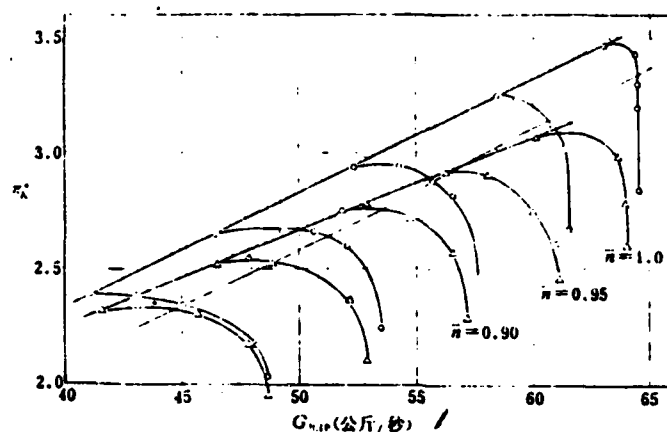
2 压气机 I ○ 准均匀流场 △ 畸变流场: $\theta = 90^\circ$ $\bar{D} = 12\%$ ($\bar{n} = 1.0$)

Figure 5

1-- G_{sur} (kg/sec); 2--Compressor I, 0 quasi-homogeneous flow, Δ distorted flow: $\theta = 90^\circ$ $\bar{D} = 12\%$ ($\bar{n} = 1.0$)

Figure 4 showed that in a quasi-homogeneous flow, the shapes and positions of the surge lines for Compressors I and II were basically the same. This indicated that the effect of increasing blade chord length to reduce the aspect ratio on the surge lines of the compressor under homogeneous inlet flow conditions is not significant.

In some papers [1-3], it was reported that the conclusion "the stable working range of transonic compressors could be expanded by reducing the aspect ratio of the blade" This was verified based on experimental results of single stage transonic compressors. However, from the experimental results of the two different



2 压气机 I ○准均匀流场 △畸变流场: $\theta = 90^\circ$ $\bar{D} = 18\%$ ($\bar{n} = 1.0$)

Figure 6

1-- $G_{0.98}$ (kg/sec); 2--Compressor I, 0 quasi-homogeneous flow, Δ distorted flow, $\theta = 90^\circ$, $\bar{D} = 18\%$ ($\bar{n} = 1.0$)

TABLE 2. The surge margins of Compressors I and II when $\bar{D}_{\bar{n}} = 0.98 = 15-16\%$.

状态 / 畸变程度 % \bar{n}	1.0	0.98	0.90	0.85	0.80
准均匀流场(压气机 I) 3	8.2	7.2	7.9	9	10
准均匀流场(压气机 II) 4		6.3	9	10	7.2
5 压气机 I $\bar{n} = 0.98$ 时 $\bar{D} = 16\%$		4	3	3	4.7
6 压气机 II $\bar{n} = 0.98$ 时 $\bar{D} = 15\%$		0.5	-0.4	1	1.8

1--condition; 2--surge margin %; 3--quasi-homogeneous flow (Compressor I); 4--quasi-homogeneous flow (Compressor II); 5--Compressor I when $\bar{n} = 0.98$, $\bar{D} = 16\%$; 6--Compressor II, when $\bar{n} = 0.98$, $\bar{D} = 15\%$

multi-stage compressors with different aspect ratios in the first stage blades, this conclusion was not completely verified.

Nevertheless, this experiment also verified another important phenomenon: Compressor I with a smaller aspect ratio blades compared to Compressor II with larger aspect ratio blades was able to improve the surge lines under inlet flow distortions more. The greater the distortion was, the more obvious the effect became (see Figures 4-6)*.

Unfortunately, we did not further use even small aspect ratio blades in our experiments.

TABLE 3. The surge margins of Compressor I under various distortions

工况	α 畸变度 % \bar{n}	1.0	0.98	0.95	0.90	0.85	0.80
3	准均匀流场	8.2		7.2	7.9	9	10
4	$\bar{n} = 1.0$ 时 $\bar{D} = 8\%$	3.3		3.5	6	8	9.5
5	$\bar{n} = 1.0$ 时 $\bar{D} = 12\%$	2.5		3.1	4.2	5.3	7
6	$\bar{n} = 1.0$ 时 $\bar{D} = 18\%$	-1.0		0	2	3.5	6
7	$\bar{n} = 0.98$ 时 $\bar{D} = 16\%$		4		3	3	4.7

1--condition; 2--surge margin %; 4--when $\bar{n}=1.0$, $\bar{D}=8\%$; 5--when $\bar{n}=1.0$, $\bar{D}=12\%$; 6--when $\bar{n}=1.0$, $\bar{D}=18\%$; 7--when $\bar{n}=0.98$, $\bar{D}=16\%$; 3--quasi-homogeneous flow

In fact, it has already been verified in [1] that another major reason to use small aspect ratio blades in the first stage of the transonic compressor was to eliminate the danger of vibrational loss of speed of the blades.

Comparing Figures 4-6, we found that for Compressor I or Compressor II, with increasing inlet flow distortion \bar{D} , the surge lines were shifted towards the lower right and the surge point flow was decreased. The latter was even more severe than the former. From Table 2 we found that under the same distortion $\bar{D}_{\bar{n}=0.98} = 15-16\%$, Compressor I still had 3-4.7% of surge margin while Compressor II almost ran out of any margin. From Table 3 we found that the surge margin of a compressor decreases with increasing \bar{D} .

From the experimental curves of α^* surge and \bar{D} obtained at

*(from previous page)

Due to the page limitations, the experimental curves corresponding to Compressor II were omitted.

rotational speeds $\bar{n} = 0.98$ and 0.90 for Compressors I and II, we found that the value of π_{*}^{*} surge decreased linearly with increasing \bar{D} . Compressor I at a rotational speed of $\bar{n} = 0.98$, in its peak efficiency, also decreased linearly with increasing \bar{D} .

III. DISTORTION ATTENUATION RATE

For a twin rotor engine, the outlet flow distortion of the low pressure compressor could also cause an adverse effect on the performance of the high pressure compressor. For a single axis engine, excessive compressor outlet flow distortion would have an adverse effect on combustion chamber performance. Therefore, in this experiment, preliminary measurements were made on the outlet flow of Compressor I. The results were not satisfactory because the individual probes on the II-II cross-section were facing the rear fringe of the third stage flow regulating blades and the results were affected by the tail traces. However, after partial correction, it was still possible to approximately observe the pressure distribution of the outlet flow. In the experiment, we determined the total outlet pressure when $\bar{n} = 0.98$ (see Figure 7). The corresponding distortion \bar{D} value was 3.5%. At this time, the \bar{D} value of the flow distortion with respect to the inlet and outlet was 10%. This showed that the compressor inlet flow distortion was strongly attenuated after passing through the three stage compressor. The distortion value at the outlet was about one-third of that of the inlet.

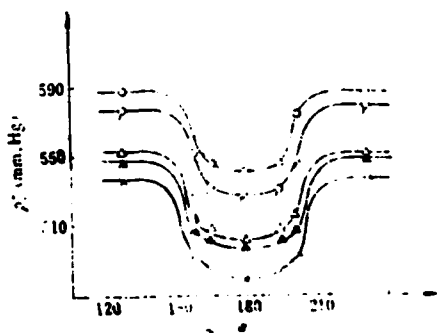


Figure 7(a)
1--condition point

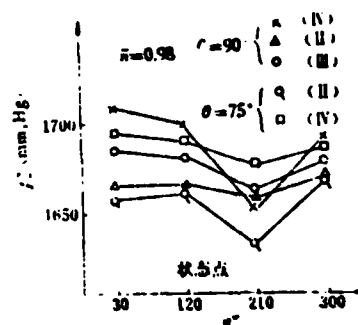


Figure 7(b)

In the meantime, the outlet temperature distributions of Compressor I, when $\bar{n} = 0.98$ with sector angle θ , 60° and 90° , were measured in the experiment. The measured results indicated that the pressure distortion of the inlet flow of the compressor causes a distortion of the outlet temperature field. Furthermore, the outlet temperature field relative to the inlet pressure field corresponds to rotation in the direction of rotor rotation.

/70

IV. PRELIMINARY CONCLUSIONS

(I) The distortion critical disturbance angle of Compressor I is $\theta_{Icritical} = 75^\circ - 90^\circ$, and $\theta_{IIcritical}$ of Compressor II = 60° . The former was not sensitive to inlet flow distortion and could stand inlet flow distortion disturbances over a larger area. It also had more intense distortion attenuation capability.

(II) Under identical conditions, compressors with smaller aspect ratio blades, relative to compressors with larger aspect ratio blades, have a larger stable working range, especially under inlet flow distortion conditions. They had larger surge margins which meant that the distortion-resistant capability was better. It was more suitable for airplane maneuvering.

(III) The pressure distortion of the inlet flow of the compressor causes a temperature distortion of the outlet flow of the compressor. The outlet temperature relative to the inlet pressure corresponds to a turn in the direction of rotor rotation.

V. CONCLUSIONS

Experimental work on inlet flow distortion of compressors has just begun. Due to lack of experience and other objective reasons, there were imperfections in all the links which are yet to be improved upon. The readers are welcome to present their valuable suggestions. This experiment was carried out on the compressor testing device at the Research Institute of Shenyang Aeroengine Company. The Comrades

of the second group in the third room have performed a large amount of work. We wish to express our thanks here.

With the increasing flight range of modern airplane flights, more rigorous requirements are placed on the operating characteristics of engines. Hence, improvement of distortion tolerance has already become one of the major topics to be studied. In order to further improve the compressor distortion tolerance and to expand the maneuvering range of the flight of airplanes, we are carrying out experimental studies in various casing treatments. This report only contained part of the experimental plan.

REFERENCES

- [1] Shenyang Aeroengine Company Experimental Report on the first stage compressor of the model B₁ engine.
- [2] J. D. D. Weil. Application of Advanced Material, Aircraft Engineering July 1968, vol. 40, no. 7.
- [3] Experimental study on the affect of aspect ratio on the axial-flow compressor supersonic stable working range*.
- [4] Robert, F., Plourde, G. A. and Smakula, F.,: Insight into Axial Compressor Response to Distortion, AIAA Paper No. 68-565.
- [5] C. Reid. The Response of Axial Flow Compressors to Intake Flow Distortion, ASME Paper No. 69-GT-29.
- [6] Northwest Industrial University "The Effect of Inlet Flow Distortion on the Performance of the Engine (I)", May 1976.
- [7] Roger W. Snyder and Robert J. Blade: Analytical Study of Effect of Casing Treatment on Performance of A Multistage Compressor, NASA TN D-6917.
- [8] Foreign Aeronautical Technology, Engine Type 3, (total no. 85), 1977.

* This paper was published in "3" vol. 3, 1964. The journal was lost and could not be located.

EXPERIMENTAL INVESTIGATIONS ON THE TURBULENT FILM COOLING EFFECTIVENESS OVER AN ADIABATIC FLAT PLATE*

Ko Shao-yen, Liu Deng-ying, Huang Liang-fu, Zhang Zheng-fang and Pan Wen-xin (Academia Sinica)

ABSTRACT

Experimental methods were used to determine the adiabatic temperature ratio η of turbulent flow cooling over a flat plate. The mainstream velocities in the experiment were 54-101 (m/sec). The jet velocities were 15-143 (m/sec). The mass flow rates M were 0.2-3.2. The mainstream temperature variation range was 40-148 ($^{\circ}\text{C}$). The jet temperature variation range was 24-67 ($^{\circ}\text{C}$). The experimental results are expressed using several correlations.

INTRODUCTION

A cooling jet was injected in the tangential direction near the wall surface to separate the high temperature gas from the wall surface. This type of protective cooling is flow film cooling. Flow film cooling has been widely used in main combustion chambers and/or the acceleration combustion chambers of modern gas burning turbine jet engines and the pulse pressure engines. The combustion chambers and nozzles of rocket engines can also use turbulent film cooling.

Recently, some authors carried out more studies in the turbulent film cooling process. However, the results obtained disagreed widely and could not satisfy the design requirements. For example, in the actual application, the effective cooling length x/s is relatively short and the flow rate M is approximately around 1. However, it was

* This paper was presented in the Second Engineering Thermal Physics Conference in Han zhou in November 1978.

reported in the literature [7-9] that the mass flow rate M was low and the experimental plate was too long due to the limitation of experimental conditions. The rear part of the experimental plate has already entered the turbulent boundary laminar flow region and the flow film cooling effect was very poor. Under this condition, the adiabatic temperature ratio formula obtained could not agree with the actual design requirements [5]. The experimental parameters were high and were close to the condition of actual engines. But, the actual temperature rise of the jet flow in the jet channel was not considered when the adiabatic temperature ratio was organized. Therefore, the results obtained were on the low side [4,6]. The more practical adiabatic temperature ratio correlation formula were presented.

According to the above situation described, this paper studied the calculating method of the adiabatic temperature ratio--emphasizing the organization of the correlation formula of the adiabatic temperature ratio in the jet mixing region. Part of the experimental results were published in [11].

BASIC EQUATIONS OF FILM COOLING

The flow of flat plate turbulent film cooling is as shown in Figure 1. Under normal conditions, y_1 is far less than the diameter of the flaming cylinder. Therefore, the flow film cooling flow inside the flame cylinder may be treated as the flat plate flow.

The velocity and temperature distributions in the jet mixing region are:

$$\frac{u - u_\delta}{u_\infty - u_\delta} = \left[1 - \left(\frac{y - \delta}{y_1 - \delta} \right)^2 \right] \quad (1)$$

$$\frac{t - t_{aw}}{t_\infty - t_{aw}} = \left[1 - \left(\frac{y_1 - y}{y_1} \right)^2 \right] \quad (2)$$

where u_δ is the flow speed of the boundary layer δ of the flow.

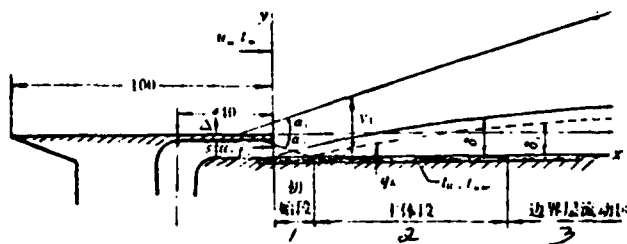


Figure 1. Simplified diagram of the flat plate turbulent film cooling flow.
1--initial section; 2--main section; 3--boundary laminar flow region

The adiabatic temperature ratio η is an important dimensionless temperature ratio correlation of an adiabatic wall flow film cooling. Its definition equation is

$$\eta = (t_m - t_{w,a}) / (t_m - t_i) \quad (3)$$

where $t_{w,a}$ is the adiabatic wall temperature which is the wall temperature of flow film cooling when the experimental plate is not heated; t_i is the average temperature of the jet gas being injected out of the jet channel ($x = 0$). In general, η is a function with the following correlations:

$$\eta = f(x/s, M, Re_s, Pr_s/Pr_m) \quad (4)$$

EXPERIMENTAL APPARATUS AND DETERMINATION OF THE FLOW

As for the mainstream flow entering the experimental section (see Figure 2), after being heated by the electric heater, the flow is homogeneous and the turbulence has been reduced. The jet flow was injected into the experimental section in the tangential direction after pressure reduction stabilization. The jet channel light s was limited by a jet spacing plate with a thickness $\Delta = 2$ and $s = 2.3$ mm. The spacing plates used were the removal be flat head and sharp head types.

The experimental flow plate was 398 mm long, 12 mm wide and the material was 2x18 stainless steel. In order to reduce the transverse heat flow along the plate length, there were 40 deep grooves on the back of the plate. The bottom of the groove was 0.4-0.5 mm away from the surface. The grooves began from the front and were distributed first densely and then far apart. The ϕ 0.5 mm nickel chromium-nickel aluminum thermocouples used to measure the wall temperature were installed on the bottom of 22 grooves on the back of the plate. Sufficient heat insulating material was filled under the experimental flat plate to create a good thermal insulating condition for the experimental flat plate.



Figure 2. The experimental section and the tracing device

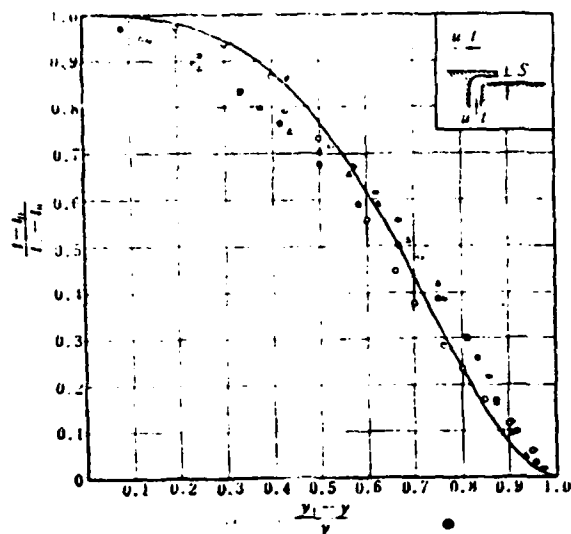
This experiment used the determined velocity distribution and temperature distribution to evaluate the flow field in the channel of the experimental section. The temperature distribution was shown in Figure 3 which agreed with the temperature distribution equation (2) approximately [3].

PHOTOGRAPHY OF THE TRACING DEVICE

An 80 mm diameter light beam tracing device was used to carry out observations of the flow field near the jet tank and a series of photographs had been taken for the jet flow mixed boundaries. Figure 4 shows two typical photographs.

Figure 4a showed that when the sharp headed spacing plate was used, there was no displacement in the jet extremum point. The flow was more homogeneous and the inner and outer boundaries of the mixing region were both straight lines. However, the disadvantage was that the effective jet groove height was increased near the tip of the plate. Correspondingly, the jet flow velocity was decreased and the

175



1 符号	速度 [米/秒] 2			温度 [°C] 3			距离 [毫米] 4	槽高 [毫米] 5	备注 6
	u_m	u_s	m	t_m	t_s	θ			
○	101.36	137.4	1.356	104	30.05	0.803	45	2.3	
○	101.46	137.4	1.356	104	30.05	0.803	140	2.3	
△	101.46	137.4	1.356	104	30.05	0.803	250	2.3	
◇	101.36	137.4	1.356	104	30.05	0.803	390	2.3	
7 实验序号	108								

Figure 3. The dimensionless temperature distribution of adiabatic flat plate under flow film cooling.
1--symbol; 2--velocity (m/sec); 3--temperature (°C); 4--distance (mm); 5--slot height (mm); 6--remarks; 7--experimental sequence



a
 $U_m = 38.0 \text{ m/s}$ $U_s = 125.0 \text{ m/s}$
 $t_m = 47.2^\circ\text{C}$ $t_s = 25.0^\circ\text{C}$
 $M = 3.80$



b
 $U_m = 71.1 \text{ m/s}$ $U_s = 62.0 \text{ m/s}$
 $t_m = 54.5^\circ\text{C}$ $t_s = 33.3^\circ\text{C}$
 $M = 0.95$

Figure 4. Tracing photographs a, b

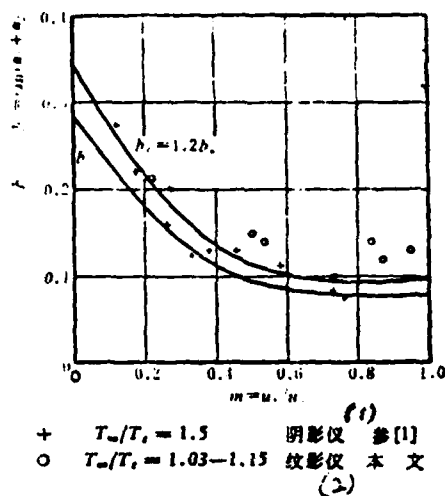


Figure 5. Variation of the tangent of the angle between the mixing region boundaries with m measured by the tracing method.
 1--shadow device, reference [1]; 2--tracing device, this work

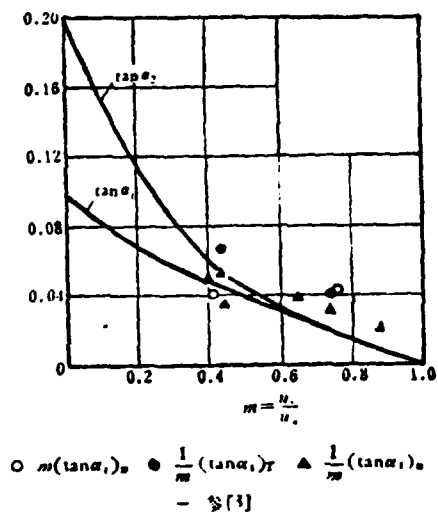


Figure 6. Variation of the tangent of the jet stream mixing region boundary angle with m .
 1--reference [5]

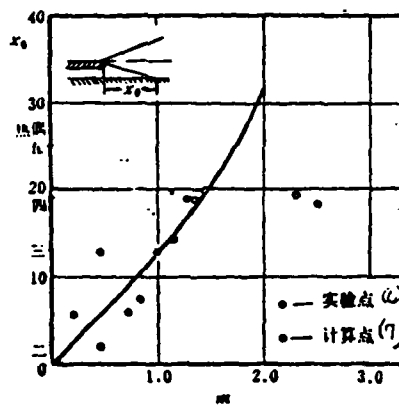


Figure 7. Variation of the initial section length in the jet flow mixing region with m .
 1--thermal couple; 2--five; 3--four; 4--three; 5--two; 6--experimental point; 7--calculated point

flow film cooling effect was reduced. Figure 4b is the formation condition of the jet boundary when the flat top plate height was M . The mixing boundary line was approximately in the form of a straight line.

Figure 5 is the variation regularity of the tangent of the angle between the inner and outer boundaries ($\bar{b}_1 = \tan \alpha_1$, $\bar{b}_2 = \tan \alpha_2$) with m in the jet mixing region measured from a batch of photographs. The results approximately were in agreement with [1]. Figure 6 shows the tangents of the jet flow boundary angles, i.e., $(\tan \alpha)_T$ and $(\tan \alpha)_n$, measured according to the temperature and velocity distributions. At this time, the mixing boundary was selected at 95% of the mainstream temperature and velocity. When $m > 1$, the results of the inverse of m and those of $m < 1$ were symmetrical. The photographs of this type of flow film cooling and boundary formation were rarely reported in the literature.

THE PROBLEM OF \bar{t}_s

The average jet temperature \bar{t}_s of the jet tank outlet is an important parameter in flow film cooling. The difference is that the different measurement methods of \bar{t}_s was one of the factors which caused the inconsistency of the results in the literature.

In this paper, the lowest adiabatic wall temperature measured, using the second through the fourth thermocouples (their positions were $x/s = 0.217, 5.65, 8.26$) near the jet tank, was used as \bar{t}_s . There were two major reasons for this selection method: (1) the insulation of the experimental plate was really good. Experimental results indicated that the temperature distribution of the flow near the slot was perpendicular to the tested flat plate. Hence, it is possible to use an adiabatic wall temperature to express the flow temperature on the cross-section near the wall surface. (2) from the model in Figure 1 we found that in the initial section range the unpenetrated jet flow covered the adiabatic plate. According to the half wall jet stream theory, the temperature at any point on the adiabatic plate at

this time is equal to the temperature of the jet stream. As shown in Figure 7, the initial section length of the jet stream mixing region lengthens with increasing $m = u_s/u_\infty$.

ADIABATIC TEMPERATURE RATIO

The great amount of experimental results in this work should that when the mainstream and jet stream were air, the adiabatic temperature ratio η mainly varied with x/s and M . From Figure 8, we found that the exponent of x/M_s varied with M . The exponent of x/M_s was a constant because its experimental M value was also a constant [7,10].

Figure 9 gives the variation of η with M . Obviously, $M < 1$ and $M > 1$ were two different regions. Furthermore, we found that in the initial section and the beginning of the main section of the jet stream (about $x/s < 44.8$), after M reached a certain value, even if when M was increased, η no longer continued to increase, but stabilized at a given value. This indicated that at this time, even by increasing jet flow, the cooling effect no longer would be improved. This region was the right upper corner triangular area at $M < 1$ in Figure 9. The reflection point of η when reaching a stabilized value was on a straight line.

From the experimental results, we obtained the following adiabatic temperature ratio correlation formula: (1) when $M < 1$

$$\eta = 2.73M^{0.4}(x/s)^{-0.38} \quad (x/s \leq 20) \quad (5)$$

$$\eta = 4.55M^{0.4}(x/s)^{-0.38} \quad (20 < x/s < 150) \quad (6)$$

$$\eta = 2.04(x/s)^{-0.15} \quad (7)$$

when $x/s < 65.2$ and $0.45 < M < 1$, the lower value of η from Equations (16) and (7) was chosen.

(2) when $1 \leq M < 2$:

$$\eta = 1.96M^{0.15}(x/s)^{-0.38} \quad (x/s < 150) \quad (8)$$

(3) when $2 \leq M < 3.5$:

$$\eta = 2.71(x/s)^{-0.38} \quad (x/s < 150) \quad (9)$$

/77

From Figure 10, the direct comparison of equations (6) and (8) in this work and several other equations in the literature were given. In the figure, we chose $M = 0.3, 0.8, 1.3$ and 1.5 . x/s was chosen to be between 10-100. The formula used are listed in the following table.

Comparison table of adiabatic temperature ratio formula

1 作者	2 公式	3 范围	4 [参考文献]
Scesa (1954)	$\eta = 2.20(x/Ms)^{-0.3}$		[3]
Hartnett Birkeback Eckert (1961)	$\eta = 16.9(x/Ms)^{-0.3}$	$M = 0.28$ $x/Ms = 60-1000$	[7]
Seban (1960)	$\eta = 25M^{0.4}(x/s)^{-0.3}$	$x/Ms^{1.3} > 56$	[6]
5 本文	6 式(6) 式(8)	$M < 1, 20 < x/s < 150$ $1 \leq M < 2$	

1--author; 2--formula; 3--range; 4--[reference]; 5--this work; 6--equation

From Figure 10, we could see that for various M values the formula given in this paper gave more reasonable results. Especially when $M > 1$, equation (8) provided a reasonable result while the other formulas were not applicable. When $M = 0.3$, the results by Hartnett and Seban are more or less in agreement with equation (6) in this paper. However, as described earlier in the paper, low M values do not have any practical value.

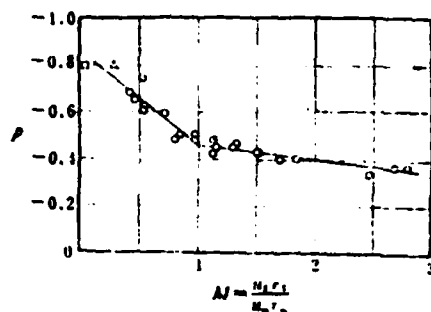
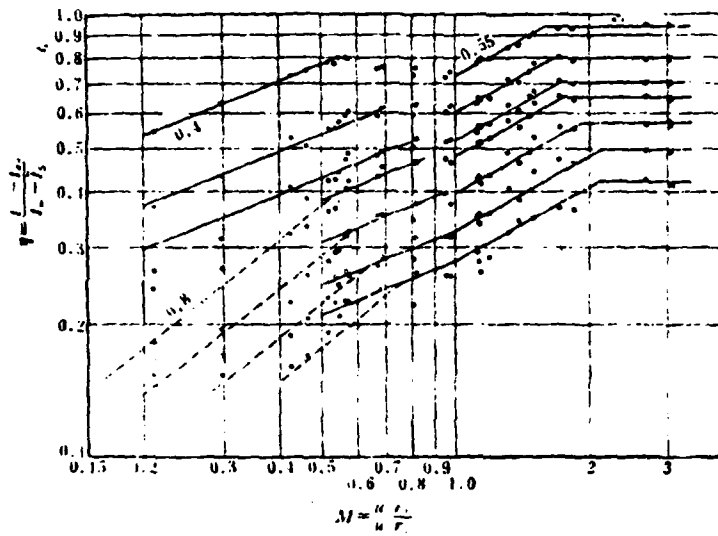


Figure 8. Δ ref. [8]
ref. [10]
O Exponent P of $(x/Ms)^P$
versus M measured.

CONCLUSIONS

1. In the given experimental range, the adiabatic temperature range can be expressed by equations (5)-(9). Among them, equations (6) and (8) are more important. The remaining three equations are



177

Figure 9. The variation of the adiabatic temperature ratio with M .

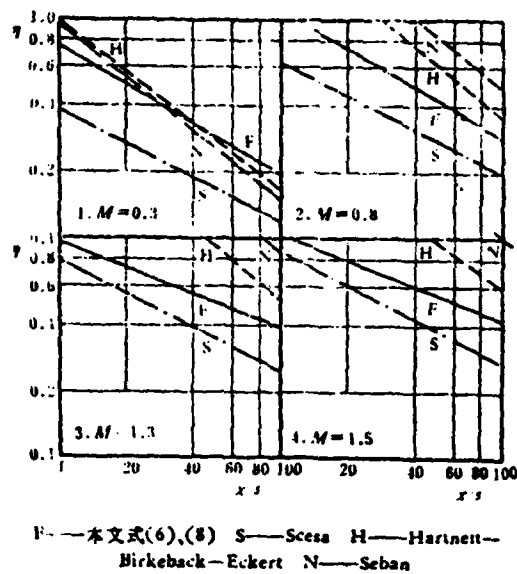


Figure 10. Comparison of the adiabatic temperature ratio in this work and the literature.

the auxiliary equations of the two above equations.

2. From Figures 8, 9 and 10, we can find that the x/M_s correlation commonly used in the literature and the -0.8 exponent of this correlation are mostly limited to $M = -.01-0.5$ and in the range when x/s is high. This range does not agree with the actual condition of turbine jet engine flame cylinders. Therefore, finally in this paper, these types of correlation formulas were used.

TABLE OF SYMBOLS

$m = u_s/u_\infty$	flow velocity ratio
$M = u_s r_s / u_\infty r_\infty$	mass flow rate
s	jet tank height, mm
x	length of the flat plate starting from the jet tank outlet, mm
y_1	distance from the outer boundary of the jet stream mixing region to the flat plate, mm
α_1, α_2	angle between the inner and outer boundaries of the jet stream mixing region
Subscripts:	
aw	adiabatic condition
s	jet flow condition

1. Zhestkov, B.A., V.V. Tlazkov, M.D. Guseva. Method for calculating the wall temperature in the case of jet and combination cooling. (1955).
2. Borodachev, V.Ya. Theoretical and experimental study of air-barrier cooling of a plane plate. (1956).
- [3] Seesa, S. Effect of Local Normal Injection on Flat-plate heat Transfer, Ph. D. Thesis, University of California, Berkeley, California. (1954)
- [4] Chin, J. S., Skirvin, L. Hayes, A. Silver, Adiabatic Wall Temperature Downstream of a Single Injection Slot, ASME Paper No. 58-A-104. (1958)
- [5] Papell, S., A. M. Trout, Experimental Investigation of Air Film Cooling Applied to an Adiabatic Wall by Means of an Axially Discharging Slot, NASA TN-D-9. (1959)
- [6] Seban, R. A., Heat Transfer and Effectiveness for a Turbulent Boundary Layer with Tangential Fluid Injection, Jour. Heat Transfer, Trans. ASME, 82. (1960)
- [7] Hartnett, J. P., R. C. Birkeback, E. R. G. Eckert, Velocity Distributions, Temperature Distributions, Effectiveness and Heat Transfer for Air Injection Through a Tangential Slot into a Turbulent Boundary Layer, Jour. Heat Transfer, Trans. ASME, 83. (1961)
- [8] Nishiwaki, N. M. Hirata, A. Tsuchida, Heat Transfer on a Surface Covered by Cold Air Film, International Developments in Heat Transfer, Part IV. (1961)
- [9] Hartnett, J. P., R. C. Birkebak, E. R. G. Eckert, Velocity Distributions, Temperature Distributions, Effectiveness and Heat Transfer in Cooling of a Surface with a Pressure Gradient, International Developments in Heat Transfer, Part IV. (1961)
- [10] Goldstein, R. J., G. Shavit, T. S. Chen, Film-Cooling Effectiveness with Injection Through a Porous Section, Jour. Heat Transfer, Trans. ASME, 87. (1965)
- [11] Ko Shao-Yen, Deng-Ying Lu, Experimental Investigations on Effectiveness, Heat Transfer Coefficient and Turbulence Distribution of Film Cooling, Proceedings of Fourth International Symposium on Air Breathing Engines, Orlando, Florida, U. S. A. April 1-6, 1979. Paper 79-7047.

EXPERIENCE ON DEVELOPING AN ANNULAR COMBUSTOR OF "A" TYPE* TURBOJET ENGINE

Zhang Bao-cheng, Hou Yu-tian, Huang Dian-fu and Huang Zhao-xiang
(Shenyang Aeroengine Company) (Academia Sinica)

ABSTRACT

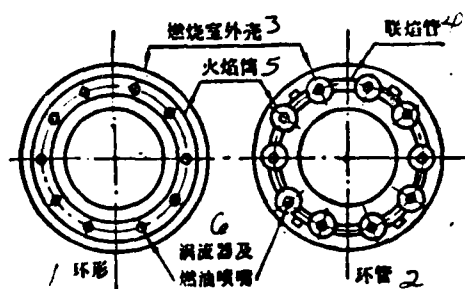
This paper briefly described the technological targets and the design characteristics of the annular flame tube of the type A engine. Emphasis was placed on explaining that the adjustment of the flame tube on an engine test stand can control the flow distribution. In the adjustment, the flow distribution in the main combustion zone dilution zone--auxiliary zone should be close to the ratio of 30%-30%-40%. Air used in flow film cooling should be controlled at under 25%. In the paper, it was also shown that by controlling the relevant parameters of temperature, the homogeneity of the temperature field could be improved. By choosing the proper flow passing through the inner and outer annular ducts, it was possible to ensure the better distribution of the combustion gas temperature along the blade height direction. In the adjustment method, one adjusts temperature t_4^* to indirectly adjust t_3^* . The experiment results realized the design targets of raising R by 2% and reducing C_R by 1.5%.

INTRODUCTION

The annular combustion chamber has more advantages over the loop combustion chamber (Figure 1), especially in the low flow loss of the combustion chamber, homogeneous outlet temperature, better flame connection, low breakdown rate and simplicity in technology. If one

* This paper was presented in the Second National Engineering Thermal Physics Conference in Hangzhou in November 1978.

considers an annulus and a ring of the same inner and outer diameters, if the same unit area cooling air mass is required, the annulus can save one-third of the cooling air [1]. Thus, it is more advantageous to organize the combustion and to use the gas economically.



At present, the advanced engines abroad have already widely adopted this annular combustion chamber. The change of type A turbojet engine (from here on

Figure 1. Comparison of two types of combustion chambers.
1--annulus; 2--ring; 3--external shell of the combustion chamber; 4--flame connecting tube; 5--flame tube; 6--vortex device and fuel nozzle

it is called type A engine for short) to the annular flame tube was based on the improvement of the flame tube structural design in order to raise the component performance, to reduce the weight, to minimize breakdown and to extend the useful life.

I. DETERMINATION OF TECHNICAL OBJECTIVES

The technological objectives of the design adjustment of type A annular flame tube (annulus I for short from here on) are as follows:

1) The annulus I should raise R by 2% and reduce C_R 1.5% for type A engines.

2) The ground starting characteristics when using two ignition devices (originally four ignitors were used) must not be lower than those of the original flame tube for annulus I. It can guarantee the restarting of the engine at a flight altitude of under 9000 meters.

3) Good lean and rich fuel stopping characteristics. The engine should not stop when the throttle is rapidly cut and no surge and cracking sound should occur during acceleration.

- 4) The outlet temperature t_3^* distribution is:

$$\delta, \leq 20\%; \quad t_{3max}^*/t_{3pj}^* = 1.04-1.05.$$

Based on the experience on the indirect adjustment of t_3^* by adjusting t_4^* distribution for type A engine, it must make t_4^* satisfy the following to realize the above objectives:

- a. $\delta, \leq 16\%$;
- b. $t_{pj}^* - t_{20pj}^* \geq 40^\circ\text{C}$; $t_{pg}^* \leq 620^\circ\text{C}$; $t_{max}^* - t_{20pj}^* \leq 120^\circ\text{C}$;
- c. $\Delta t = |t_{20pj}^* - t_{pg}^*| \leq 10^\circ\text{C}$; $\Delta T = |t_{20}^* - t_{pg}^*| \leq 10^\circ\text{C}$;

- 5) The weight is lighter by 3 kilograms as compared to the ring tube for each unit.

- 6) The useful life is 250-300 hours.

II. ADJUSTMENT METHODS

The flame tube testing was divided into a simulated single tube test and the complete engine test stand adjustment. Single tube tests can directly measure the η_3 , σ_3^* , stable combustion range and t_3^* distribution and after the flame observation capability.

The complete engine test stand adjustment does not have any simulated problem. It can provide the actual flow field and the flow parameters. It can also directly access the effectiveness of the improvement procedures made on the combustion chamber. For the improvement of the engine combustion chamber already in mass production, it is more suitable for complete engine test stand adjustment.

In general, it is possible to determine the individual adjustment of the effectiveness of the flame tube of the complete engine through the following parametric evaluation when other components are kept unchanged:

- 1) The increase in R can be considered as the improvement in σ_3^* . By rough calculation, to improve σ_3^* by 1% for type A engines,

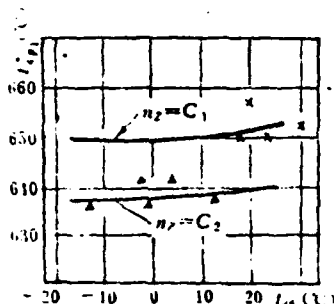


Figure 2. t_{dq} vs. t_{4pj}^* curves for type A engines

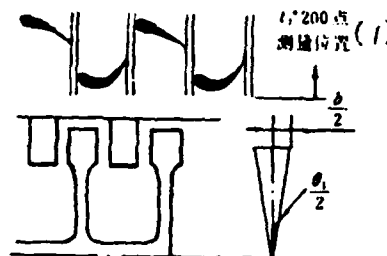


Figure 3. Schematic diagram of fuel gas passing through the turbine channel
1--measuring position of t_1^* 200 point

R can be improved by 0.65%.

2) The decrease in C_R is primarily the result of the improvement in η_3 . The effect of σ_3^* is small. By rough estimation, to raise η_3 by 1%, C_R can approximately decrease by 1%.

3) For type A medium pressure ratio engines, the measured t_{4pj}^* curves (Figure 2) when the atmospheric temperature t_{dq} has at -20° – 30°C showed that: when n_z remained unchanged t_{4pj}^* did not vary significantly with t_{dq} . Hence, it is possible to use this characteristic to determine the temperature of this type of engine. For experiments carried out under different atmospheric conditions, the absolute values of t_4^* are comparable.

Between t_3^* – t_4^* , there must be some corresponding relations as shown in Figure 3: the high temperature fuel gas after passing through the guide and turbine to reach the measuring thermocouple position for t_4^* must have been shifted by an angle in the direction of rotation of the guide and the turbine. The rotation angle of type A engine was experimentally determined to be about 36° . Hence, based on the t_{4max}^* , δ_4 and the high temperature distribution along the blade height measured on the test stand, the t_3^* distribution can be determined to evaluate the effectiveness of improvement by "operating on" the flame tube.

4) Through the acceleration, deceleration, maneuverability of the engine to test the combustion stability and temperature rise rate.

5) Through the test stand starting test to evaluate the ignition and flame connection characteristics of the flame tube. /97

6) Through the painting of temperature indicating paint on the wall to measure the temperature distribution on the flame tube wall when the test stand was under maximum operating conditions to expose the local high temperature zone on the wall and to observe the effectiveness of the improvement measures.

III. DESIGN CHARACTERISTICS AND ANALYSIS

1. The use of elliptical tips

Annulus I used 10 elliptical tips to satisfy the structural condition of the original 10 full nozzles of type A engine. The photograph shows its external appearance.

The use of an elliptical tip avoided the high flame tube cavity caused by using a round tip (Figure 4) to make the structure more compact. In order to obtain a reasonable structure and to extend the lifetime, it is necessary to keep the heat capacity lower than that of the original flame tube. Let us take the cavity height as 127 mm (the original flame tube cavity height was 136 mm) for annulus I. The length to height ratio of the flame tube was 3.55 which agreed with the 2.6-5.0 range for an ordinary flame tube length to height ratio.

The use of elliptical tips also could sufficiently utilize the radial space around the tips to increase the volume of the main combustion zone. According to a calculation, the volume of the elliptical tips of annulus I increased by 35.5% over that of a seven stage gas film flame tube (seven stage for short from here on). This is

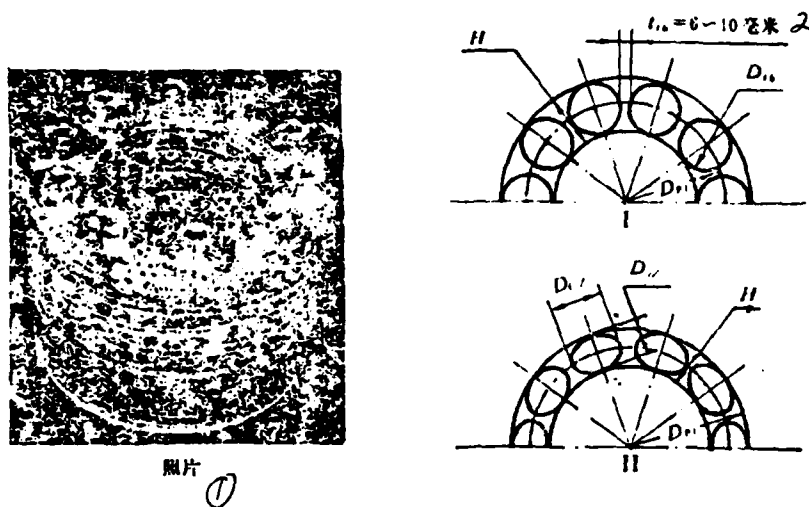


Figure 4. Comparison of elliptical and round tips
1--photograph; 2--mm

advantageous for the improvement of combustion efficiency to reduce C_R .

2. Hole opening forms

Small holes at the tip were used for annulus I. The main combustion holes were flange holes. The tube body takes in air vertically. In the dilution section, large holes (inner ring) were used (see the photograph).

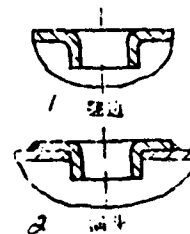


Figure 5. Schematic diagram of the flanging hole and the funnel
1--flanging hole; 2--funnel

Compared with flush holes, the use of funnel shaped main combustion holes would improve η_3 by 1% and reduce C_R by about 0.005-0.01. The use of flanging holes as compared to funnel shaped holes (Figure 5) would reduce C_R by about another 0.01. The flanging has a higher flow coefficient which makes it easier for the jet stream to reach the center of the flame tube. This enables the elimination of the local fuel rich vortex nucleus and the improvement in combustion efficiency.

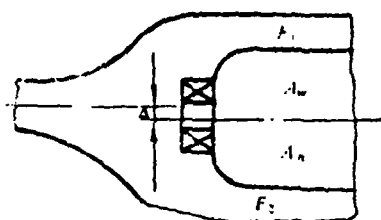


Figure 6. Flame tube of A type A engine.

Table 1. Temperature field indicators using various apertures

孔 径	δ, %	t_{max}	热区占横截面积比例 2
15-φ28	14.3	744	15.5
15-φ19 15-φ21	20.0	775	19.0

1--aperture; 2--ratio of heat area vs. cross-sectional area of thermal ejection

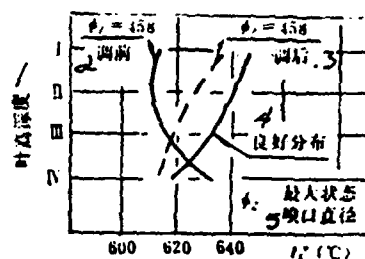


Figure 7. Temperature distribution along the blade in a flame tube
1--blade height depth; 2--advanced; 3--lagging behind; 4--good distribution; 5--nozzle diameter under optimal condition

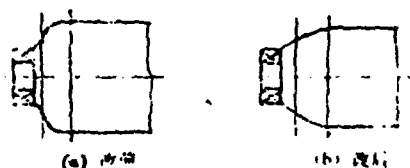


Figure 8. Improvement of the rotating connection section in the tip of the annulus I flame tube
1--(a) before; 2--(b) after

The adjustment of the dilution hole would directly affect the outlet temperature and radial temperature distributions. Because the difference of the radial positions of the center line of the outlet channel of the type A engine compressor and that of the flame tube Δ is too large (Figure 6), the air mass flow in the outer ring II channel would be greater than the one obtained from the usual area distribution law $F_1/F_2 = n \cdot A_w/A_n (n \leq 1)$. The areas of the holes on the inner and outer walls of the first two experimental units on ring I followed the $A_w/A_n = A_{k.w}/A_{k.n}$ law, due to the fact that the annular flame tube could not maintain the balance automatically as the pressure in the channel II of the ring tube. Therefore, three mutually isolated channels were formed which caused the actual external wall inlet gas flow to be slightly larger. The symmetry about the center

/98

of the flame could not be assured. Finally, the temperature at the root of the blade became too high which is a disadvantage (Figure 7).

Annulus I used a reduced gas inlet area on the external wall holes to adjust A_{kw}/A_{Kk} to 0.97 in order to obtain a more reasonable temperature distribution along the blade height.

In the adjustment of dilution holes it was found that: when the total hole opening area was unchanged, the use of a smaller number of larger holes could obtain a better penetration depth than using a larger number of small holes. The homogeneity of the temperature field was improved. Table 1 listed this result.

3. Total pressure loss

In the adjustment of annulus I, in order to minimize the pressure loss, the rotating connection section of the tip was changed from Figure 8(a) to (b) to improve the streamline. Test stand results indicated that: after modification, R_z was raised by 70 kg and more.

According to the inlet parameters of the combustion chamber of type A engine, t_3^*/t_2^* , structural parameters of annulus I and hole opening area, the magnitude of σ_3^* can be estimated by using the following equation and the curves in [2]:

$$\sigma_3^* = 1 - K / \{ 2[1 + (K - 1)M_1^2/2]^{K/(K-1)} \} \psi'' (A_1/A_{cK})^2 M_1^2 (M_1 \leq 0.3) \quad (1)$$

where $\psi'/\psi'' = (A_1/A_{cK})^2$, and the flow resistance coefficient

$$\psi' = (\rho_1^* - \rho_3^*) / (\rho_1 V_1^2/2) = \Delta p^* / q_1.$$

Equation (1) gave the σ_3^* calculated using the maximum cross-section (A_{cK}) as the reference cross-section.

Table 2 lists the comparison of the estimated values of σ_3^* for annulus I and the R values recorded on the test stand. Table 3 shows the value of p_2^* , p_3^* and σ_3^* measured with annulus I. The numbers 4 and 5 represent the measured results obtained under different experimental units and different hole opening conditions as compared to the first three. From the estimated and measured values, we first found that:

Table 2. Comparison of the estimated value of σ_3^* for the annulus I flame tube to the performance of the engine stand test.

参数	2 实验	3 I-2	4 I-3	5 I-4	6 I-3	7 I-4	8 备注
σ_3^*		0.929	0.921	0.921	0.921	0.921	9 估计值
ΔR		645	645	646	644	644	10 实验值
A_{Kt}/A_{cK}		0.291	0.275	0.265	0.255	0.255	
ϕ		22.0	23.1	23.6	24.3	24.3	

1--parameter; 2--experimental unit; 3--annulus I-2; 4--annulus I-3; 5--annulus I-4; 6--annulus I-3; 7--annulus I-4; 8--remarks; 9--estimated value; 10--experimental value

Table 3. Measured p_1^* , p_3^* and σ_3^* of the annulus I flame tube

参数	状态 / 序号	1	2	3	4	5
p_1^*	1	6.52	7.90	7.98	7.64	7.58
p_3^*	2	6.09	7.39	7.48	7.04	6.92
σ_3^*	3	0.913	0.916	0.937	0.922	0.913

1--condition; 2--number; 3--parameter

1) When A_{Kt}/A_{cK} decreases, σ_3^* is reduced and R is also reduced. When A_{Kt}/A_{cK} stays the same, R also will remain the same. This law has a very significant meaning to the test stand adjustment of flame tubes.

2) The measured values were very close to the estimated values and the measured values were about 1% higher. The approximation of the curve and the accuracy in the measurements were the causes creating this error.

In summary, σ_3^* was in the range of 0.925 to 0.93 when using annulus I for the type A engine and the measured values of σ_3^* for the seven stages were in the 0.905 to 0.91 range.

4. Main combustion zone lean fuel design.

/99

In the adjustment of annulus I, the gas flow has been continuously increased in the main combustion zone. When the performance and temperature indicators were all good, the gas flow rate in the main combustion zone was increased from 22.7% to 27.8% of the total flow which was close to 30%. At this time, α increased from 0.93 to 1.14 which was in the usual lean fuel design parametric range (1.1-1.2).

Because the α values in the combustion zone for annuli I-3₍₃₎ and I-4₍₆₎ were large (1.14), therefore, the $\Delta C_{RZ}, \Delta C_{RE}$ were lower than those of the seven stage by 0.01 or more. t_{\max}^* was also lower than that of the seven stage by 40°C or more. Furthermore, δ_{200} decreased to 14% which was 22% lower than the seven stage. This indicated that the lean fuel main combustion zone had a higher heat release rate than the rich fuel main combustion zone. The radial temperature was more homogeneous and the hot zone temperature was even lower.

5. The adjustment of the temperature field geometrical relevant parameter K_{sg}

K_{sg} is defined as:

$$K_{sg} = L_{fg}^2 / A_{fg} \quad (2)$$

where $L_{fg} = L_{ht} / H_{ht}$ is the dimensionless length of the flame tube; $A_{fg} = A_{ht} / A_{fg}$ is the ratio of the total hole opening area of the flame tube and the cross-section of the flame tube. The value of K_{sg} is the relevant parameter for obtaining a given fuel gas temperature distribution in front of the turbine. The larger K_{sg} is, the higher the possibility of obtaining a homogeneous combustion chamber outlet temperature will be. In addition, δ_{200} is lowered. Table 4 shows

Table 4. Comparison of K_{sg} in the adjustment of annulus I

/100

参数 2	试验件 /	七段 3	环 I-3 4	环 I-3, 5	环 I-4 6	环 I-4, 7
A_{sg}		1.047	0.517	0.494	0.171	0.465
K_{sg}		11.65	28.04	29.33	30.80	31.28
δ_{200}		≤ 25	19.3	13.8	16.8	15.4

1--experimental unit; 2--parameter; 3--seven stage; 4--annulus I-3;
5--annulus I-3; 6--annulus I-4; 7--annulus I-4

Table 5. Comparison of cooling air flow rate of several types of engines

发动机 2	参数 /	G_{L_0}	G_{L_0}/G	G_{L_0}/A_{L_0}
3	A 型机装环 I-4	10.25	23.88	7.75
4	A 型机装七段	12.90	30.06	6.25
5	B 型机用	23.80	37.36	8.90
	SPRY	16.40	32.93	10.8
	J-17M	38.90	49.87	10.0

1--parameters; 2--engine; 3--type A engine equipped with I-4;
4--type A engine equipped with seven stage; 5--type B engine

that when the K_{sg} values of annuli I-3 and I-4 increased, δ_{200} was reduced to 5.5% and 1.4%, respectively.

When A_{sg} remains unchanged, the value of K_{sg} increases with increasing L_{sg} which means that the lengthening of the flame tube can increase the duration of stay of the fuel gas in the flame tube to more sufficiently mix the fuel gas with the diluting air so that the homogeneity of the temperature field can be improved. When L_{sg} is fixed, to increase K_{sg} corresponds to the reduction of A_{sg} . In fact, this is realized by reducing the flame tube hole opening area to improve the gas flow pressure loss which consequently will lead to the reduction of R . Such as in the adjustment of annulus I-4, when K_{sg} was changed from 30.80 to 31.28, ΔR_z dropped by 30 kg. In the adjustment of annulus I, $K_{sg} = 30$ was chosen as the adjustment base value.

6. Flow film cooling problem

Annulus I underwent several cooling gas flow rate adjustments. After successfully accomplishing all the technological objectives of the flame tube, its G_{L}/G was about 23.88% (Table 5). At this time, the flame tube wall temperature was uniform. Temperature indicating point measurements indicated that: 70% of the inner and outer annular wall of the flame tube was at 550°C. The wall temperature of the inner and outer tubes was at 700-750°C. The local wall temperature in the main combustion zone reached 720°C. Annulus I did not show the local high temperature zone (850-900°C) in the downstream downwind of the flame connection tube of the seven stage flame tube.

IV. CONCLUSIONS

After several adjustment and stability tests, I realized the objectives of 2% increase on R and 1.5% decrease in C_R (Table 6). The outlet temperature was stabilized. It created conditions for starting life test and field test flights. Through the experiments, we realize that:

1) the adjustment of flame tubes must control the gas flow rates. First, the flow rate in the main combustion zone must be adjusted to improve the combustion efficiency and then the dilution zone flow rate is adjusted to obtain a good outlet temperature field.

2) the amount of air combusted in the main combustion zone, the dimension of the vortex in the main combustion zone, and the extent of fuel-air mixing may vary significantly. Annulus I used a lean fuel-air mixture main combustion zone whose flow rate reached 27.8%. Experimental results indicated that the main combustion zone gas flow approached 30%, i.e., $\alpha = 1.2$ is appropriate.

3) the use of larger holes in the adjustment of the dilution zone performance was not only applicable to ring tubes but also to annuli.

Table 6. Comparison of the average performance of pilot production annulus I and that of the seven stage (same engine)

/101

3 火焰筒类别	2 状态	JL		L		E		0.8E	200点温度场			
		$\frac{n}{\Delta K}$	$\frac{\Delta C_R}{t_0^2}$	$\frac{n}{\Delta K}$	$\frac{\Delta C_R}{t_0^2}$	$\frac{n}{\Delta K}$	$\frac{\Delta C_R}{t_0^2}$	$\frac{\Delta C_R}{t_0^2}$	$\frac{t_{200}^2}{t_{200}^2}$	$\delta_{100} \%$	$\frac{\Delta T}{\Delta t}$	ϕ_2
环 I (五台平均)	4	11152 +140	-0.0525 654	11142 +100	-0.02 640	11114 +91	-0.015 546	-0.035 425	718 629	14.1	-7 7.2	458
七段 (年平均)	5	11116 -10	-0.075 644	11129 -7	-0.02 644	11145 -11	-0.011 544	-0.024 449	778 625	-22	-10 ≤10	458
按设计指标提高	6			+53	-0.015 645	+43	-0.015 540		-750	≤16	≤10 ≤10	458

注：耗油率“-”号表示比额定值少耗油，绝对值越大，耗油率越低。 7

1--condition; 2--parameter; 3--type of flame tube; 4--annulus I (average of five); 5--seven stage (annual average); 6--increase in design objective; 7--the "fuel consumption rate" with a "-" sign represents that it consumes less fuel than the allowable value. The larger the absolute value, the smaller the fuel consumption rate is; 8--200 point temperature field

The dilution zone air flow should be 30%.

4) the selection of a proper Ksg is a more practical method. In the adjustment of a flame tube temperature, K_{sg} should be raised as much as possible to obtain a more uniform temperature field.

V. EXISTING PROBLEMS

The rigidity of the external tube of annulus I was weak. This was determined by the large diameter thin wall annular shaped structural characteristics which may affect the useful lifetime. In the future, further steps will be taken to improve its cooling and to raise its rigidity. The hot zone in the temperature field carries out certain movements. This is one of the special points which distinguishes the annular shape from the ring tube. The radial movement of the hot zone of the t_{40}^* temperature field for annulus I was statistically determined to be about 15-24°.

In the developmental stage, we have received guidance and assistance from some comrades at Beijing Aeronautical Institute. Those

who also participated in this work are: Su Xiu-shan, Zhu Jin-can, Guo Yong-quan, etc. Comrade Zhang Qin has carefully corrected and plotted the figures in this paper. We wish to express our sincere gratitude here.

TABLE OF SYMBOLS

A	area, cross-sectional area of the flame tube, m^2
C_R	fuel consumption per unit propulsion, kg/kg propulsion hour
E	fixed condition (same as a subscript)
G	combustion chamber inlet flow rate Kg/sec
H	cavity height of the flame tube, mm
L	length of the flame tube, mm
n	number of turns, proportionality index rotation/mm
R	propulsion, kg
t	temperature, $^{\circ}C$
Z	maximum condition (same as a subscript)
δ	inhomogeneity of the temperature field $(t_{4max} - t_{4min}) / t_{400p}$ %
α	gas coefficient
η	combustion efficiency, %
σ	pressure restoration coefficient, %

Subscripts:

bm	wall surface	pj	average
cK	reference cross-section	sg	relevant
ht	flame tube	tb	tip of the flame tube
K	constant	W	outer ring of the flame tube
Kt	cylindrical section of the flame tube	yg	flame tube
kl		yj	blade tip
Le	cooling	y σ	right engine
n	inner ring of the flame tube	Zu	left engine
3	combustion chamber outlet	-	depth along the blade height
4	outlet of the turbine		radial average
200	200 point temperature field *		viscosity coefficient

REFERENCES

- [1] Edited by Huang Zhao-xiang "Combustion Chamber of Turbojet Engine for Aeronautics", Defense Publication, July 1979.
- [2] Robert, R., Tacina and Jack Grobman: "Analysis of Total-Pressure Loss and Airflow Distribution for Annular Gas Turbine Combustors", NASA TND-5385.

DISTRIBUTION LIST

DISTRIBUTION DIRECT TO RECIPIENT

<u>ORGANIZATION</u>	<u>MICROFICHE</u>
A205 DMAHTC	1
A210 DMAAC	1
B344 DIA/RTS-2C	9
C043 USAMIIA	1
C500 TRADOC	1
C509 BALLISTIC RES LAB	1
C510 R&T LABS/AVRADCOM	1
C513 ARRADCOM	1
C535 AVRADCOM/TSARCOM	1
C539 TRASANA	4
C591 FSTC	1
C619 MIA REDSTONE	1
D008 NISC	1
E053 HQ USAF/INET	1
E403 AFSC/INA	1
E404 AEDC/DOF	1
E408 AFWL	1
E410 AD/IND	1
E429 SD/IND	1
P005 DOE/ISA/DDI	2
P050 CIA/OCR/ADD/SD	1
AFIT/LDE	
FTD	1
CCN	1
NIA/PHS	2
NIIS	1
LLNL/Code L-389	1
NASA/NST-44	2
NSA/1213/TDL	

ATE
LMED
8